Workshop of **Nuclear and Particle Physics** 2022

11.–18. 06. 2022, Bílý Potok

Faculty of Nuclear Sciences and Physical Engineering
Czech Technical University in Prague

Workshop of Nuclear and Particle Physics 2022

Editors:	L. Novotný
Issued by:	Czech Technical University in Prague
	Faculty of Nuclear Sciences and Physical Engineering
Address:	KF FJFI ČVUT, Břehová 7, 115 19 Praha 1
	novotl23@fjfi.cvut.cz, +420728222668

Available at `https://indico.fjfi.cvut.cz/event/200/attachments/1238/1876/book_of_proceedings.pdf`
First edition. 89 pages.

Contents

Jet energy loss in relativistic heavy-ion collisions with realistic medium modeling
Josef Bobek **iv**

A talk about jets which everyone will understand
Robert Líčeník **vii**

Predictions for future electron-ion colliders with the Balitsky–Kovchegov equation
Dagmar Bendová **ix**

Measurements of open-heavy flavor hadrons at RHIC and the LHC
Jan Vaněk **xii**

Moon shadow (not) seen by the experiment KASCADE & new energy calibration
Karolína Syrokvaš **xv**

ALICE update and latest data
Helena Hesounová **xviii**

Inclusive dijet studies at the ATLAS experiment
Ota Zaplatilek **xxiv**

Cluster sunrise
Zdenek Hubacek **xxix**

Incoherent photoproduction of J/ψ with ALICE
David Grund **xxxi**

Longitudinal profiles of the highest energy cosmic-ray air showers measured at the Pierre Auger Observatory
Nikolas Denner **xxxiv**

Development of barrel hadronic calorimeter for ATHENA
Leszek Kosarzewski **xxxvii**

Central inclusive production of K^0_S at the experiment STAR
Michaela Svěráková **xxxix**

Linearity of the upgraded electronics at the Pierre Auger Observatory
Marek Strnad **xlii**

Femtosecond electrostatic electron gun design and optimization
Zdeněk Vostřel **xlv**

Charm meson production in proton-nucleus collisions in the STAR experiment
Michal Svoboda **xlviii**

Study of non-linear evolution of the hadron structure within quantum chromodynamics
Matěj Vaculčiak **li**

Laser driven plasma waveguides for tabletop synchrotrons
Martin Guldan **liv**

Design patterns in data science
Henry Day-Hall **lvii**

Upsilon meson production in p+p collisions measured at STAR
Jakub Češka **lx**

Study of the mass composition and hadronic interactions of the ultra-high energy cosmic rays using data of the Pierre Auger Observatory
Tereza Potúčková **lxiii**

Electron production from the open-heavy flavor decay in relativistic heavy-ion collision at STAR
Ayanabha Da **lxxxviii**

Charm production
Kristýna Haismanová **lxxxviii**

Studies of strangeness production vs. charged particle multiplicity with PYTHIA8 and pion interferometry with CorAL
Subhadip Pal **lxxxviii**

Imaginary magnetic field in relativistic quantum mechanics
Alexandra Ridziková **lxxxviii**

Trenasverse expansion in nuclear collisions at RHIC BES
Jakub Štěrba **lxxxviii**

Evolution of galaxies in clusters
Anežka Kabátová **lxxxviii**

Foreword

This year, for the 14^{th} time, students, graduates, and teachers from the field of Nuclear and Particle Physics at FNSPE CTU met at the annual winter workshop held in June this year due to the pandemic of Covid-19 in winter. The meeting was held during the week of 11.–18. 06. 2022 at Penzion Krakonoš in the Jizera Mountains in the Czech Republic. The main goal of the workshop is to follow the progress of students, discuss problems and experiences and also to get to know each other better. Each participant gave a talk about their work or progress during the previous year. Extended abstracts of these talks are published in the proceedings you are holding now.

Editors

JET ENERGY LOSS IN RELATIVISTIC HEAVY-ION COLLISIONS WITH REALISTIC MEDIUM MODELING

Josef Bobek

1 Introduction

Two kind of processes happening during the heavy-ion collision at LHC experiments. The first is that when nuclei pass each other, there is a huge amount of energy deposited in the collision rgion. The temperature is so high that the particles and the corresponding antiparticles are created and a hot and dense medium is formed. This medium is called a quark-gluon plasma (QGP). The medium is indeed composed of quarks, antiquarks, and gluons that interact with a strong interaction described by quantum chromodynamics (QCD). Because this dense medium is surrounded by vacuum, it expands and cools, and when it reaches the critical temperature $T_c \approx 165$ MeV, it undergoes a crossover phase transition to hadronic degrees of freedom. This is called a soft QCD.

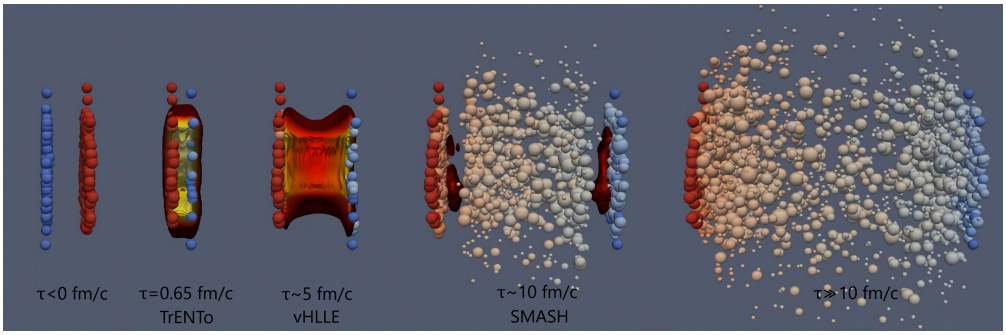

The second type of processed is called hard QCD. The hard QCD process means that a particle with a large amount of transverse momenta p_T was produced. Nuclei are composed of nucleons, and those are composed of quarks, antiquarks, and gluons. These are called partons, and when partons collide at the beginning of the collision, large p_T back-to-back partons are possibly created. Partons split and lose energy inside the medium. In the end they hadronize, and we can detect them as a collimated shower of hadrons. Then one has to use sophisticated algorithms to reconstruct a full jet with background subtraction.

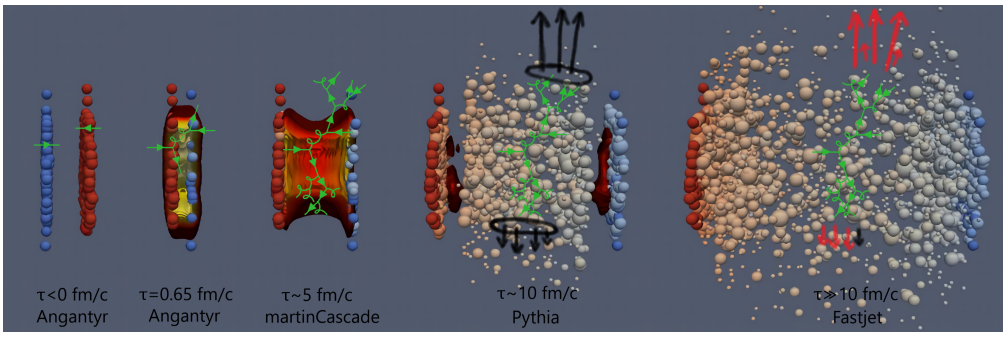

My master thesis reseach is focused on study of energy loss and overall evolution inside realistically simulated QGP.

2 Medium modeling

2.1 Initial state model

TRENTo (Reduced Thickness Event-by-event Nuclear Topology) model is a parametric initial condition model introduced in 2014 in [**?**]. This non-dynamical model is based on eikonal entropy density deposition directly proportional to reduced thickness function

$$T_R\left(p; T_A, T_B\right) \equiv \left(\frac{T_A^p + T_B^p}{2}\right)^{1/p}, \quad \text{where} \quad T_A(x,y) \equiv \int \rho_A^{\mathrm{part}}(x,y,z)\mathrm{d}z,$$

where $\rho_A^{\mathrm{part}}(x,y,z)$ is participating nucleon density function of nucleus A. T_A is called participant thickness function of nucleus A. Finally, p is a model parameter of TRENTo.

2.2 Hydrodynamic simulation

Initial state from TRENTo is passed to the relativistic hydrodynamic simulation code `vHLLE` [**?**]. This code employs second-order Israel-Stewart equations with Grad's 14-Momentum approximation

$$\begin{aligned} D\Pi &= \frac{-\zeta\theta - \Pi}{\tau_\Pi} - \frac{\delta_{\Pi\Pi}}{\tau_\Pi}\Pi\theta + \frac{\lambda_{\Pi\pi}}{\tau_\Pi}\pi^{\mu\nu}\sigma_{\mu\nu}, \\ D\pi^{\langle\mu\nu\rangle} &= \frac{2\eta\sigma^{\mu\nu} - \pi^{\mu\nu}}{\tau_\pi} - \frac{\delta_{\pi\pi}}{\tau_\pi}\pi^{\mu\nu}\theta + \frac{\phi_7}{\tau_\pi}\pi_\alpha^{\langle\mu}\pi^{\nu\rangle\alpha} - \frac{\tau_{\pi\pi}}{\tau_\pi}\pi_\alpha^{\langle\mu}\sigma^{\nu\rangle\alpha} + \frac{\lambda_{\pi\Pi}}{\tau_\pi}\Pi\sigma^{\mu\nu}, \end{aligned}$$

where there are several transport coefficients and among them shear viscosity η and bulk viscosity ζ.

2.3 Freeze-out of the QGP

A hadronic transport code `SMASH` [**?**] thakes information from `vHLLE` simulation at the freeze-out hypersurface Σ_μ (2+1 surface at critical temperature T_c) and samples it into Cooper-Frye formula

$$E\frac{\mathrm{d}N_i}{\mathrm{d}^3p} = \int_\Sigma \mathrm{d}\Sigma_\mu p^\mu f_i\left(T, p_\mu u^\mu, \pi^{\mu\nu}\right),$$

where $f_i\left(T, p_\mu u^\mu, \pi^{\mu\nu}\right)$ are particle distribution functions of particle species i. Then hadronic rescattering and resonance decays takes place.

3 Jet evolution modeling

3.1 Initial state of the partons

Initial positions and four-momenta of hard partons are obtain from `Pythia/Angantyr` [**?**]. Angantyr takes standard Woods-Saxon nucleon distribution and then use Glauber–Gribov model to collide nuclei. With parton distribution functions $f_{a/p}(x)$ and $2 \to 2$ cross-section one can just calculate initial parton production $\sum_{ab} f_{a/p} \star f_{b/p} \star \widehat{\sigma}_{ab}$.

3.2 Parton cascade evolution

In vacuum, patrons split ($q \to q + g$, $g \to g + g$, $g \to q + \overline{q}$) according to QCD. With leading-order parton splitting functions ($\widehat{P}_{qq}$, $\widehat{P}_{gg}$, $\widehat{P}_{qg}$) one can obtain Sudakov form factor

$$S_a\left(Q_{\mathrm{i}}^2, Q_{\mathrm{f}}^2\right) = \exp\left[-\int_{Q_{\mathrm{f}}^2}^{Q_{\mathrm{i}}^2} \frac{\mathrm{d}Q^2}{Q^2}\int_{z_-}^{z_+} \mathrm{d}z \frac{\alpha_{\mathrm{s}}}{2\pi}\sum_b \widehat{P}_{ba}(z)\right]$$

and build Monte Carlo simulation around it. [**?**]

Energy loss inside the medium is due to $2 \rightarrow 2$ elastic processes with the medium partons and $2 \rightarrow 3$ medium-induced gluon radiation. Cross-section for the first part can be calculated from QCD and then regularised. Second part can be approached by enhancment of parton splitting ($1 \rightarrow 2$ processes). [**?**] Results of this model are introduced in [**?**].

Information about the medium temperature is taken from hydrodynamic simulation `vHLLE`.

3.3 Hadronization

Final state partons are then hadronized via the Lund string phenomenological model [**?**]. This model is implemeted in `Pythia` and is based on QCD potential

$$V_{\mathrm{QCD}} = -\frac{4}{3}\frac{\alpha_s}{r} + \kappa r + ...,$$

where κ is the string tension, which is around 1 GeV/fm. String in the name stands for the potential linearly rising with the distance between the two quarks.

3.4 Reconstruction

When one obtains hadrons from `SMASH` and Lund string model it is necessary to reconstruct jets without the medium background. The reconstruction by the k_T algorithm takes place as a first step and ghost particle algorithm is used to determine the area A_{jet} of the jet. Then transverse momentum density of background ρ in the event is calculated as

$$\rho = \mathrm{median}\left\{\frac{p_{T,\,\mathrm{jet}}^{\mathrm{raw},j}}{A_{\mathrm{jet}}^{j}}\right\},$$

where one or two hardest jets (depends on centrality) are excluded from median calculation. Finally, anti-k_T algorithm is used to reconstruct raw jet spectra. Then background is subtracted as

$$p_{T,jet} = p_{T,jet}^{\mathrm{raw}} - \rho A.$$

A TALK ABOUT JETS WHICH EVERYONE WILL UNDERSTAND

Robert Líčeník

1 Introduction

Talks about jet physics and jet analyses are far too often too technical for younger students or non-experts to understand. This makes it harder to fully appreciate the power and beauty of jet measurements and the physics which motivate them. This document aims to give the easiest possible explanation of jet physics related to the physics of heavy-ion collisions.

2 Why jets?

Jets serve as an excellent probe of quark-gluon plasma (QGP), an exotic state of matter created during heavy-ion collisions, where quarks and gluons exist briefly in a deconfined state. First proposed by Bjorken [1], the now firmly established [2, 5] phenomenon of jet quenching (i.e. suppression of observed number of jets with high transverse momentum p_{T}) is considered a smoking-gun evidence for QGP existence. Since jets are created during hard (high-p_{T}) processes, it is possible to calculate the cross section using perturbative quantum chromodynammics, which makes theory predictions viable.

3 What jets?

Jets are often presented as "collimated sprays of hadrons". Althought it is not entirely incorrect, this expression does not contain all the important considerations that need to go into the interpretation of the results to the physics underneath. Jets serve as an approximation for individual partons as they are formed during parton fragmentation. After fragmentation (sort of understood process) and hadronization (not well understood process), jet particles can be detected in a detector as a collection of particles or calorimeter energy. Jets are defined by the reconstruction algorithms, the most widely used being the anti-k_T algorithm. The anti-k_T algorithm clusters particles sequentially by minimizing the distance between jet constituents, starting with the hardest particles. Making the connection between the jets reconstructed by the algorithm and jets as the products of individual parton fragmentations is not a trivial task, especially

4 How jets?

Reconstructing jets in heavy-ion collisions is an extremelly challenging task due to the large soft background (underlying event) of soft uncorrelated particles. Therefore corrections are needed before one can interpret the results. Common technique is the median background subtraction where the median background density multiplied by jet area is subtracted from reconstructed jet p_{T}. During the next step, the p_{T} of the hardest particle in the jet is required to be higher than a chosen threshold. This step biases the fragmentation of the initial parton and therefore needs to be carefully considered when interpreting the results. Then, the results need to be corrected for background fluctuations and also for instrumental effects. The simulated response matrix gives the probability of measuring a jet with p_{T}^{meas}, given a true jet with p_{T}^{true}. The correction then consists of inverting the matrix and multiplying the measured jet spectrum with this inverse response matrix. However, the response matrix is often singular and therefore no inverse

matrix exists. A technique called unfolding is often used to approximate the inverse matrix. There are many methods of unfolding, but the often-used ones are the iterative Bayesian and SVD methods. After the unfolding and obtaining the true jet spectrum, the systematic errors need to be estimated. Discussion of systematic errors is beyond the scope of this document.

References

[1] James D. Bjorken Energy Loss of Energetic Partons in Quark-Gluon Plasma: Possible Extinction of High $p_\perp$ Jets in Hadron-Hadron Collisions. Unpublished, Fermilab-Pub-82/59-THY, Batavia (1982).

[2] Jaroslav Adam et al. (ALICE). Measurement of jet suppression in central Pb-Pb collisions at $\sqrt{s_{NN}}$ = 2.76 TeV. In Physics Letters B 746, 1 (2015), arXiv:1502.01689 [nucl-ex].

[3] Jaroslav Adam et al. (STAR). Measurement of inclusive charged-particle jet production in Au+Au collisions at $\sqrt{s_{NN}}$ = 200 GeV. In Physical Review C 102 (2020) 5, 054913.

PREDICTIONS FOR FUTURE ELECTRON-ION COLLIDERS WITH THE BALITSKY–KOVCHEGOV EQUATION

Dagmar Bendová

1 Introduction

It is known for several decades now that hadron are particles with inner structure. They are composed of (anti)quarks and gluons, which intermediate the interaction among quarks. However, there are still many unanswered questions about the nature of the hadron structure, e.g. its evolution with changing energy, its modification when the individual nucleons are bound inside a nucleus, the contribution from individual quarks and gluons to the overall mass, spin, and other quantities, etc. Currently proposed electron-ion colliders in the US (EIC) and in Europe (LHeC) aim to shed a light into these problems of the quantum chromodynamics (QCD) at high energies (for an extensive review, see e.g. [1] and [2]). It is therefore necessary to complement these experimental plans with corresponding phenomenological predictions of physical observables which provide both a connection to previous measurements and a guidance to the next development in both experimental and theoretical area.

2 QCD phenomenology at high energies

In the past, the deep inelastic scattering (DIS) has proven to be a very successful experimental tool to study the inner structure of hadrons in ep collisions at HERA. The process goes as follows: the incoming electron emits a virtual photon with virtuality Q^2, defined as $Q^2 = -(k - k')^2$, where k, and k' are four-momenta of the incoming and the rescattered electron. The photon then interacts with the target hadron. In the Feynman's parton model picture, the photon can be seen as interacting with one of the constituent partons (now associated with quarks and gluons) which carry a momentum fraction x of the hadron. Measurement of the final state system and the rescattered electron allows for the precise measurement of the change of the proton structure in the means x and Q^2, given as an evolution of distribution functions of the constituent quarks and gluons.

At low energies, proton is dominated by the valence quarks uud which determine its quantum numbers. However with increasing energy, this picture starts to change as more and more sea quarks and antiquarks emerge from the available energy of the vacuum and also gluons branch and start to dominate the hadron structure. This evolution of hadron structure is described by evolution equations. So called DGLAP equation describes the change of the proton structure with increasing Q^2. Simply said, it tells us how the structure changes when we use a probe with better resolution in our experiment. By fixing the scale of the process, one can study another evolution direction – decreasing Bjorken-x, where the overall hadron's momentum is distributed among higher and higher number of partons. This directions of the evolution is dominated by gluons which increase their numbers via gluon branching process. However, the untamed growth of gluon densities would cause a divergence of the corresponding distribution functions and, subsequently, unphysically large values of cross section and unitarity violation. It is therefore expected that the number of gluons should saturate after reaching a certain domain of densities – denoted as a *saturation scale*. Below this scale, the branching process dominated and the rise of gluon densities is linear, described by the BFKL equation. However, after reaching the saturation region, gluon recombination starts to play a role and the subsequent evolution of hadron structure becomes non-linear and can be described by JIMWLK equations or the Balitsky–Kovchegov (BK) equation, which is a special case of the full JIMWLK hierarchy of evolution equations.

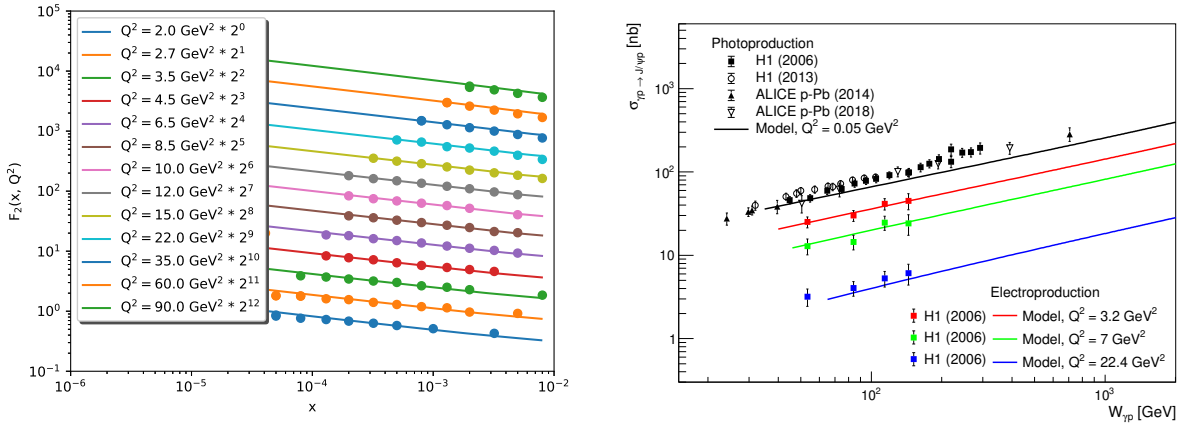

Figure 1: Results using the b-dependent BK equation. (Left:) x-dependence of the proton structure function F_2 for several values of Q^2 compared to data from HERA. (Right:) Energy $W_{\gamma p}$ dependence of the $\gamma p \to J/\psi p$ cross section for several values of Q^2 compared to data from ep collisions at HERA and from pPb ultraperipheral collisions at the LHC. Figures from [4].

In order to describe the DIS and other QCD processes at high energies it is necessary to view the photon-hadron interaction in the way it allows for strong interaction to govern the process. The color dipole model has successfully proven to be such phenomenological model of DIS. In this model, the virtual photon can be seen as fluctuating into one of its Fock states, where the simplest one is $q\bar{q}$ pair – a color dipole, which then interacts with the hadron via gluon exchange. One can then use the BK evolution equation to calculate the dipole-hadron scattering amplitude at given x and use it for phenomenological calculations of the γ-hadron interaction in DIS and other processes like production of vector mesons in ep, eA, and pA and AA ultraperipheral collisions, or the deeply virtual Compton scattering (DVCS). Since the dipole and the target hadron are interconnected by the interaction, evolution of the dipole structure via BK equation provides us information about the target hadron structure.

3 Selected results

Using the above mentioned approach, we use the BK equation to calculate several QCD observables. First we numerically solve the BK equation. In general, it depends on three variables – x, which represents the energy of the process, and vectors $\vec{r}$ and $\vec{b}$, which represent size of the dipole and its distance from the target (so called *impact parameter*) in plane transverse to the direction of movement of the interacting particles. Since the solution to the full BK equation depending on the mentioned vectors is technically and computationally very demanding, several simplifications has been used for phenomenological applications – the mostly used approach has been to factorise the b-dependence out into a function which is then modelled separately. In the previous works [3, 4] a new approach to solutions of the BK equation was introduced which allows for the calculation to explicitly depend on both r and b. This approach proved to be successful in description of both inclusive (DIS) and exclusive processes (VM production, DVCS) – see Fig. 1. It has subsequently been extended to the case of nuclear targets [5] which allows us to make predictions for future facilities where such experimental measurements will be performed. It also allows us to compare our result with current measurements in ultraperipheral collisions (UPC) at the LHC – see Fig. 2.

4 Conclusions

Solution to the BK equation with as much complexity as possible presents one of the current open problems in high energy QCD phenomenology. There has been several successful calculations using simplified versions of the equation and currently, there are attempts to extend the calculation towards more complex picture. In our work, we obtained

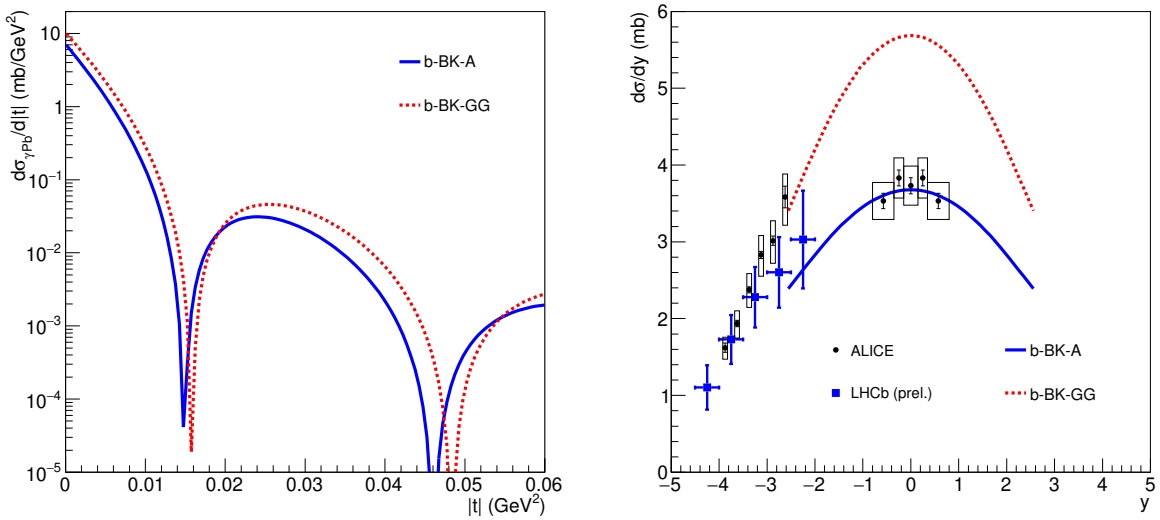

Figure 2: Results for the coherent $J\psi$ photoproduction in γPb collisions using two approaches to the nuclear b-dependent BK evolution. (Left:) $|t|$-dependence of the J/ψ cross section. (Right:) Rapidity y dependence of the J/ψ photoproduction cross section compared to data from UPCs at the LHC. Figures from [6].

solution of the dipole-hadron scattering amplitude with an explicit dependence on the impact-parameter b and we have successfully applied it into several QCD processes – namely to inclusive and diffractive DIS, production of vector mesons, and DVCS. These predictions are of interest for measurements at current and future facilities such as LHC, EIC or LHeC. It is expected that at the planned electron-ion colliders, structure functions of nuclei will be measured with great precisions. And since the saturation is expected to onset sooner in nuclei than in protons, it is therefore expected that we will obtain first experimental evidence of parton saturation. These new measurements can therefore enable us to better understand the QCD dynamics at high energies and help us to improve our models and their input for the relevant processes.

References

[1] R. Abdul Khalek *et al.* Science Requirements and Detector Concepts for the Electron-Ion Collider: EIC Yellow Report. arXiv:2103.05419.

[2] P. Agostini *et al.* The Large Hadron-Electron Collider at the HL-LHC. In *Journal of Physics G: Nuclear and Particle Physics 48*, 110501, 2021.

[3] J. Cepila, J. G. Contreras, and M. Matas. Collinearly improved kernel suppresses Coulomb tails in the impact-parameter dependent Balitsky-Kovchegov evolution. In *Physical Review D 99*, 051502, 2019.

[4] D. Bendova, J. Cepila, J. G. Contreras, and M. Matas. Solution to the Balitsky-Kovchegov equation with the collinearly improved kernel including impact-parameter dependence. In *Physical Review D 100*, 054015, 2019.

[5] J. Cepila, J. G. Contreras, and M. Matas. Predictions for nuclear structure functions from the impact-parameter dependent Balitsky-Kovchegov equation. In *Physical Review C 102*, 044318, 2020.

[6] D. Bendova, J. Cepila, J. G. Contreras, and M. Matas. Photonuclear J/ψ production at the LHC: proton-based versus nuclear dipole scattering amplitudes. In *Physics Letters B 817*, 136306, 2021.

MEASUREMENTS OF OPEN-HEAVY FLAVOR HADRONS AT RHIC AND THE LHC

Jan Vaněk

1 Physics motivation

One of the main goals of physics program at the Relativistic Heavy-Ion Collider (RHIC) and the Large Hadron Collider (LHC) is to study properties of the hot and dense state of matter known as the Quark-Gluon Plasma (QGP), which can be created in ultra-relativistic collisions of heavy ions. One of the main challenges in studying properties of the QGP is that it has very short lifetime and it is therefore impossible to use any external probes to determine its properties. Fortunately, the collisions themselves are a source of suitable probes - the charm and bottom quarks.

Due to their large masses, both charm and bottom quarks are created predominantly in the hard partonic scatterings, at very early stages of the heavy-ion collisions, before the QGP is ignited. As a result, they pass through the medium, where they loose energy and momentum. The energy loss can be then quantified, for example, by comparing measurement in heavy-ion collisions to that in p+p collisions where no medium is present.

Table 1: Summary of open heavy-flavor hadrons measured at RHIC and the LHC. The left part of the table contains open-charm hadrons the right part open-bottom hadrons. Quark contents of the the hadrons are provided in brackets. Also shown are the rest masses ($M_{\rm inv}$) and lifetimes, as path-length ($c\tau$). Values taken from Ref. [1].

Hadron	$M_{\rm inv}$ [MeV]$/c^2$	$c\tau$ [μm]	Hadron	$M_{\rm inv}$ [MeV]$/c^2$	$c\tau$ [μm]
D^+ $(c\bar{u})$	1869.66 ± 0.05	311.8 ± 2.1	B^+ $(u\bar{b})$	5279.34 ± 0.12	491.1 ± 1.2
D^0 $(c\bar{d})$	1864.84 ± 0.05	122.9 ± 0.4	B^0 $(d\bar{b})$	5279.66 ± 0.12	455.4 ± 1.2
D_s^+ $(c\bar{s})$	1968.35 ± 0.07	149.9 ± 2.1	B_s^0 $(s\bar{b})$	5366.92 ± 0.10	455.7 ± 1.5
Λ_c^+ (udc)	2286.46 ± 0.14	59.9 ± 1.8	Λ_b^0 (udb)	5619.60 ± 0.17	441.0 ± 2.7
Ξ_c^+ (dsc)	2470.44 ± 0.28	45.5 ± 0.7			

One possible way to access information about heavy quark production in any type of collision system is by measurement of open heavy-flavor hadron production. A list of open heavy-flavor hadrons measured at RHIC and the LHC and their basic properties are summarized in Tab. 1. One of the main challenges in reconstruction of the open heavy-flavor hadrons is their short lifetime which means that they cannot be observed directly, but only through their decays.

Generally, there are two main experimental methods used for reconstruction of the open heavy-flavor hadrons. The first one is reconstruction of semi-leptonic decays, such as $\mathrm{D}^+ \rightarrow \mathrm{K}^- e^+ \nu_e$, i.e. decays containing positron (electron), (anti-)neutrino, and any hadronic state. In this case, only the lepton is detected which means that the kinematics of the mother particle is not accessible. On the other hand, this method can provide insight into ratio of open-charm and open-bottom production. In order to have direct access to the mother particle kinematics, it is necessary to topologically reconstruct hadronic decays of the open heavy-flavor hadrons. The main challenges with this method are that it requires very precise resolution of primary and secondary (decay) vertices and that it needs large data samples due, as the reconstruction efficiency of open heavy-flavor hadrons is often low.

The following section provides a selection of recent results from measurement of the open heavy-flavor hadrons by the STAR experiment at RHIC and the ALICE experiment at the LHC, utilizing both of the aforementioned methods.

2 Experimental results from RHIC and the LHC

One of the most straightforward methods to evaluate particle production modification in heavy-ion collisions with respect to p+p collisions is using the nuclear modification factor which can be defined as:

$$R_{\mathrm{AA}} = \frac{(\mathrm{d}N/\mathrm{d}p_{\mathrm{T}})_{\mathrm{AA}}}{\langle N_{\mathrm{coll}}\rangle (\mathrm{d}N/\mathrm{d}p_{\mathrm{T}})_{\mathrm{pp}}}, \tag{1}$$

where $(\mathrm{d}N/\mathrm{d}p_{\mathrm{T}})_{\mathrm{AA}}$ is an invariant yield p_{T} spectrum of particles of interest, e.g. open-charm mesons, measured in heavy-ion collisions, $(\mathrm{d}N/\mathrm{d}p_{\mathrm{T}})_{\mathrm{pp}}$ is the same spectrum measured in p+p collisions and $\langle N_{\mathrm{coll}}\rangle$ is the mean number of binary collision.

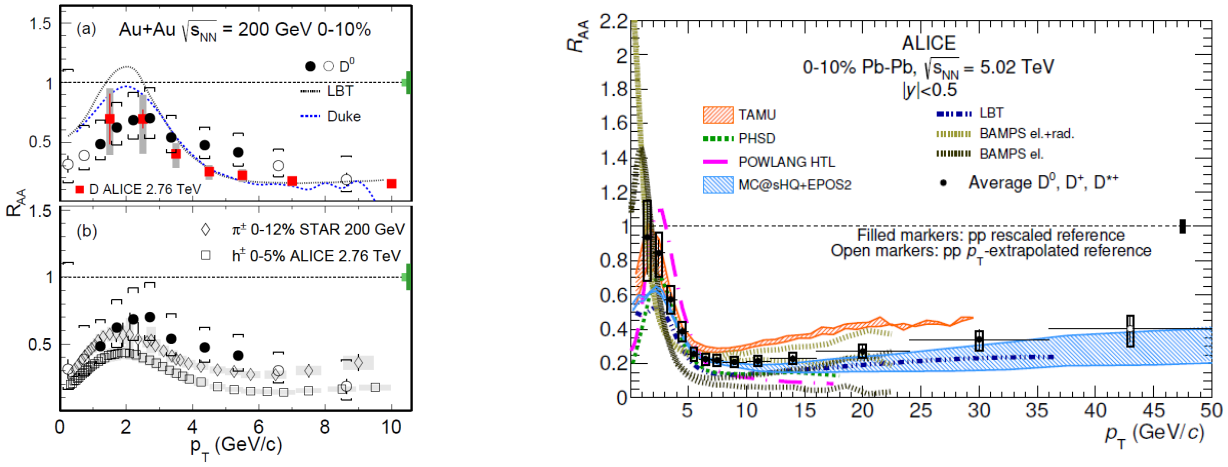

Figure 3: **(left)** Nuclear modification factor of D^0 mesons as a function of p_{T} measured by STAR in 0-10% central Au+Au collisions at $\sqrt{s_{\mathrm{NN}}} = 200\,\mathrm{GeV}$. Taken from Ref. [2]. **(right)** Nuclear modification factor of D mesons as a function of p_{T} measured by ALICE in 0-10% central Pb+Pb collisions at $\sqrt{s_{\mathrm{NN}}} = 5.02\,\mathrm{TeV}$. Taken from Ref. [3].

The R_{AA} of D mesons as a function of p_{T} measured by STAR in 0-10% central Au+Au collisions at $\sqrt{s_{\mathrm{NN}}} = 200\,\mathrm{GeV}$ and by ALICE in 0-10% central Pb+Pb collisions at $\sqrt{s_{\mathrm{NN}}} = 5.02\,\mathrm{TeV}$ is shown in Fig. 3. At both RHIC and the LHC, the high-p_{T} D mesons are significantly suppressed in central heavy-ion collisions which suggests substantial energy loss the charm quarks inside the QGP. This observation is supported by various models, which are also shown in Fig. 3. For more details, see Ref. [2, 3]. The results in Fig. 3 are obtained using the topological reconstruction method described in the previous section. Both STAR and ALICE have also performed similar measurements using the semi-leptonic decays of open-charm hadrons, which provide consistent results and are compatible with the charm quark energy loss scenario [4, 5].

The QGP also has significant influence on the hadronization mechanism of heavy quarks in heavy ion collisions. This can be seen, for example, in measurement of $\Lambda_{\mathrm{c}}/\mathrm{D}^0$ yield ratio, which is shown in Fig. 4. Both at RHIC (left panel) and the LHC (right panel), the Λ_{c} baryons are enhanced in heavy-ion collisions with respect to p+p collisions. The enhancement can be well described by models which incorporate both fragmentation hadronization and coalescence hadronization of charm quarks [6]. It is important to note here, that ALICE also observes an enhancement of open-charm baryons in p+p collisions compared to various model predictions [8, 9]. Production of open-charm baryons is therefore very important in understanding the charm quark hadronization in both p+p and heavy-ion collisions.

Both STAR and ALICE have also performed measurements of open-bottom hadron production in heavy-ion collisions. STAR accessed the open-bottom production via measurement of semi-leptonic decays [4], ALICE has used direct topological reconstruction of D mesons which decayed far from the primary vertex, which likely originate from

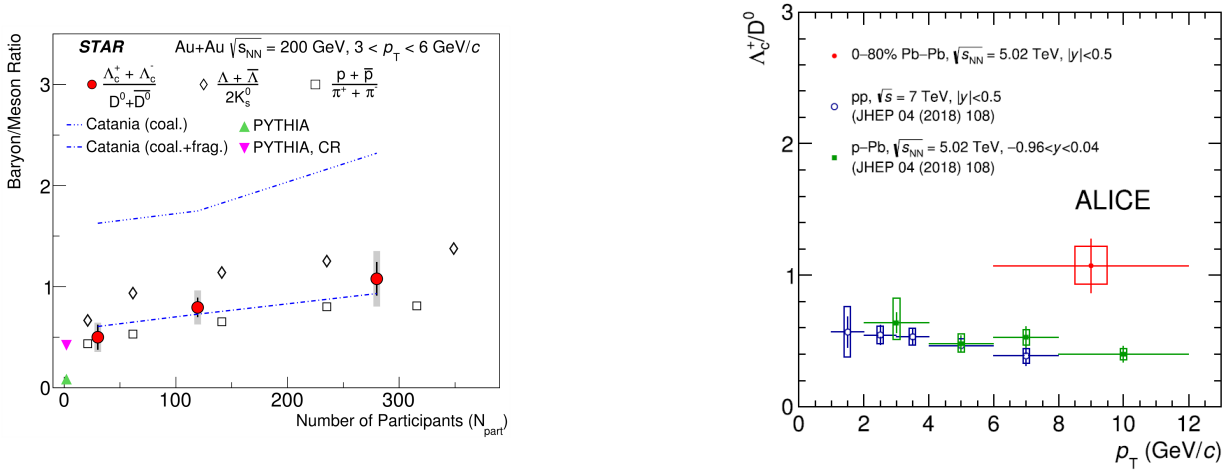

Figure 4: **(left)** Λ_c/D^0 yield ratio as a function of number of participants ($N_{\rm part}$) measured by STAR in Au+Au collisions at $\sqrt{s_{\rm NN}} = 200\,\text{GeV}$. Taken from Ref. [6]. **(right)** Λ_c/D^0 yield ratio as a function of $p_{\rm T}$ measured by ALICE in 0-80%)central Pb+Pb collisions at $\sqrt{s_{\rm NN}} = 5.02\,\text{TeV}$ and in p+p collisions at $\sqrt{s_{\rm NN}} = 5.02\,\text{TeV}$ and $\sqrt{s_{\rm NN}} = 7\,\text{TeV}$. Taken from Ref. [7].

decays of open-bottom hadrons [10, 11]. All measurements suggest that bottom quarks also experience energy loss inside QGP, which is smaller that that of charm quarks, due to lager mass of bottom quarks.

3 Summary

STAR and ALICE experiments have very rich open heavy-flavor program in both heavy-ion and p+p collisions. The measured data suggest that both charm and bottom quarks loose energy inside the QGP. Charm quarks loose significant part of their energy which is suggested by significant suppression of D meson production in central heavy-ion collisions with respect to the p+p collisions. Bottom quarks seem to loose energy in QGP as well, but much less than charm quarks due to larger mass of the bottom quarks. The enhancement of the Λ_c/D^0 yield ratio measured by STAR also suggests that charm quarks experience combination of fragmentation and coalescence hadronization in heavy-ion collisions. Similar enhancement of open-charm baryons is observed by ALICE in both Pb+Pb and p+p collisions. Measurements of open-charm baryons are therefore vital for understanding of charm quark hadronization.

References

[1] R.L. Workman, *et al.* [Particle Data Group], to be published in Prog. Theor. Exp. Phys. 2022, 083C01 (2022).

[2] J. Adam, *et al.* [STAR Collaboration], Phys. Rev. C **99**, 034908, (2019).

[3] S. Acharya, *et al.* [ALICE Collaboration], J. High Energ. Phys. **2018**, 174 (2018).

[4] J. Adam, *et al.* [STAR Collaboration], arXiv:2111.14615 [nucl-ex].

[5] S. Acharya, *et al.* [ALICE Collaboration], Phys. Lett. B **804** , 135377, (2020).

[6] J. Adam, *et al.* [STAR Collaboration], Phys. Rev. Lett. **124**, 172301, (2020).

[7] S. Acharya, *et al.* [ALICE Collaboration], Phys. Lett. B **793**, 212-223, (2019).

[8] S. Acharya, *et al.* [ALICE Collaboration], Phys. Lett. B **829**, 137065, (2019).

[9] S. Acharya, *et al.* [ALICE Collaboration],J. High Energ. Phys. **2021**, 159 (2021).

[10] S. Acharya, *et al.* [ALICE Collaboration], arXiv:2202.00815 [nucl-ex].

[11] S. Acharya, *et al.* [ALICE Collaboration], arXiv:2204.10386 [nucl ex].

MOON SHADOW (NOT) SEEN BY THE EXPERIMENT KASCADE & NEW ENERGY CALIBRATION

Karolína Syrokvaš

1 Introduction

The Moon blocks trajectories of cosmic rays, while the geomagnetic field of Earth deflects it, shifting it with the respect to the true Moon position. This offset can be wrongly interpreted as a systematic offset of event reconstruction, making the study of the Moon shadow crucial for correct event reconstruction. We investigate whether the Moon shadow is visible on the data recorded by the experiment KASCADE between the dates 8.5.1998 - 20.12.2003.

2 The cosmic-ray experiment KASCADE

The KASCADE (KArlsruhe Shower Core and Array Detector) experiment was a large-area detector for the measurement of high-energy cosmic rays situated in the Karlsruhe Institute of Technology, Campus North, Germany. After starting data acquisition in 1996, the experiment was extended to KASCADE-Grande in 2003 to reach higher energies of primary cosmic rays, since the flux decreases to less than one per day and square metre. While the experiment stopped data acquisition in 2012, the international collaboration of the experiment continues the detailed analysis of nearly 20 years of data.

2.1 The Moon and Sun shadow

large celestial bodies such as the Sun and the Moon block the trajectories of incoming cosmic rays, creating a shadow. While the Sun is also a source of primary cosmic rays, solar cosmic rays typically reach energies of 10^7 to 10^{10} eV, which is three orders below the sensitivity threshold of the KASCADE experiment. The geomagnetic field - Earth's own magnetic field generated by its core - causes a shift in the shadow position with respect to the true position of the celestial body. This can be wrongly interpreted as a systematic offset of event reconstruction, leading to a decrease in data quality. The observed Moon or Sun shadow also helps show the angular resolution of the experiment, which, in the case of the KASCADE experiment, should be 0.1 degrees.

The data used are publicly available from `https://kcdc.iap.kit.edu/`, where data for the interested public, preselected datasets and simulations with pre- and post-LHC hadronic interaction models can be found. In our current dataset, KASCADE did not have its extension KASCADE-Grande yet. Used were run 877 – 4683 taken from 8^{th} May 1998 to 20^{th} December 2003. The energy range $10^{13} - 10^{19}$ eV was used. The incoming events were transformed into equatorial coordinates with the implementation of libnova library. The only cut for the data was a cut for declination, which was required to be less than 30°, only close to the Moon trajectory.

As seen on Figure 5, the experiment KASCADE does not seem to be sensitive towards the Moon or the Sun shadow. This is most likely caused by the sensitivity of the experiment, where quality cuts for the data taken suggest the incoming events have zenith angle less than 60°, while the maximum Moon zenith angle in Germany is 70° and the maximum Sun zenith angle is 65°, which is below this quality cut. This suggests a less intuitive approach is needed to analyse the Moon and the Sun shadow the KASCADE data.

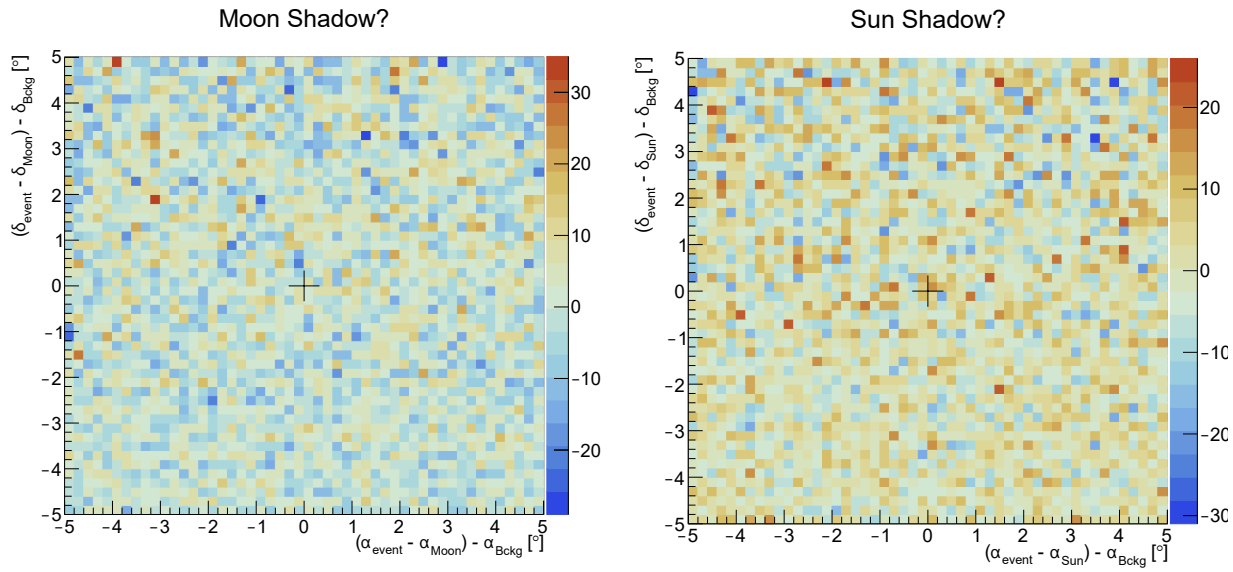

Figure 5: The flux of incoming events transformed into shifted equatorial coordinates with the Moon (left) and the Sun (right) in its centre, marked by the cross.

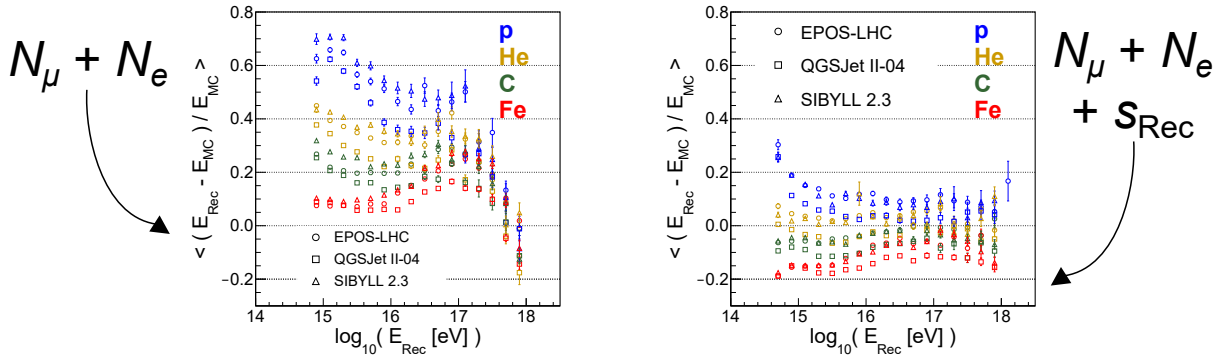

Figure 6: Biases of the shower energy estimated using KASCADE formula (left) and using new energy calibration (right). From `https://pos.sissa.it/358/453/pdf`.

2.2 New energy reconstruction of the experiment KASCADE

The experiment KASCADE computes the muonic and electromagnetic components simultaneously and independently, which makes the estimation of the primary energy using these two parameters - the number of muons and the number of electrons on ground - very useful. However, using only two parameters can lead to uncertainties in the estimation. We propose using additional parameters, the zenith angle of the incoming particle and the lateral shape parameter s to improve the old energy reconstruction formula. This can lead to a reduction of biases of the reconstructed shower energy, as seen on Figure 6.

The old energy reconstruction formula is as follows:

$$\begin{aligned}\log_{10} E = {} & 1.93499 + 0.66704 \cdot \log_{10} N_\mu + 0.07507 \cdot \log_{10} N_\mathrm{e}^2 \\ & + 0.25788 \cdot \log_{10} N_\mathrm{e} + 0.09277 \cdot \log_{10} N_\mu^2 \\ & - 0.16131 \cdot \log_{10} N_\mathrm{e} \cdot \log_{10} N_\mu,\end{aligned} \tag{2}$$

and with the new energy reconstruction, we propose the true (Monte Carlo simulated) energy is composed of the calorimetric energy, dependant on the lateral shape parameter and number of charged particles at ground for zero zenith angle, and the invisible energy, dependant on the zenith angle and the number of muons on ground:

$$\begin{aligned}
\log_{10} E_{\text{inv}} &= E_{\text{MC}} - E_{\text{Cal}} = C(\cos^2\theta) + \delta(\cos^2\theta) \cdot \log_{10} N_\mu \\
\log_{10} E_{\text{Cal}} &= E_{\text{MC}} - C(\cos^2\theta) + \delta(\cos^2\theta) \cdot \log_{10} N_\mu \\
&= D(s) + \omega(s) \cdot \log_{10} N_{\text{ch}}(0^\circ), \\
N_{\text{ch}}(0^\circ) &= N_{\text{e}}(0^\circ) + N_\mu(0^\circ), \\
\Rightarrow E_{\text{MC}} &= E_{\text{MC}}(N_\mu, N_{\text{e}}, \theta, s)
\end{aligned} \tag{3}$$

For this analysis, additional showers using CORSIKA 7.64 must be simulated, as the KASCADE data centre does not have longitudinal profiles of the produced showers necessary for the calibration of the calorimetric energy. 60000 showers were produced, with three hadronic interaction models EPOS LHC, QGSJet-II 07 and Sibyll 2.3c, four primary particles protons and the nuclei of helium, nitrogen and iron, ten fixed values of zenith angle with even distribution for squares cosine of the angles on the range $0^\circ - 40^\circ$ and five fixed primary energies ranging from 10^{15} eV to 10^{17} eV.

The new energy calibration will then be applied on simulations from `https://kcdc.iap.kit.edu/simul/simkas/` for three hadronic interaction models EPOS LHC, QGSJet-II 07 and Sibyll 2.3d, four primary particles protons and the nuclei of helium, carbon and iron and the energy range 10^{15} eV to 10^{18} eV.

ALICE UPDATE AND LATEST DATA

Helena Hesounová

1 Introduction

The Large Hadron Collider has finished the Long Shutdown 2 period, which lasted more than three years. The experiments at CERN have upgraded its detectors and analysis software during this time. Experiment ALICE has upgraded most of its detectors and the collaboration of ALICE created a new analysis software. First test runs performed in September 2021 provided us with data for calibration of all the new features.

2 ALICE upgrade

The LHC should be working with a higher interaction rate in Run 3. The increase is from 8 to 50 kHz for lead-lead collisions. Moreover, the new ALICE detectors have a continuous readout. These changes made a creation of a new analysis software inevitable. Besides the new software and the continuous readout, many other parts of the experiment were improved.

The Inner Tracking System detector has a completely new structure. Instead of three silicon pixel detectors, two layers each, a new seven-layered structure has been developed. The new ITS has an improved vertex reconstruction and determination of the DOCA. Because of the new structure, the whole tracks can be reconstructed using only ITS data. The Time Projection Chamber replaced its MultiWire Proportional Chambers with Gas Electron Multipliers, and the Fast Interaction Trigger complex of detectors replaced the old triggers. In addition, a new detector was developed: the Muon Forward Tracker.

The new software for analysis, called the Online-Offline or O^2 software, was developed in collaboration with the GSI. It has three main parts. The Transport Layer FairMQ, created in GSI, covers the communication between devices. The O^2 Data Model and the Data Processing Layer, developed by the ALICE Collaboration, are used for message description and process topology creation, respectively.

3 Pilot beam data

In September 2021, the ALICE collaboration acquired the first real data of the LHC Run 3. These data serve for calibration of the upgraded detectors and the new O^2 software. The analysis is a work in progress and does not provide definite answers. My contribution to the process was to compare two runs with the different polarities of the L3 magnet to check the symmetry between positively and negatively charged particles. The comparison of the vertex reconstruction and the multiplicity is in Fig. 7 and Fig. 8, respectively. In Fig. 9 is visible an ITS deficiency, that has already been dealt with.

To conclude, I proved the symmetry between the two studied runs. A deficiency of the ITS detector has been found and dealt with. The newly acquired data were used for the calibration of the detectors and the software and are in good agreement with our expectations and Monte Carlo simulations.

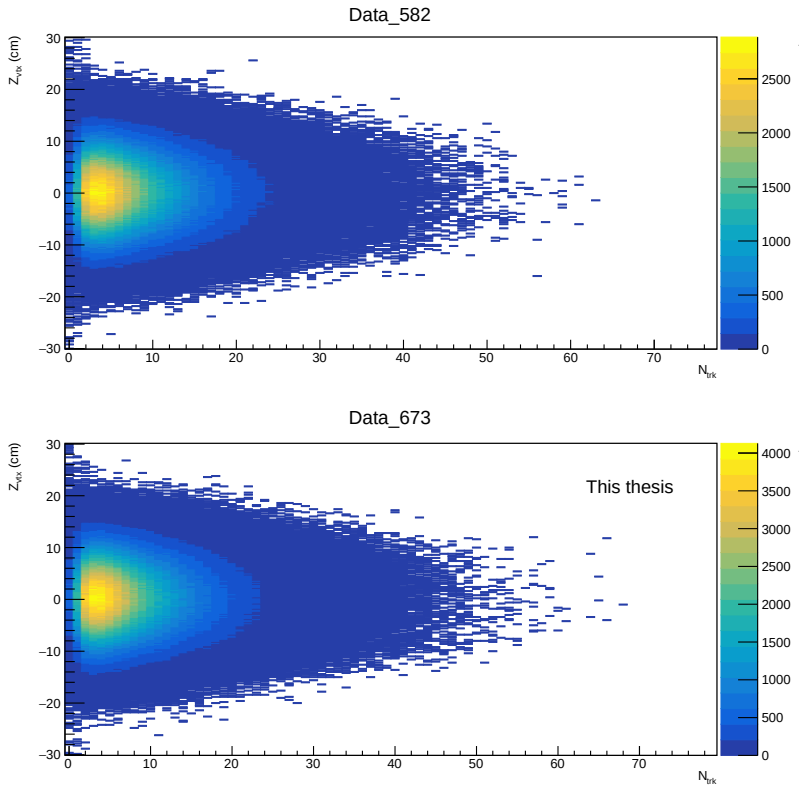

Figure 7: The vertex position distribution along the z axis in the run 582 with the negative polarity of the L3 magnet (upper panel) and the run 673 with the positive polarity of the L3 magnet (lower panel). Taken from [1].

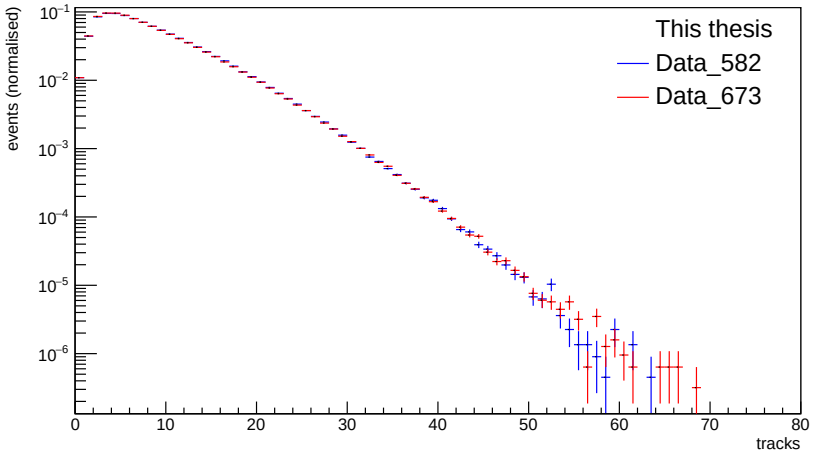

Figure 8: Normalised multiplicity distributions for run 582 with negative polarity of the L3 magnet and run 673 with positive polarity of the L3 magnet. Taken from [1].

References

[1] Hesounová H. 2022, 'Multiplicity measurements in pp collisions with ALICE during the LHC Run 3', Bachelor thesis, Czech Technical University in Prague

[2] George Kour and Raid Saabne. Real-time segmentation of on-line handwritten arabic script. In *Frontiers in*

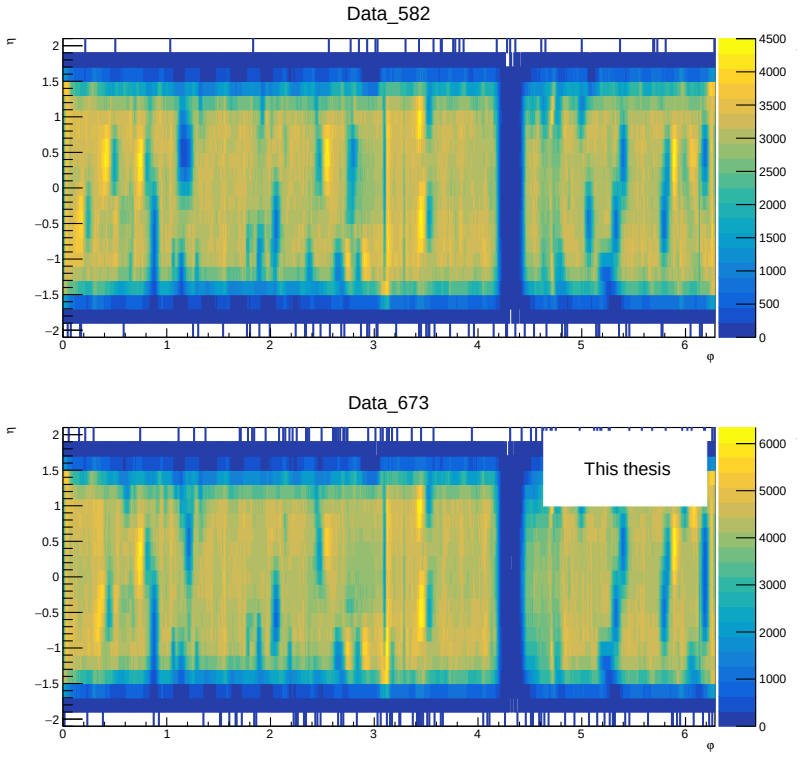

Figure 9: The φ, η distribution of detected particles in the run 582 with the negative polarity of the L3 magnet (upper panel) and the run 673 with the positive polarity of the L3 magnet (lower panel). Taken from [1].

Handwriting Recognition (ICFHR), 2014 14th International Conference on, pages 417–422. IEEE, 2014.

[3] George Kour and Raid Saabne. Fast classification of handwritten on-line arabic characters. In *Soft Computing and Pattern Recognition (SoCPaR), 2014 6th International Conference of*, pages 312–318. IEEE, 2014.

[4] Guy Hadash, Einat Kermany, Boaz Carmeli, Ofer Lavi, George Kour, and Alon Jacovi. Estimate and replace: A novel approach to integrating deep neural networks with existing applications. *arXiv preprint arXiv:1804.09028*, 2018.

PHYSICS WITH FORWARD PROTONS AT RHIC

Tomáš Truhlář

1 Introduction

The physics program with forward protons at the Relativistic Heavy Ion Collider (RHIC) started in August 1990, when the PP2PP experiment [1] was proposed. The PP2PP was a stand alone experiment using eight Roman Pot detectors placed about 57 meters from interaction point at 2 o'clock RHIC position. In 2002, the first data were measured. The PP2PP experiment focused on measurement of proton-proton (pp) elastic scattering at $\sqrt{s} = 200$ GeV [2, 3], the highest center-of-mass energy at that time.

The elastic scattering is one of the diffractive processes involving exchange of IPomeron(s) between the interacting hadrons. Figure 34 graphically represents few classes of the diffractive processes with their corresponding leading order Feynman diagrams (Regge pictures): elastic scattering, single diffractive dissociation, and central diffraction without the dissociation of the forward-scattered protons. Corresponding schemes of event topology in the azimuthal angle φ and pseudorapidity η plane are shown as well.

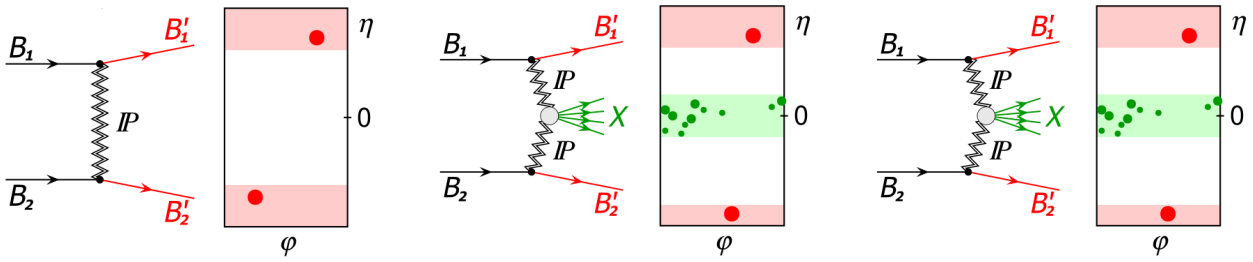

Figure 10: Leading order Feynman diagrams with corresponding schemes of event topology in the azimuthal angle φ and pseudorapidity η plane of the diffractive processes. From left: elastic scattering, single diffractive dissociation, and central diffraction without the dissociation of the forward-scattered protons. Taken from [4].

The PP2PP experiment was originally designed to study pp elastic scattering through the measuring of forward-scattered protons in Roman Pot detectors. In 2006, the PP2PP experiment joined the STAR experiment [5] enabling high-resolution tracking of charged particles in the Time Projection Chamber and precise particle identification through the measurement of $\mathrm{d}E/\mathrm{d}x$ and time of flight. Thanks to that, measurements of another diffractive processes such as single diffractive dissociation or central diffraction were possible.

2 Central exclusive production

Central Exclusive Production (CEP) is type of central diffraction without the dissociation of the forward-scattered protons where all particle are measured. At RHIC energies, the CEP through double IPomeron exchange (DIPE) is expected to be dominant. It is a process, where each colliding proton "emits" a IPomeron. The IPomerons fuse and produce a neutral central system with quantum numbers of vacuum. Moreover, the produced central system is well separated from forward-scattered protons by large rapidity gaps. Although the process is topologically very simple, it is theoretically very complex and rich in phenomena. The process is a combination of continuum and resonance production, see **??**. Therefore, there are significant interference effects between resonance and continuum production. In addition, significant rescattering effects via additional interaction between the protons are present.

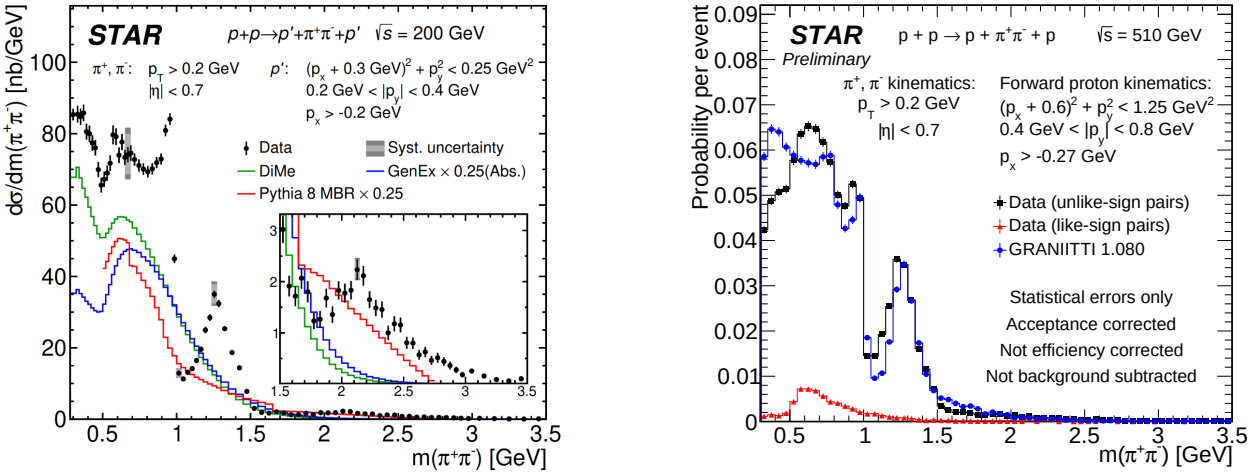

Figure 11: Left: Differential cross-section as a function of invariant mass of $\pi^+\pi^-$ pairs at $\sqrt{s} = 200$ GeV. Taken from [7]. Right: The acceptance corrected invariant mass spectrum of exclusively produced $\pi^+\pi^-$ pairs at $\sqrt{s} = 510$ GeV.

Since CEP through DIPE is gluon rich process, it is suitable to study strong interaction described by quantum chromodynamics (QCD). Moreover, it is also a potential source of glueballs, bound states consisting of only gluons. The experimental confirmation of the glueball would be yet another strong support for the validity of the QCD theory.

3 Results

In 2015 and 2017, the STAR experiment collected proton-proton collision data at $\sqrt{s} = 200$ and 510 GeV, respectively. All particles in the final state were fully measured. The forward-scattered protons were measured in the Roman Pot detectors and the central system was measured in the Time Projection Chamber and in the Time of Flight systems. This allowed full control of the interaction's kinematics and verification of its exclusivity.

Figure 11 (left) shows the most recent results of the CEP of $\pi^+\pi^-$ in pp collisions at $\sqrt{s} = 200$ GeV, the highest center-of-mass energies at which DIPE has been measured with the detection of the forward-scattered protons. The expected features are seen: drop at 1 GeV and the peak about 1.3 GeV. The first one should be due to negative interference of the continuum contribution by the $f_0(980)$ resonance. The second one is attributed to the $f_2(1270)$ resonance. Monte Carlo model predictions available at that time are shown as well. They are able to generate only the continuum production. Hence, they cannot fully describe the data.

Figure 11 (right) depicts the invariant mass distribution of selected $\pi^+\pi^-$ pairs at $\sqrt{s} = 510$ GeV. The data were compared to the new Monte Carlo event generator for high energy diffraction, GRANIITTI [6]. To do so, the results were corrected using acceptance corrections obtained from pure single particle STAR simulation and were normalized such that area under the distribution is equal to one. GRANIITTI generates both continuum and resonance contributions. Thus, the significant interference effects are taken into account. In addition, the significant rescattering effects are also embedded in GRANIITTI. Both data and GRANIITTI shows the expected features discussed above. GRANIITTI is able to describe the shape fairly well, especially above 0.8 GeV.

In Fig. 12 the invariant mass distribution of $\pi^+\pi^-$ pairs was differentiated in two regions of the difference of azimuthal angles between the forward protons ($\Delta\varphi$), where different Pomeron dynamics and rescattering effects are expected. The clear difference between the distributions can be seen: a suppression of $f_2(1270)$ and an enhancement at low invariant mass in $\Delta\varphi < 90°$ are seen. The sharp drops at $m(\pi^+\pi^-) < 0.6$ GeV for the $\Delta\varphi > 90°$ range should be due to the fiducial cuts applied to the forward-scattered protons. GRANIITTI is able to describe shapes of distributions quite well in both $\Delta\varphi$ regions.

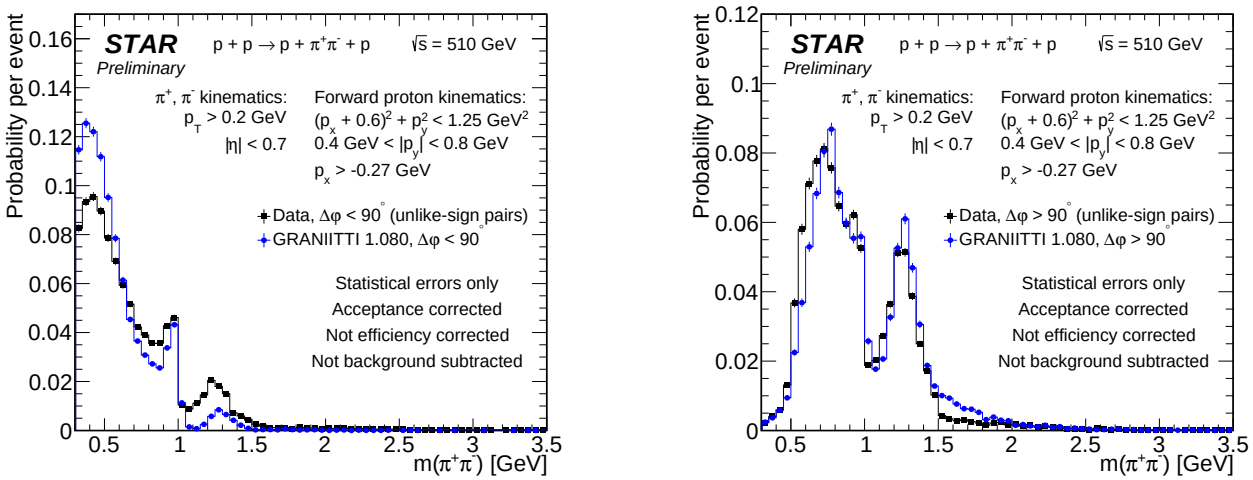

Figure 12: Acceptance corrected invariant mass spectra of exclusively produced $\pi^+\pi^-$ pairs at $\sqrt{s} = 510$ GeV differentiated in two regions of the difference of azimuthal angles between the forward protons: $\Delta\varphi < 90°$ (left) and $\Delta\varphi > 90°$ (right).

References

[1] W. Guryn, Total and elastic pp cross sections at RHIC. In *Proc. of the Fourth Workshop for RHIC*, pages 11, 1990

[2] S. Bultmann, et al. (PP2PP Collaboartion), First measurement of proton proton elastic scattering at RHIC. In *Physics Letters B, vol. 579*, pages 245-250, 2004.

[3] S. Bultmann, et al. (PP2PP Collaboartion), First measurement of A_N at $\sqrt{s} = 200$ GeV in polarized proton–proton elastic scattering at RHIC. In *Physics Letters B, vol. 632*, pages 167-172, 2006.

[4] R. Sikora, Measurement of the diffractive central exclusive production in the STAR experiment at RHIC and the ATLAS experiment at LHC. PhD. thesis, AGH University of Science and Technology, Cracow, 2020.

[5] K.H. Ackermann, et al. (STAR Collaboration), STAR detector overview. In *Nuclear Instruments and Methods in Physics Research Section A, vol. 499*, pages 624-632, 2003.

[6] M. Mieskolainen, GRANIITTI: A Monte Carlo Event Generator for High Energy Diffraction. *arXiv preprint arXiv:1910.06300*, 2019.

[7] R. Sikora, et al. (STAR Collaboration), Measurement of the central exclusive production of charged particle pairs in proton-proton collisions at $\sqrt{s} = 200$ GeV with the STAR detector at RHIC. In *Journal of High Energy Physics, vol. 2020, no. 7*, pages 46, 2020.

INCLUSIVE DIJET STUDIES AT THE ATLAS EXPERIMENT

Ota Zaplatilek

1 Introduction

Jets are introduced in quantum chromodynamics (QCD) as collimated sprays of hadron particles after quark/gluon fragmentation. The quarks and gluons are produced in a short-distance scattering process with no chance of direct observations. However, the jets can be matched to the original quarks/gluons before fragmentation. The jet cross-section measurements provide valuable information about the QCD, the proton structure, the parton distribution functions (pdf), and the strong coupling constant, α_s.

The article deals with a dedicated study of the next-to-leading (NLO) calculations of perturbative QCD (pQCD) at the one-loop level of Feynman diagrams for two-dimensional inclusive dijet cross-section measurement as a function of dijet mass m_{jj}, and the half absolute rapidity separation of leading and subleading jets, $y^* = \frac{1}{2}|y_1 - y_2|$. The variable $y^\star$ distinguishes the central and forward dijet systems with low and high values. Furthermore, the $y^\star$ variable is sensitive for New Physics (NP), since most New Physics theories predict different shapes of distributions at low $y^\star$ values. The NLO prediction going to be compared with the data recorded with the ATLAS detector at the Large Hadron Collider (LHC) during the LHC run 2 phase.

2 Selection criteria

The two leading jets (with the highest transverse momentum p_T) define the inclusive dijet system as the vector sum of the four-momenta. The inclusive dijet system will be called the dijet. Each dijet is tested according to the selection criteria listed in Tables 2.

Selection criterion		Applied condition
jet multiplicity	n_{jets}	$n_{\text{jets}} \geq 2$
leading jet transverse momentum	$p_{\text{T},1}$	$p_{\text{T},1} > 75$ GeV
sub-leading jet transverse momentum	$p_{\text{T},2}$	$p_{\text{T},2} > 75$ GeV
leading jet rapidity	$\lvert y_1 \rvert$	$\lvert y_1 \rvert < 3.0$
sub-leading jet rapidity	$\lvert y_2 \rvert$	$\lvert y_2 \rvert < 3.0$
dijet half rapidity separation	$y^\star = \frac{1}{2}\lvert y_1 - y_2 \rvert$	$y^\star < 3.0$
dijet scalar sum of transverse momentum	$H_{\text{T}}^{\text{two}} = p_{\text{T},1} + p_{\text{T},2}$	$H_{\text{T}}^{\text{two}} > 200$ GeV

Table 2: Selection criteria for inclusive dijet system identification.

3 Data and theoretical prediction

Analysed data are collected by the ATLAS detector[1, 2] using proton-proton collisions at $\sqrt{s} = 13$ TeV in the years 2015-2018 during the LHC run 2 phase with an integrated luminosity of 139 fb^{-1}.

The measured data used be to compared to Monte-Carlo (MC) Pythia 8 (version 8.186 [3]), which includes leading order (LO) pQCD matrix elements for $2 \rightarrow 2$ process. However, it was found as Pythia, the LO MC generator, miss model forward jets, which are propagated to the dijets system by construction. An observed miss modelling effects lead

up to 50% disagreement between the measured data to MC prediction for the forward dijet system ($2.5 < y^{\star} < 3.0$). Thus high orders of pQCD need to be considered.

The next-to-leading order (NLO) prediction was calculated using NLOJET++ 4.1.3 [4] and APPLGRID utility [5] for a convolution of matrix elements with the pdf. It was considered various pdf sets (CT, NNPDF, MMHT, MSHT,MSTW) implemented in LHAPDF6 library [**?**] and two choices for both the renormalization scale, μ_R, and the fragmentation scale, μ_F. The nominal scale $\mu_R = \mu_F = p_{\mathrm{T}} \exp(0.3y^{\star})$, where p_{T} notes leading jet transverse momentum, and $y^{\star}$ half-rapidity separation, was proposed in Ref. [6] and applied also in previous ATLAS dijet measurements at 7 TeV [7] and 13 TeV [8]. The alternative choice of scale is a dijet mass $\mu_R = \mu_F = m_{\mathrm{jj}}$.

The main sources of NLO systematics uncertainties were evaluated, namely: scale, parton distribution function (pdf) and α_s. The scale uncertainty provides information about missing terms of perturbative calculus. The scale uncertainty was evaluated as an envelope of independent upward and downward variations in both directions by factor of 2 for fragmentation and renormalization scales, μ_F, μ_R, after their propagation through the NLO calculations. The pdf uncertainty comes from N independent eigenvectors for each pdf set as recommended by the PDF4LHC group [9]. The α_s uncertainty is taken as the envelope of the uncertainties derived from two pdf sets that differ in the alpha value only as $\alpha_s \pm \Delta\alpha_s = 0.118 \pm 0.001$ and their propagation through the NLO calculations. Finally, the total uncertainty is estimated from squares of individual sources discussed above.

4 Results for next-to-leading order calculations

First, the NLO calculations were compared with the ATLAS data and previous theoretical prediction of the LO MC Pythia 8. As expected, the NLO calculations improve the data to theory agreement (compared to the LO MC Pythia8) for forward (di)jets. Small deviations from the NLO to the ATLAS data are still observed at low dijet masses, which are affected by the missing non-perturbative corrections. Due to the ATLAS collaboration policy, it is not allowed to show unpublished data here.

Further, the main sources of systematic uncertainties for NLO predictions were estimated as discussed in Section 3. The relative NLO systematic uncertainties using pdf of CT18 can be found in Figure 13 for the two demonstrative regions of $0.0 < y^{\star} < 0.5$ (central dijet) and $2.5 < y^{\star} < 3.0$ (forward dijet). The dominant systematic NLO uncertainty comes from scale uncertainty, which becomes very asymmetric, at the level of a few (tens) percents for upward (downward) uncertainties using the nominal scale of $\mu_R = \mu_F = p_{\mathrm{T}} \exp(0.3y^{\star})$. The scale uncertainty rises up to 50% at the edge of fiducial space with of $2.5 < y^{\star} < 3.0$ and high dijet mass, m_{jj}. The scale uncertainty can be decreased using higher pQCD calculations only. The second dominant source refers to the pdf uncertainty, which is evaluated for CT18 pdf in Figure 13. However, the pdf uncertainty was investigated for various pdf sets. The pdf uncertainties have been improved significantly with new published pdf sets (CT18, MHSH20, NNPDF40) that stay below 10% in each dijet mass and $y^{\star}$ bin. The lowest pdf uncertainty was found for NNPDF40 at a level of 1–4% for each dijet mass and $y^{\star}$ bin. The last α_s uncertainty remains below 3%.

5 Conclusion

The inclusive dijet cross-section is measured using calibrated anti-k_{T} jets with $R = 0.4$ radius in proton-proton collisions at $\sqrt{s} = 13$ TeV at the ATLAS experiment. The cross-section is measured double differentially for dijet mass, m_{jj}, and half rapidity separation of leading and subleading jets, $y^{\star}$. The observed fiducial space covers m_{jj} from 300 GeV to 10 TeV, $y^{\star} < 3.0$. The measurement is compared with fixed-order NLO calculations of pQCD considering statistic and systematics uncertainties of the NLO calculations, namely: scale, pdf and α_s sources. The dominant NLO computation uncertainty comes from the factorization and the renormalization scales. The pdf uncertainty is improved significantly using the latest pdf sets, the lowest pdf uncertainty is achieved with the NNPDF40.

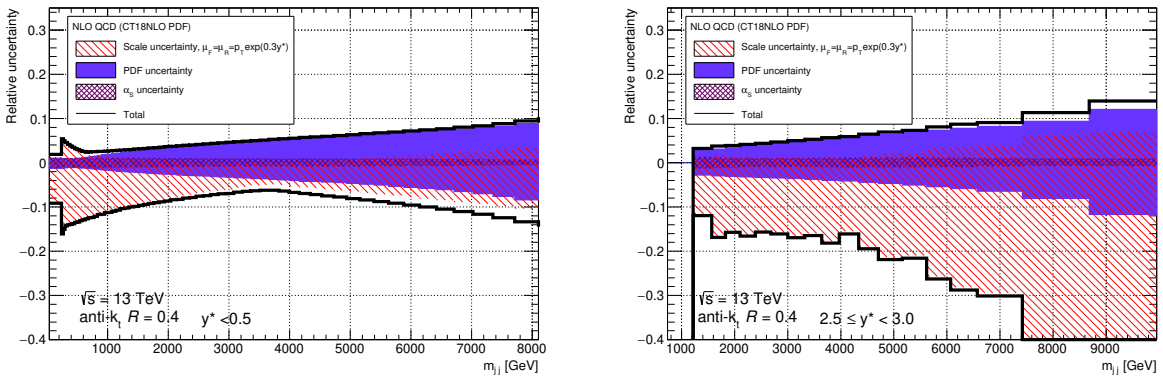

Figure 13: Relative systematic uncertainties of NLO calculations considering three main sources: scale (red), pdf (blue) and α_s (magenta) and total uncertainties for inclusive dijet mass cross-section in two $y^\star$ bins: $0.0 < y^\star < 0.5$ and $2.5 < y^\star < 3.0$ (right). The nominal fragmentation and renormalization scales of $\mu_F = \mu_R = p_{\mathrm{T}} \exp(0.3y^\star)$ are applied. The pdf uncertainty is derived using CT18 eigenvectors.

References

[1] ATLAS Collaboration, *The ATLAS Experiment at the CERN Large Hadron Collider*, JINST 3 (2008) S08003.

[2] ATLAS Collaboration, *ATLAS Insertable B-Layer Technical Design Report*, ATLAS-TDR-19, 2010.

[3] T. Sjöstrand, S. Mrenna and P. Skands, `A brief introduction to PYTHIA 8.1`, Comput. Phys. Commun. 178 (2008) 852, arXiv: 0710.3820 [hep-ph]

[4] Z. Nagy, *Next-to-leading order calculation of three jet observables in hadron hadron collision*, Phys. Rev. D 68 (2003) 094002, arXiv: hep-ph/0307268.

[5] T. Carli et al., *A posteriori inclusion of parton density functions in NLO QCD final-state calculations at hadron colliders: The APPLGRID Project*, Eur. Phys. J. C 66 (2010) 503, arXiv: 0911.2985 [hep-ph].

[6] S. D. Ellis, Z. Kunszt and D. E. Soper, *Two jet production in hadron collisions at order α_s^3 in QCD*, Phys. Rev. Lett. 69 (1992) 1496.

[7] ATLAS Collaboration, *Measurement of dijet cross-sections in pp collisions at 7 TeV centre-of-mass energy using the ATLAS detector* JHEP05(2014)059, arXiv:1312.3524 [hep-ex].

[8] ATLAS Collaboration, *Measurement of inclusive jet and dijet cross-sections in proton-proton collisions at $\sqrt{s} =$ 13 TeV with the ATLAS detector*, JHEP 05 (2018) 195, arXiv:1711.02692 [hep-ex].

[9] J. Butterworth et al., *PDF4LHC recommendations for LHC Run II*, J. Phys. G 43 (2016) 023001, arXiv: 1510.03865 [hep-ph].

APPLICATION OF THE DEEP MACHINE LEARNING FOR THE STUDIES OF THE MUON AIR-SHOWER COMPONENT USING THE PIERRE AUGER SURFACE DETECTOR DATA

Margita Majerčáková

1 Introduction

Cosmic rays were discovered more than a century ago. Since then, the properties of cosmic particles have been incessantly studied using a large variety of experimental techniques. Despite establishing with an unprecedented precision many important characteristics of cosmic radiation, the most fundamental questions about its origins remain unanswered. In particular, it is not understood which processes and objects can accelerate the most energetic particles in the Universe to their energies, exceeding those achieved at the man-made accelerators by several orders of magnitude. The study of these particles is complicated by their rarity, thus experiments with an area of a few thousand square kilometres should be used for collecting sufficient statistics on their properties.

The largest astroparticle experiment currently operating is the Pierre Auger Observatory, located in Argentina. The Observatory is using a hybrid detection technique by simultaneously observing air showers with ground-based detectors and fluorescence telescopes. One of the main aims of the Observatory is the discovery of the sources of the ultra-high energy cosmic rays (UHECR) through analysis of their arrival directions. To account correctly for the influence of the galactic and extragalactic magnetic fields on the UHECR propagation, a knowledge of the mass of primary particles on an event-by-event basis is required. The strongest indicators of the primary particle mass are the atmospheric depth at which the number of particles in the shower reaches its maximum and the number of muons registered with the surface detectors. The former indicator is directly accessible with the optical detectors having a duty cycle of 15% only. Therefore, the use of the muon content and thus the statistics of the surface detector with its nearly 100% duty cycle is a must for obtaining mass-sensitive information for the highest energy events. However, water Cherenkov surface detectors used in Auger are not designed to record separately muon and electromagnetic components of air showers. For overcoming this problem, the Auger detector is being currently upgraded with scintillator detectors and radio antennas which can help to disentangle the muonic and the electromagnetic components. As a complementary tool, the Pierre Auger Observatory has recently started investigating the potential applications of machine learning methods. After their validation, it might become feasible to extract muon content from the surface detector data accumulated by the Observatory since the beginning of its operation [2].

2 The study of muons with the deep neural networks

The number of muons in air showers is one of the most important parameters linked to the mass of a primary particle. The knowledge of the mass composition is the key input required for verifying the astrophysical models describing the acceleration and propagation of cosmic rays and for understanding the properties of hadronic interactions in the phase space regions inaccessible to the man-made accelerators. Two types of neural networks were used in the analysis performed. The first one was the method for the prediction of a total muon signal with the deep neural network. The second part deals with the recurrent neural networks, which are used to predict the muonic component in individual time bins. With the latter method, an accurate estimation of muon signal and its arrival time distributions is possible for certain ranges of primary energy, zenith angles and distances to the core. The architecture of the neural network

can be seen in Fig. 14. Our tests have shown that the results are nearly independent of the choice of the hadronic interaction model. A preliminary application to the Auger data indicates that the muon deficit in simulations is present at a wide range of distances to the core. The results of this application is shown in Fig. 15.

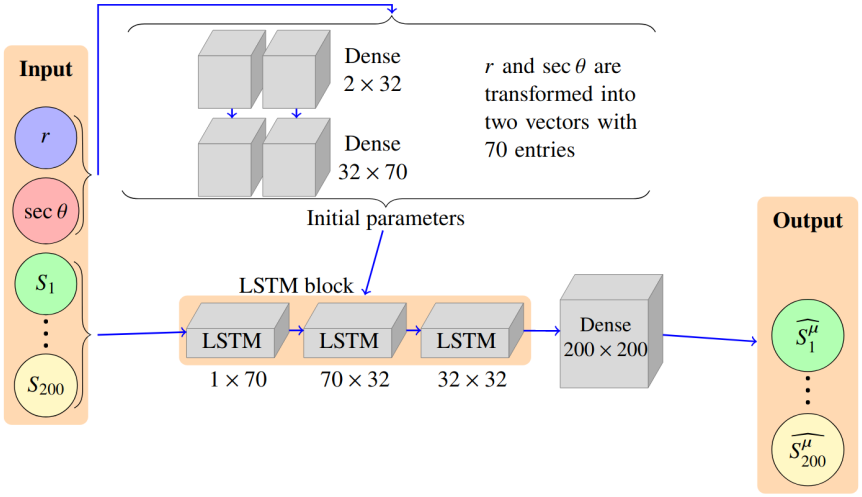

Figure 14: The architecture of the neural network used to determine temporal muon distribution [1].

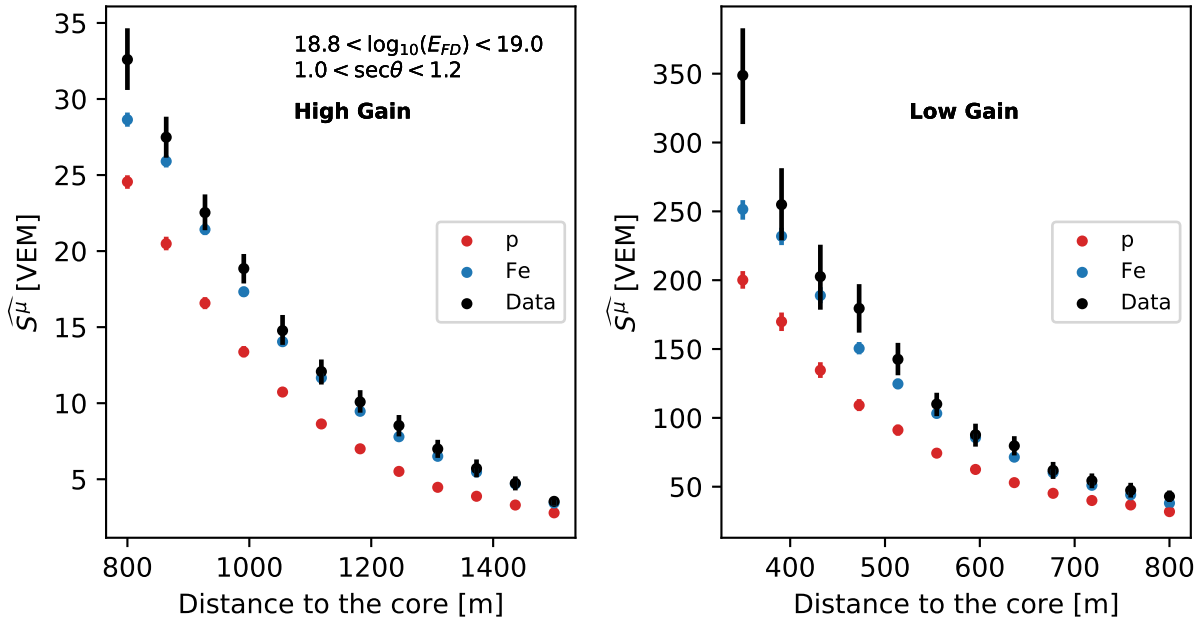

Figure 15: The muon trace integral as a function of distance, compared for data and simulations. The predicted muon trace integral is plotted for simulations [2].

References

[1] The Pierre Auger Collaboration. Extraction of the muon signals recorded with the surface detector of the Pierre Auger Observatory using recurrent neural networks. In *Journal of Instrumentation*, 2021.

[2] Margita Majerčáková. Master's Thesis. Application of the deep machine learning for the studies of the muon air-shower component using the Pierre Auger Surface Detector data. Czech Technical University. 2022.

CLUSTER SUNRISE

Zdenek Hubacek

1 Introduction

This is a follow up on the contribution presented at the previous Workshop in 2020 [1]. Our small computing cluster at the department, `sunrise` [2], has been recently upgraded with new servers. The details of the upgrade and the PBS Professional tools used to manage its resources are presented in this contribution.

2 Computing Cluster sunrise

A small computing cluster `sunrise` (`sunrise.fjfi.cvut.cz` or IP address `147.32.5.210`) is operated at the Department of Physics of the Faculty of Nuclear Sciences and Physical Engineering of the Czech Technical University in Prague. The cluster, physically located in the Brehova 7 building basement, has as of June 2022 about 650 CPU cores. The pool of CPUs has been recently upgraded with 6 new servers (`sunset29-34`) each with AMD EPYC3 7543@2.8GHz processors (64 HT cores and 256 GB RAM). All available nodes currently run CENTOS7 operating system. Relevant user environments can be setup for example from `cvmfs` areas or by using containers. A disk array with about 200 TB of disk space is connected to the cluster and a new SSD-based disk array is going to be connected soon. All new working nodes and the disk-arrays are now connected by 10GE network, however the main connectivity to the outer world is still limited by the network elements outside of the department.

The resources are available to everyone at the department. Please contact the administrators for creating a computing account.

3 PBSPro

The PBS Professional 19.1.3 (PBSPro) [3] batch system is used to manage the computing resources. Users log into the main login node `sunrise.fjfi.cvut.cz` and submit their jobs (tasks) from there to the batch system. The system manages all worker nodes (`sunset01` - `sunset34`, some older worker nodes are retired and not all numbers are used at this moment) and takes care of distribution of jobs to them automatically. The basic commands and their use are presented in the talk slides. Currently running jobs could be monitored in multiple ways. A new webpage overview is provided [4].

4 Summary and Bonus

A small computing cluster is operated for users at the Department of Physics of the FNSPE CTU in Prague. PBSPro batch system is used for managing the computing resources and for distributing user jobs among the worker nodes of the cluster. All users are encouraged to use the cluster following some simple rules and the common sense.

For fun, the `animate` LaTeX package is presented on top of the `Beamer` standard package used for presentations. This environment works only for selected PDF viewers.

References

[1] Z. Hubacek, PBSPro batch system na sunrise, https://indico.fjfi.cvut.cz/event/123/contributions/2734/, accessed June 2022

[2] Computing cluster sunrise: https://nms.fjfi.cvut.cz/wiki/Sunrise.fjfi.cvut.cz, accessed in June 2022

[3] Altair Engineering, Inc., documentation available at https://community.altair.com/community?id=altair_product_documentation, accessed June 2022

[4] Sunrise grafana web summary http://sunrise.fjfi.cvut.cz/grafana/d/batch/batch?orgId=1, accessed June 2022

INCOHERENT PHOTOPRODUCTION OF J/ψ WITH ALICE

David Grund

1 Introduction

Measurements of photoproduction of vector mesons in ultra-peripheral collisions of heavy ions constitute a powerful tool to study the nuclear substructure thanks to the fact that cross sections of such processes can be directly related to the parton distribution functions (PDFs) of nucleons. Using data from Run 2 of the LHC, where lead ions were collided at the center-of-mass energy of 5.02 TeV, the PDFs can be probed in the region of Bjorken-x ranging from 10^{-5} to 10^{-2}, where the substructure of nucleons is dominated by gluons. This enables us to study the related low-x phenomena such as gluon saturation or nuclear shadowing.

In ultra-peripheral collisions, the nuclei are collided at the impact parameter that is larger than the sum of their radii, which ensures that any hadronic interactions are suppressed owing to the short range of the strong interaction. This means that the interaction has to be induced by a quasi-real photon emitted by one of the nuclei. In the so-called dipole picture, the photon can later fluctuate into a quark-antiquark pair that interacts with the other nucleus via exchange of a Pomeron. As a result, a vector meson such as J/ψ can be created, which carries information about the target gluon density.

Photoproduction can be classified as coherent or incoherent based on what part of the target nucleus the photon interacts with. If it interacts with the nucleus as a whole, it is referred to as coherent and the produced J/ψ typically has a transverse momentum of a few tens of MeV, $\langle p_{\mathrm{T}} \rangle \sim 60$ MeV [1]. On the other hand, if the photon interacts with a selected nucleon, the target nucleus is likely to be dissociated and the J/ψ transverse momentum can reach several hundreds of MeV, $\langle p_{\mathrm{T}} \rangle \sim 500$ MeV [1]. This process is called incoherent photoproduction and the $|t|$-dependence of the incoherent photonuclear cross section, where t is the momentum transfer in target nucleus vertex, is sensitive to geometric fluctuations of gluons in the transverse plane. Should subnucleonic fluctuations be significant, the phenomenological models predict that the photonuclear cross section would fall much less rapidly with increasing $|t|$ [5].

2 The analysis of $|t|$-dependence of incoherent J/ψ photoproduction at $\sqrt{s_{\mathrm{NN}}} = 5.02$ TeV with ALICE

In the presented analysis, we study dimuon decays of incoherently photoproduced J/ψ mesons at midrapidity, $|y| < 0.8$, using the following central-barrel ALICE detectors: the ITS, TPC and TOF. In addition, the AD, V0 and ZDC forward detectors are used to reject events with potential hadronic contamination and to measure emitted forward neutrons. Particle identification was provided by measuring specific energy losses, $\mathrm{d}E/\mathrm{d}x$, in the TPC.

We analyze events from the periods LHC18q and LHC18r triggered with the central CCUP31 trigger. This data set corresponds to the integrated luminosity of 231.9 $\mu\mathrm{b}^{-1}$. Measuring dimuon decays means that we look for very clean events where only two back-to-back lepton tracks are present in otherwise empty detectors. After the application of necessary selection criteria, 720 events with p_{T} in the range from 0.2 to 1.0 GeV/c were found. The signal extraction was performed by fitting the invariant mass distribution with a combination of a double-sided Crystal Ball function and an exponential to account for background, see Fig. 16.

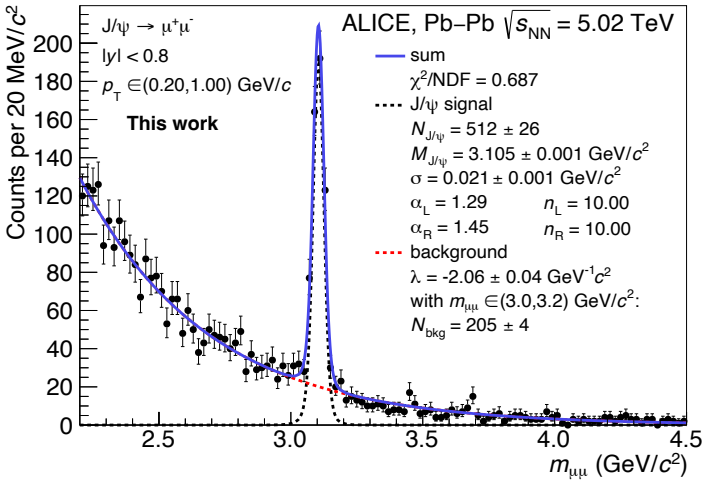

Figure 16: Invariant mass fit of events with $0.2 < p_{\mathrm{T}} < 1.0$ GeV/c.

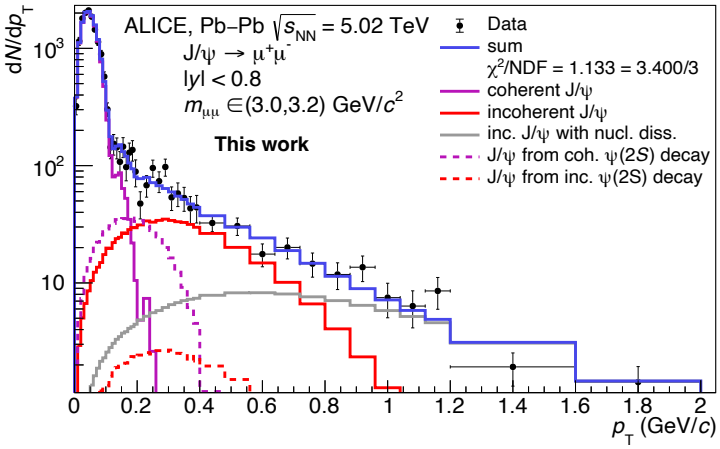

Figure 17: Fit of the transverse momentum distribution of events with $p_{\mathrm{T}} < 2.0$ GeV/c.

It was found that 512 events from the incoherent-enriched sample can be considered J/ψ candidates. It was thus decided that 5 bins will be created in this p_{T} range, in which the $|t|$-dependence will be studied, so that the signal is uniformly distributed among the bins. However, not all these events are in fact incoherently photoproduced J/ψ because the signal is also subjected to contamination from coherent J/ψ production (at lowest p_{T}) and feed-down from photoproduction of excited charmonium states, $\psi(2S)$. These contributions are separated by means of fitting the transverse momentum distribution in the range of $p_{\mathrm{T}} < 2$ GeV/c, see Fig. 17, after the background is first subtracted in each bin via invariant mass fits.

The acceptance and efficiency of the signal reconstruction was calculated exploiting MC data sets anchored to the periods LHC18qr and simulated using the STARlight generator [2]. The efficiency of the V0 and AD vetoes was determined studying the distribution of events into ZN classes and applying the correction factors obtained from the analysis of events from 2015, where no AD veto was applied. Since no significant migration of events across the bins was observed, the unfolding of the signal was not performed.

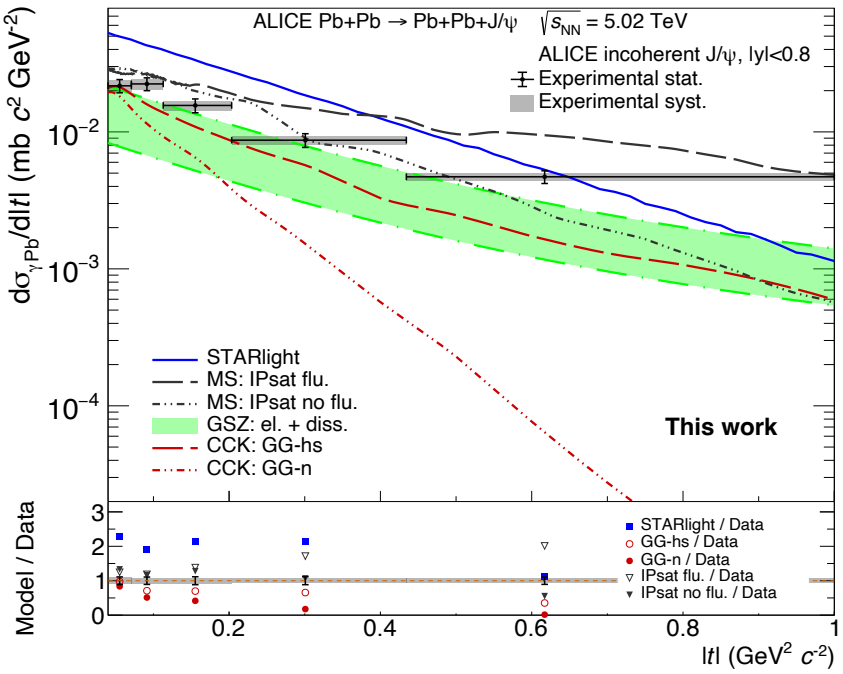

Figure 18: Measured $|t|$-dependence of the incoherent photonuclear cross section in comparison with predictions of phenomenological models [2, 3, 4, 5] and the ratios of model predictions to measured points. The error bars show statistical uncertainties while systematic uncertainties are displayed as shaded areas.

3 Results

The obtained $|t|$-dependence in comparison to predictions of several phenomenological models [2, 3, 4, 5] is depicted in Fig. 18. The uncertainty of the measurement is dominated by the statistical error ($\approx 10\%$). Even though none of the models correctly reproduces the overall normalization, the cross section does not appear to decrease rapidly at high $|t|$, which suggests that the measured slope might favor the phenomenological scenarios where subnucleonic fluctuations are present.

References

[1] ALICE Collaboration: First measurement of the $|t|$-dependence of coherent J/ψ photonuclear production (2021). https://arxiv.org/abs/2101.04623.

[2] S.R. Klein, J. Nystrand, J. Seger, Y. Gorbunov, J. Butterworth, Comp. Phys. Comm. 212 (2017) 258. https://starlight.hepforge.org.

[3] H. Mäntysaari and B. Schenke: Probing subnucleon scale fluctuations in ultraperipheral heavy ion collisions (2017). https://inspirehep.net/literature/1519841.

[4] V. Guzey, M. Strikman and M. Zhalov: Nucleon dissociation and incoherent J/ψ photoproduction on nuclei in ion ultraperipheral collisions at the Large Hadron Collider (2019). https://inspirehep.net/literature/1684846.

[5] J. Cepila, J. G. Contreras and M. Krelina: Coherent and incoherent J/ψ photonuclear production in an energy-dependent hot-spot model (2018). https://inspirehep.net/literature/1634637.

LONGITUDINAL PROFILES OF THE HIGHEST ENERGY COSMIC-RAY AIR SHOWERS MEASURED AT THE PIERRE AUGER OBSERVATORY

Nikolas Denner

1 Introduction

The Pierre Auger Observatory is the world's largest cosmic-ray detector, spreading over an area of about 3000 km^2 [**?**]. It uses a so-called hybrid detection of cosmic-ray showers employing two different types of detectors, namely the surface detector (SD), measuring particles that reached the surface using an array of 1660 water-Cherenkov stations, and the fluorescence detector (FD), measuring fluorescence light emitted by the shower particles in the atmosphere using 27 fluorescence telescopes distributed at 4 sites and overlooking the SD array. The detection of fluorescence light emitted by the shower makes it possible to reconstruct its longitudinal profile, which is defined as the dependence of the energy deposited by the shower on the slant depth. The reconstruction gives us two important properties, the depth of the shower maximum X_{max} and the calorimetric energy E_{cal}, from which the total shower energy E_{tot} can be estimated. These properties are then used for the analysis of the mass composition of the highest energy cosmic rays.

For the analysis of the Observatory data detected by both types of detectors, one reconstruction method, referred to in the following text as the standard hybrid reconstruction method, is conventionally applied. This method uses full FD reconstruction of the detected signal and combines it with information from at least one SD station closest to the shower core to reconstruct the shower geometry [**?**]. After the reconstruction, the number of analysed events is reduced by the application of selection cuts. These cuts can sometimes also remove events that could be analysed, but are not reconstructed with good enough precision. This work investigates the possibility to combine the standard method with two alternative reconstruction methods of showers seen by the fluorescence telescopes. The motivation behind this research is the increasement of the number of events used for the analysis of the ultra-high energy cosmic-ray mass composition. Due to the small flux of cosmic rays at the end of their energy spectrum [**?**], an increase of the data set by dozens of highest energy events would correspond to more than a year of data taking.

The two alternative reconstruction methods considered in this work are the hybrid reconstruction using the SD geometry and the stereo reconstruction. The hybrid reconstruction using the SD geometry employs full reconstruction of the SD signal to estimate the geometry of the shower, while the FD signal is used for the estimation of the longitudinal profile. This has an advantage in case of reconstruction of showers that fell further from the fluorescence telescopes. The stereo reconstruction method [**?**] estimates the shower axis and with it the shower geometry by finding the best fitting axis from combination of shower-detector plane[1] fits from all triggered telescopes. This method hence needs more than one fluorescence telescope to observe the shower. However, it does not use the SD signal and so it is able to reconstruct showers that fell outside of the SD array. The analysis in this work is divided into two parts. First, we studied the differences between the three methods applied on simulated showers, and second, we combined the results of the three methods applied on real Observatory data.

[1] Shower-detector plane is a plane reconstructed using the signal on triggered fluorescence telescope pixels.

2 Analysis of simulated showers

In the case of simulated showers, we first studied the differences in reconstructed X_{max} and E_{cal} between the standard hybrid method and each of the alternative methods on identical selected[2] Monte Carlo (MC) generated events reconstructed by identical FD sites. The differences were studied as functions of the shower distance, the MC X_{max} and the MC shower energy and all of these dependencies were fitted by a constant function, showing the average shifts between the methods. An acceptable difference of the reconstructed property was considered a difference in the X_{max} of less than 5 g/cm^2. Two exemplary graphs representing this study are shown in Figure 19. From this analysis, we estimated the correction factor that needs to be applied on the SD-geometry reconstructed X_{max} as 5 g/cm^2 and on the stereo-reconstructed X_{max} as -1 g/cm^2. Concerning the E_{cal}, there was no need to apply any correction factors as the differences between the methods were lower than 5%, which corresponds to a shift in the X_{max} of about 1.2 g/cm^2.

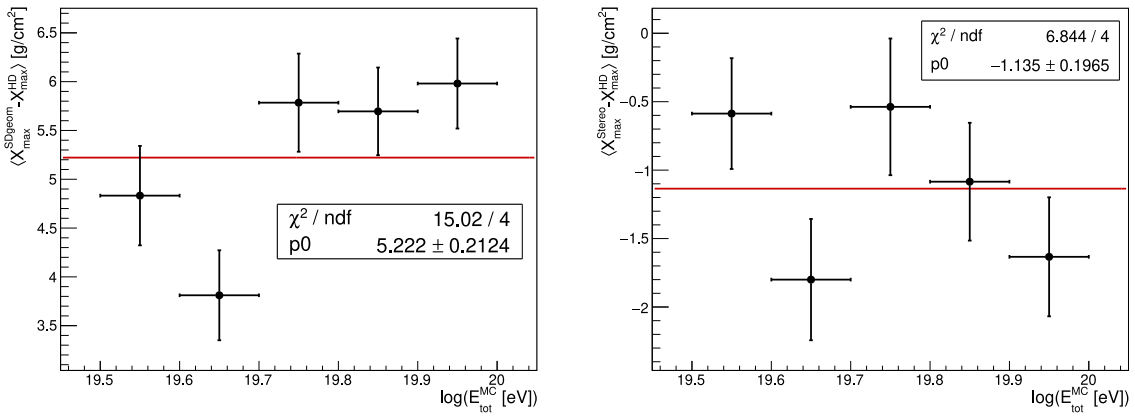

Figure 19: Mean value of the difference of the X_{max} reconstructed with the standard hybrid method and the reconstruction using the SD geometry (left) and the standard hybrid and the stereo methods (right) in $\log_{10}(E_{\mathrm{tot}}/1\ \mathrm{eV})$ bins fitted by a constant function.

In the second part of the study of simulated showers, we analysed the biases[3] and resolutions of X_{max} and E_{cal} of all selected events. The biases of the X_{max} reconstructed using the alternative methods were shown with and without the correction factors applied. We concluded that after the application of the correction factors for the X_{max}, the differences in biases between all three methods are within the acceptable bounds of 5 g/cm^2 and the resolutions of the alternative methods do not worsen the overall resolution by a significant amount. These conclusions together with the first part of the simulated shower analysis imply that the properties reconstructed using the three different methods can be combined together without considerably biasing the results.

3 Combination of the reconstruction methods

In the case of real data, we analysed all selected events reconstructed using the standard hybrid method (284 events), additional selected events reconstructed using the SD geometry (40 events) and to these two disjoint sets of events additional selected events reconstructed using the stereo method (221 events). In this way, we obtained a complete set of unique events reconstructed using the three different methods. However, due to technical difficulties, we were not able to obtain a full set of events reconstructed using the standard hybrid method. This means that the number of additional events is distorted because with the increasing number of standardly reconstructed events, the number of unique events added by the alternative methods might decrease. Yet, the number of additional events should still be more than 10% corresponding to several years of data taking of showers for standard X_{max} analysis.

[2]This selection refers to the application of selection cuts on the reconstructed events.

[3]In this context, bias means the difference between the MC-generated and reconstructed property.

Although the number of events added by the alternative methods was distorted due to the previously mentioned reason, we studied the distributions of the X_{max} in the highest energy bins, because the total number of events in each bin should not decrease even after adding the missing standardly reconstructed events. In this study, we were mostly interested in the number of events in the energetic bin between $10^{19.6}$ eV and $10^{19.7}$ eV, as this is the first range of energies which is not conventionally considered as an individual bin for the X_{max} analysis due to the number of events in this bin being lower than 40. As can be seen in Figure 20, this bin cannot be considered individual from our analysis even after using the additional methods. Nevertheless, there are still a few ways to improve our analysis and make more precise conclusions about the number of additional events and the X_{max} distributions.

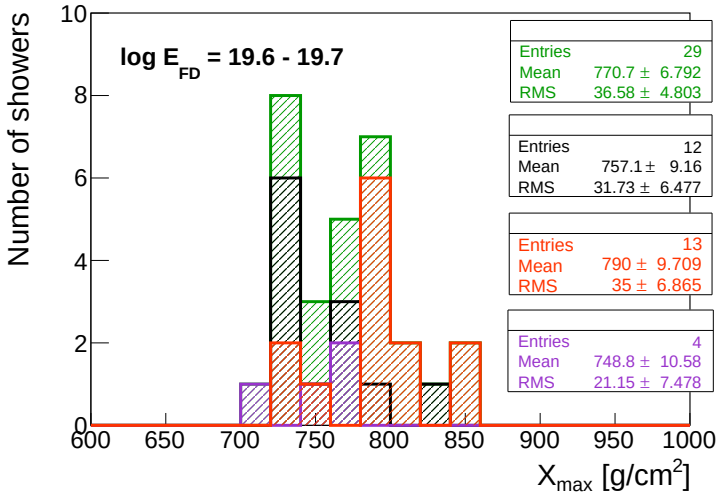

Figure 20: Distribution of the X_{max} reconstructed using the standard hybrid method (black), the SD geometry method (violet) and the stereo method (orange) and the combined distribution from all three methods (green) in energetic bin between $10^{19.6}$ eV and $10^{19.7}$ eV.

DEVELOPMENT OF BARREL HADRONIC CALORIMETER FOR ATHENA

Leszek Kosarzewski

1 ATHENA experiment

ATHENA [1] is one of the proposed designs for the detector to be built as part of the Electron Ion Collider (EIC) project. The idea was to design a high performance, general purpose detector featuring a superconducting magnet with variable magnetic field settings. It was based on the goals defined by the EIC Yellow Report and the reference detector outlined there [4]. The other designs are CORE [2] and ECCE [3]. ECCE Design was recommended for construction by the Detector Proposal Advisory Panel.

The purpose of EIC and it's detectors is to study the structure of nuclei and nucleons with a very high precision. Furthermore it will allow to study spin of nucleons and possible signatures of parton saturation. This will be done by performing collisions of $e + p$ and $e + A$ at energy up to 18 GeV for electrons and 275 GeV per nucleon for p or A. When built, EIC will be the only such machine ever constructed.

The ATHENA design will feature both MAPS silicons sensor and GEM based trackers with high momentum resolution of $\sim 1\%$ in the central barrel region as well as low material budget. Tracking in the forward (p or A-going) and backward directions is also envisioned. In addition, various detectors for particle identification will be used, like dual radiator RICH, high-performance DIRC [6] or AC-coupled LGAD based TOF [5]. Finally, a set of electromagnetic and hadronic calorimeters will be built providing energy measurements at central, forward and backward rapidities. Overall, the acceptance of the detector with tracking is planned to be $3.8 < \eta < 3.75$. This translates to $Q^2 > 1$ GeV^2 and $0.01 < y < 0.95$ for the deep inelastic scattering (DIS) measurements at the highest collision energy as illustrated in Fig. 34.

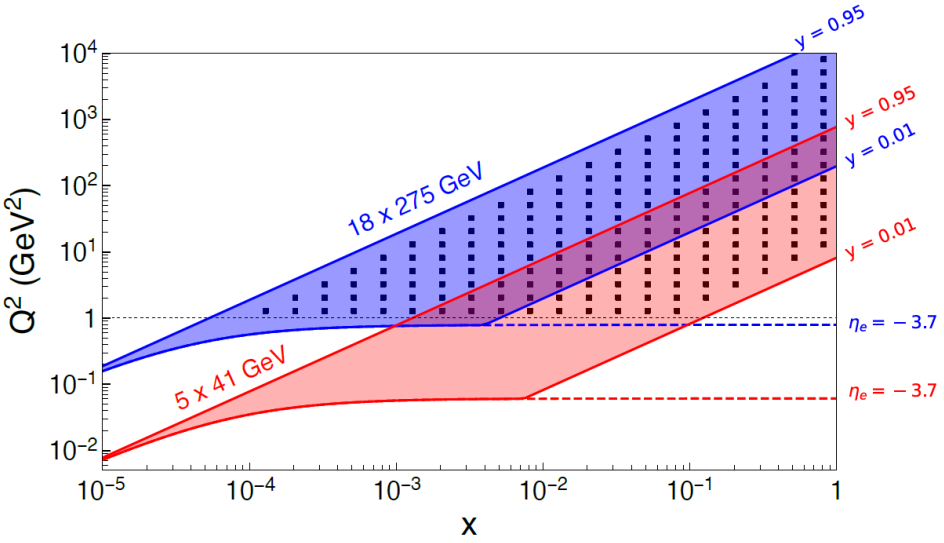

Figure 21: Acceptance of ATHENA detector for DIS measurements.

2 Barrel hadronic calorimeter development

Barrel hadronic calorimeter for ATHENA is located outside the magnet solenoid, which means that it will serve as a tail-catcher. Since, $\sim 70\%$ of hadrons will start showering in the material located before the calorimeter, it can measure only a fraction of the hadronic shower. Thus it will need to work in tandem with a hybrid Pb/SciFi and silicon imaging EM calorimeter.

The work on development of barrel hadronic calorimeter consisted of implementing a realistic geometry. The geometry description was adjusted to make use of STAR barrel EM calorimeter scintillating tiles [7]. These tiles have size of 0.05×0.05 in η and ϕ respectively. The calorimeter will provide acceptance of $-1 < \eta < 1$. The geometry was implemented in DD4hep [8], which is a flexible detector description framework with interfaces to Geant4 [9] and various MC event generators.

This was done and tested using simulated samples pions, protons and neutrons respectively. The data was reconstructed using Juggler framework.

3 Next steps

Further work is needed to study shower shape and perform track projection to the calorimeter layers. The final aim of this study is to develop methods for identifying neutral hadrons. For this purpose, machine-learning techniques will be employed.

References

[1] ATHENA Collaboration. ATHENA Detector Proposal - A Totally Hermetic Electron Nucleus Apparatus https://doi.org/10.5281/zenodo.6539707

[2] CORE Collaboration. CORE - a COmpact detectoR for the EIC https://doi.org/10.5281/zenodo.6536630

[3] ECCE Collaboration. ECCE - EIC Comprehensive Chromodynamics Experiment https://doi.org/10.5281/zenodo.6537588

[4] R. Abdul Khalek, et. al. Science Requirements and Detector Concepts for the Electron-Ion Collider: EIC Yellow Report arXiv:2103.05419 [physics.ins-det] https://doi.org/10.48550/arXiv.2103.05419

[5] Giacomini, G and Chen, W and D'Amen, G and Tricoli, A. Fabrication and performance of AC-coupled LGADs JINST 14 P09004 https://doi.org/10.1088/1748-0221/14/09/p09004

[6] Dey, B. and Ratcliff, B. and Va'vra, J. Small FDIRC Designs NIMA, vol 876, p141-144 https://doi.org/10.1016/j.nima.2017.02.044

[7] M.Beddo, et. al. The STAR Barrel Electromagnetic Calorimeter NIMA, vol 499, p725-739 https://doi.org/10.1016/S0168-9002(02)01970-8

[8] DD4hep http://dd4hep.cern.ch/ https://doi.org/10.5281/zenodo.6421687

[9] S.Agostinelli, et. al. Geant4—a simulation toolkit NIMA, vol 506, p250-303 https://doi.org/10.1016/S0168-9002(03)01368-8

CENTRAL INCLUSIVE PRODUCTION OF K^0_S AT THE EXPERIMENT STAR

Michaela Svěráková

1 Motivation and introduction of the theory

Central inclusive production, studied in the presented analysis, falls into the category of diffractive phenomena [**?**]. It is characterised by large rapidity gaps between the protons moving forward after their collision and the produced central system of particles. The production being inclusive means not all produced particles are studied, just the ones relevant for the specific analysis. The process is typically described using Regge theory as an exchange of Regge trajectories. For the energies present, the asymptomatically dominating Regge trajectory is called Pomeron. It is a particle represented in pQGP by pairs of gluons that emulate its known quark numbers. Particles made up of just gluons, that are predicted to exist by QCD are called glueballs.

The goal of this this work was to reconstruct meson K^0_S using its main decay channel $K^0_S \to \pi^+\pi^-$. The STAR detectors Time Projection Chamber, Time of Flight, Beam Beam Counter, and the Roman Pot system were used for this analysis. The ROOT framework was used to get the results in the form of distribution of invariant mass of K^0_S and the K^0_S yield. Results of my work are marked by "This work" and are not results approved by the STAR collaboration.

2 Experimental set-up

The detectors relevant for this analysis are four subdetectors of the STAR experiment. Time Projection Chamber (TPC) and Time of Flight (TOF) and Roman Pot system (RP) were used to reconstruct the tracks of charged particles. Beam Beam Counters (BBC) were used to check the rapidity gaps. The scheme of the different STAR subdetectors from 2017, and of the RP system placement can be seen on Fig. 22.

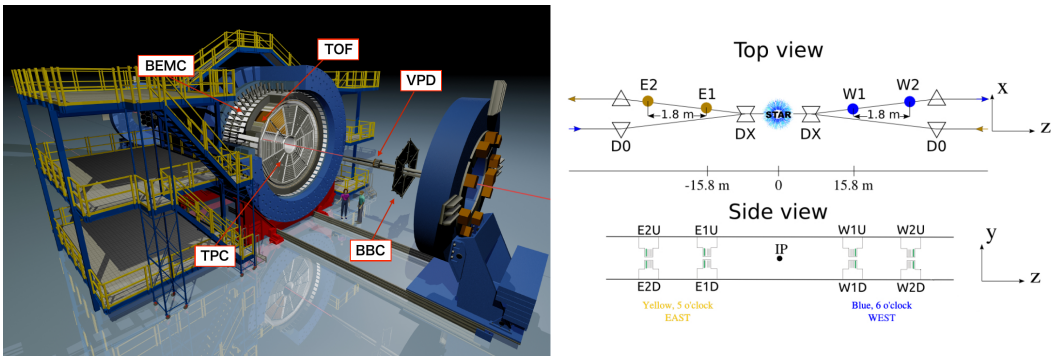

Figure 22: Experimental set-up for this analysis. The central STAR detector with marked subdetectors (left). Taken from Ref. [**?**]. The placement of Roman Pot stations with the respect to central STAR detector (right). Taken from Ref. [**?**].

3 Data and selection of events for the analysis

Data for this analysis are from proton-proton collisions at $\sqrt{s} = 510$ GeV at RHIC collected by experiment STAR in 2017. Selection criteria were applied on the available data to obtain a set of events suitable for further analysis. These criteria are presented below. The gradual decrease of events after each cut can be seen on Fig. 23.

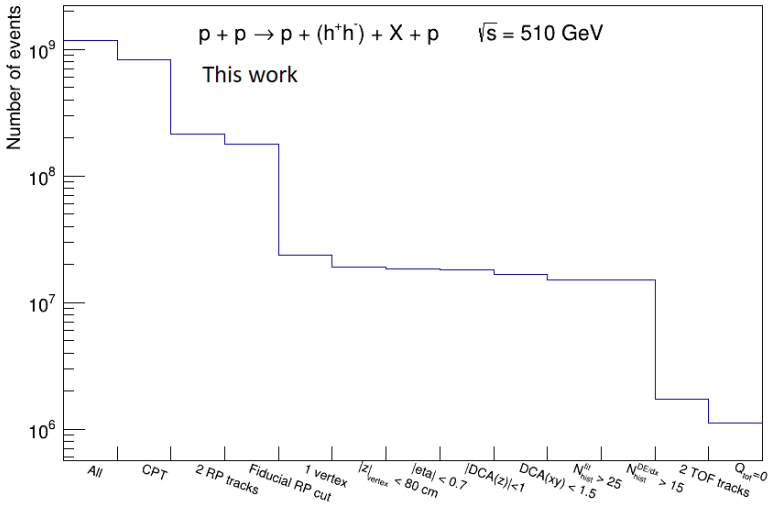

Figure 23: Histogram representing steps of the event selection and gradual decrease of events meeting the criteria. Axis y in logarithmic scale.

Firstly, only events that trigger the Central Production Trigger are accepted. In this analysis 830.167 million events make this cut. Next, as we expect the two collided protons to continue their way forward, only events with exactly two tracks registered in Roman Pots are allowed. Additionally at least three out of the four silicon strip detectors in RP have to be used for the track reconstruction. These tracks in RP need to be in an area of high geometric acceptance to ensure hight efficiency of track reconstruction. This area is called the Fiducial Region and is defined by the following equations, where p_x and p_y are the momenta of protons in axis x and y respectively.

$$\begin{aligned} &(p_x + 0.6)^2 + p_y^2 < 1.25 \text{ GeV}^2 \\ &0.4 \text{ GeV} < |p_y| < 0.8 \text{ GeV} \\ &p_x > -0.27 \text{ GeV} \end{aligned} \tag{4}$$

Another criteria is for the tracks of particles created in the collision to be coming from one vertex. This vertex then needs to be a maximum of 80 cm away from the centre of TPC to ensure high geometric acceptance. Maximal value of charged particles' pseudorapidity is set to be 0.7 to ensure the tracks are in an area with sufficient TOF acceptance.

Following four conditions define the so-called good quality tracks. Minimal number of points recorded in the TPC used in the track reconstruction needs to be equal of greater than 25. Minimal number of points used to calculate the energy loss per unit distance needs to be equal of greater than 15. Maximal distance of closest approach of the tracks to the primary vertex in the z axis needs to be less than 1 cm and in the transverse xy plane less than 1.5 cm.

Condition enforced next is to have exactly two track in TPC with associated hits in TOF per event. These two particles are assumed to be pion in this work. This assumption is supported by previous works on central production on the same data set, where it was found that pions make up 97 % of the decays [**?**]. Possible misidentification of particle pairs can be taken as a systematic uncertainty on the level of statistical uncertainty so it can be neglected within the scope of this work. Last is the condition for the total charge of the tracks to be zero as pion pairs $\pi^+\pi^-$ are searched for.

4 Results - invariant mass of K^0_S and K^0_S yield

After the application of the above presented selection criteria, I had 1.122 million events for further analysis. For these events the invariant mass distribution of the pion pairs was drawn, presented on Fig. 24. The prominent peak corresponds to pion pairs coming from the K^0_S decay. On a region $0{,}4 - 0.6$ GeV/c^2 the data were fitted with a compound function (Gauss + polynomial of second degree) - green on Fig. 24. Obtained invariant mass corresponds to the μ (mean) parameter of the Gauss function and it is: $m_{K^0_S} = 496.4 \pm 0.1$ MeV/c^2. For comparison the invariant mass of this meson currently stated on the Particle Data Group website is $m = 493.677 \pm 0.016$ MeV/c^2 [**?**].

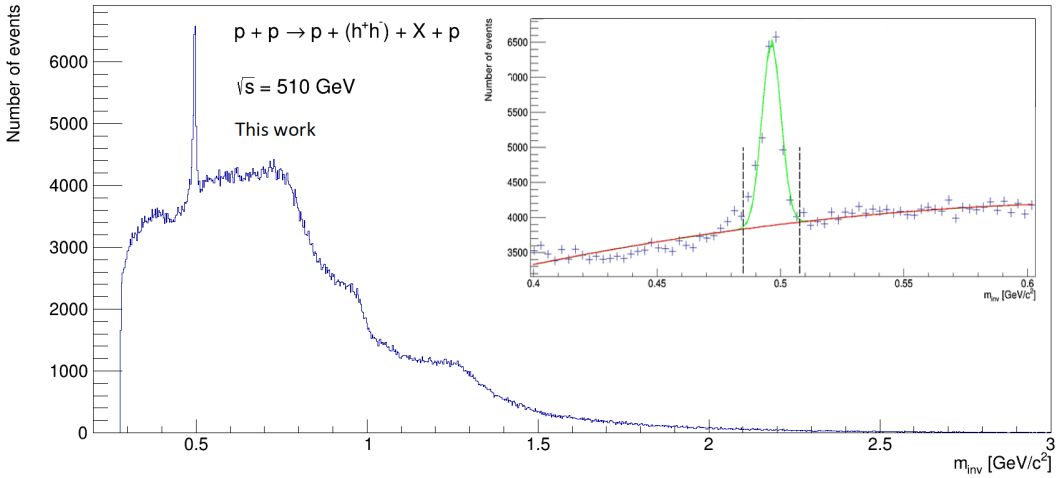

Figure 24: Invariant mass distribution of pion pairs. Inserted image is the same distribution zoomed in on the region around the prominent peak, on which the data were fitted.

As the K^0_S yield was the next wanted result, the subtraction of the so called background events, that are not contributing to the K^0_S peak, was needed. The background events were fitted with a polynomial function of the second degree - red on Fig. 24. Both fitting function (red and green) were integrated on region $\mu \pm 3\sigma$: $(0.4844; 0.5084)$ GeV/c^2 represented on Fig. 24 by the black dashed line. The integration results were subtracted and the K^0_S yield calculated as $75\ 291$ events in which the pion pair $\pi^+\pi^-$ is a result of K^0_S decay.

LINEARITY OF THE UPGRADED ELECTRONICS AT THE PIERRE AUGER OBSERVATORY

Marek Strnad

1 Introduction

The Pierre Auger Observatory is the biggest astroparticle experiment in the world. Its goal is to detect and measure incoming cosmic ray particles. In order to do that in the most data yielding way, the observatory has to undergo several upgrades. One of these upgrades is the AugerPrime upgrade and one of many parts of AugerPrime is the upgrade of control electronics of the Surface detector. These new motherboards, however, need to be properly tested. Both in regards to functionality and durability, with linearity testing being one of the functionality tests.

2 Cosmic Rays

There are two types of cosmic rays, primary and secondary. Primary cosmic rays are a flux of high energy charged particles, coming to Earth from Space. These particles consist mainly of protons ($\approx 89\%$), then alpha particles ($\approx 10\%$) and the rest being heavier nuclei, electrons, positron, antiprotons etc. Those proportions depend mainly on the energy of the incoming radiation. Another property that depends on this energy is the particle flux. This dependence can be seen on Fig. 25. One can see that the flux decreases rapidly with energy, to the point that one of the most energetic particles can be seen in an area of 1 km^2 once per year. Upon interaction of primary cosmic rays with Earth´s atmosphere, a shower of secondary cosmic rays starts to form. Muons, pions, neutrinos, photons and neutrons created this way then bombard the surface of Earth as a result.

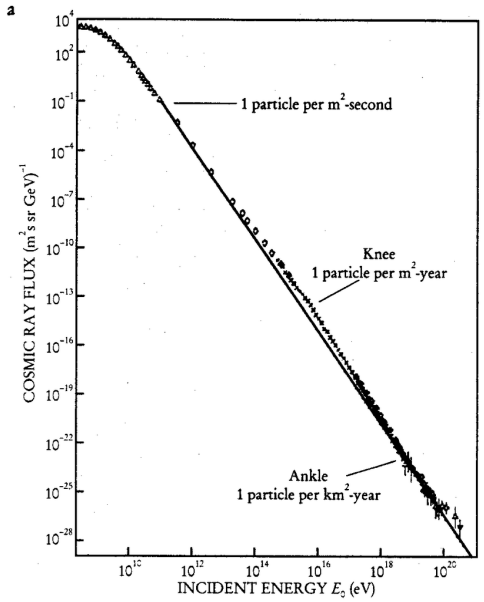

Figure 25: Energy dependence of the incoming cosmic ray flux. [1]

3 Pierre Auger Observatory

In order to properly detect these high-energy cosmic rays, we need to measure them either for a long time or over a large area. This area has to be flat, with low light pollution, with stable weather conditions and ideally be located on the southern hemisphere for it to be able to cover the centre of the Milky Way. The Pierre Auger Observatory was built with these needs in mind and its construction was finished in 2008. It is currently the largest running astroparticle experiment on Earth, spreading over an area of 3000 km^2 in Argentine pampas. It is a hybrid detector, meaning that it uses two independent methods of measurement.

3.1 Surface detector

One of these methods is the Surface detector. It consists of over 1660 Cherenkov water detectors, which are separated 1,5 km from each other in the area of the observatory. When a particle enters the water filled tank, it produces Cherenkov radiation, which is then detected by photomultipliers located inside the tank. Picture of one station can be seen in Fig. 26. Each station comes with solar panels, battery and an anthenna, for it to be able to continuously and independently collect and export data.

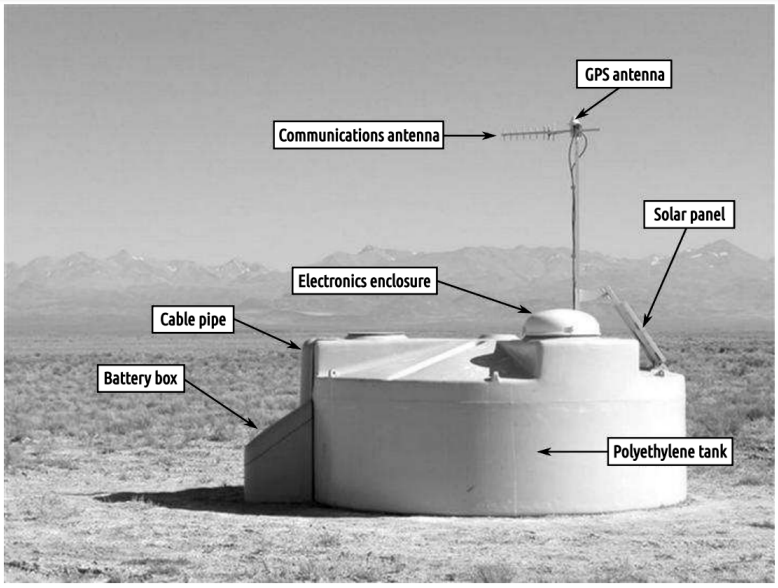

Figure 26: Schematic picture of one station of the Surface detector array. [2]

3.2 Fluorescence detector

The second measurement method is the Fluorescent detector. When a cosmic ray particle interacts with atmospheric nitrogen, it produces UV light via fluorescence. This light can then be detected by 27 optical detectors, located at four locations at the observatory, covering 360 degrees field of view. When this light reaches the detector, it is then focused with segmented mirrors into a camera, which consists of 440 photomultipliers. The schematic of this detector can be seen at Fig. 27.

3.3 AugerPrime Upgrade

There are numerous upgrades being currently done at the observatory. One of them is called the AugerPrime upgrade, with main purpose of which being to make improvements of detectional abilities of the observatory. The Fluorescent detector will be upgraded, so that it can make measurements even during nights with visible moon. The Surface detector on the other hand will get several upgrades. There will be added two scintillators to each station, one underground

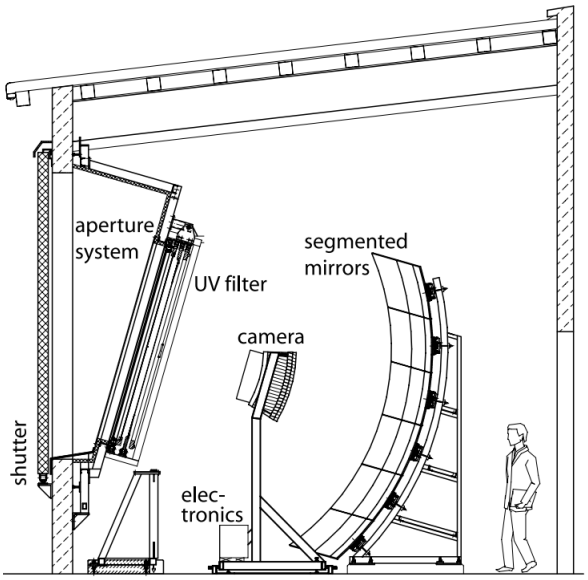

Figure 27: Sideview schematic of a Fluorescence detector station. [2]

and one above the tank. There will also be added a radio anthenna on top and a small photomultiplier inside the water tank. To connect all of these new detectors together, a new motherboard had to be created. This Upgraded Unified Board, or UUB, has more channels, has faster analog to digital conversion and makes it easier to calibrate all the detectors in comparison to the former one. [3].

4 Linearity Measurements

New UUBs need to be properly tested however. Both in regards of their functionality after manufacture and in regards of durability, in order for them to survive demanding weather conditions of the Argentine pampa. One of these functionality tests is the linearity testing. It is done to see whether the analog to digital signal conversion works as prescribed. This testing is done by generating a testing analog signal, consisting of five half sine pulses, converting it with the UUB and comparing the coefficients of regression of fitted peaks of the analog and digital signal. These tests are still ongoing and the properly working UUBs are being sent to Argentine for montage.

References

[1] Perkins, Donald H. Particle astrophysics. Oxford University Press, 2009.

[2] Pierre Auger Collaboration, et al. The Pierre Auger cosmic ray observatory. Nuclear Instruments and Methods in Physics Research Section A: Accelerators, Spectrometers, Detectors and Associated Equipment, 2015, 798: pages 172-213.

[3] Pierre Auger Collaboration "The pierre auger observatory upgrade-preliminary design report." arXiv preprint arXiv:1604.03637, í2016

FEMTOSECOND ELECTROSTATIC ELECTRON GUN DESIGN AND OPTIMIZATION

Zdeněk Vostřel

1 Introduction

With rapid development of lasers in recent years, a possibility of generating precise laser pulses and utilizing them for electron emission from metals arises. Such electrons can subsequently be accelerated by static electric field. This possibly results in production of almost monoenergetic, collimated electron bunches at very high frequencies.

For further use, these bunches must be focused. This work is dedicated to investigating the effect of focusing electrostatic lens on the properties of the produced electron bunch. The studied properties are energetic, space and time profile. A simulation in `Simion` software was performed to test the design.

The proposed electron gun can serve as an accelerator itself or as a preaccelerator and injection mechanism for the laser driven plasma accelerators. Another possibility is to use the monoenergetic bunches as an X-ray source.

2 Photoemission from metals

For an electron to be emitted from a metal, it must obtain enough energy to overcome the potential barier. There are many ways of achieving this, including heating or usage of external electric field. This work proposes photoemission. The principle of photoemission is that electrons gain the necessary energy by absorbing a photon of energy

$$E_\gamma = h\nu, \tag{5}$$

where h is the Planck constant and ν the frequency of the photon. The photoemission consists of three steps:

1. Absorption of photon.
2. Traversing in the material.
3. Leaving the material.

As the energy loss in step 2 is very high, the electron can traverse only few nanometres before losing too much energy. This distance is smaller than the penetrating distance of laser in metals. Thus, only a part of the laser total energy is actually used for the emission [1].

3 Electrostatic focusing lense

The focusing apparatus in the proposed design consists of a single electrostatic *einzel lens*. This lens is composed of three cylindrical, differently charged electrodes. A 3D view from the performed simulation is presented in Figure 28.

The effect of this lens on the beam can be approximated by the *paraxial equation* [2]. Two main aberration effect arise:

1. *Spherical aberration*: the lens effect is dependent on the initial transverse position of the electron.

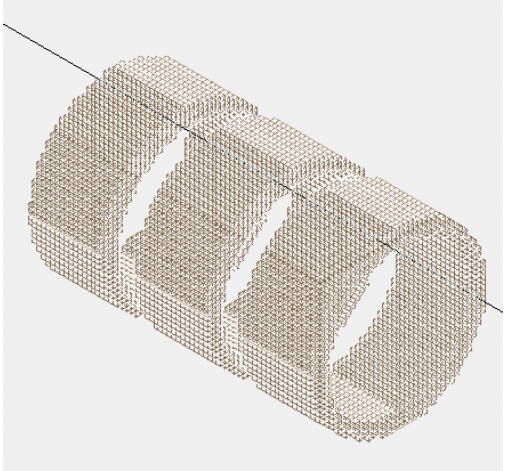

Figure 28: 3D view of the focusing einzel lens.

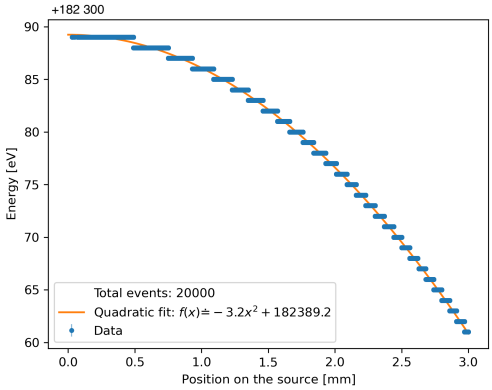

Figure 29: Energy profile of the electrons after traversing the focusing apparatus.

2. *Chromatic aberration:* the lens effect is dependent on the initial energy of the electron.

Both of these effects result in degrading the focal point.

4 Simulation results

In this section, general simulation results are presented.

Initial monoenergetic spectrum of electrons is degraded after passing the focusing apparatus. In Figure 29, see the dependence of energy loss on the initial position of electron on source. Although the energy variance may seem negligible compared to the total energy, it plays an important role in the time profile of the electron bunch.

The time profile is presented in Figure 30. The dependence was fitted by a quadratic function, the fit coefficients are noted in the figure. Due to the design of the lens, only three factors can affect the time profile:

1. Different path lengths the electrons in the centre of the bunch travel compared to the electrons at the edge.
2. Different energies and thus velocities of electrons.
3. Time delays inside the lens.

Effects of the first two are also noted in Figure 30. The difference between these two combined effects is caused by the time delays inside the lens.

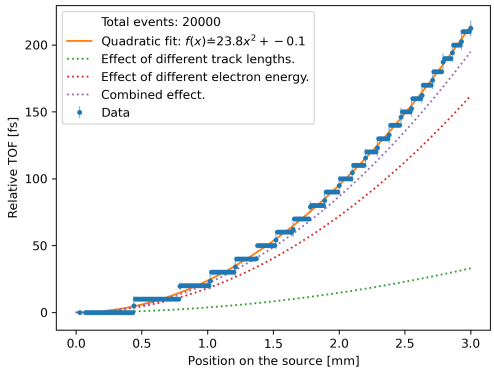

Figure 30: Time of flight (TOF) dependance on the initial position of electrons.

4.1 Key outcomes

Most of the total time delay is thus caused by the different velocities and energies of electrons. To achieve femtosecond bunches, this must be optimized. Lower energy variance can be achieved by decreasing the voltage of the lens or increasing its dimensions. Both, however, lead to the increase in the distance of the focal point.

The observed quadratic dependence in Figure 30 can be utilized to adjust the time profile of the lase pulse initiating the photoemission. Thus the effect of the focusing apparatus on the time delays can be compensated.

The transverse profile of the bunch gives limitations of the emission area and thus the charge present in the focus. This is caused by the focal point distance dependance on the initial electron position. Thus, in the best focal plane, only electrons from inner part of the bunch are present.

5 Conclusion

This work focuses on focusing electron bunch via electrostatic lenses. The aim of the performed simulation is to serve as a ground basis for practical construction of the focusing apparatus.

Three main properties were studied: energy, transverse, and time profile. Initial monoenergetic spectrum is degraded, largely impacting the time of flight of electron. The quadratic dependence of time delay on the initial electron position is observed. Transverse profile gives limitation to the possible emission area due to spherical aberration.

Outcomes of this work are to be used to adjust the time profile of the laser inducing the photoemission.

References

[1] Glenn F. Knoll. Radiation detection and measurement. *John Wiley & Sons*, 2010.

[2] Friedrich Hinterberger. Ion optics with electrostatic lenses. DOI: `https://doi.org/10.5170/CERN-2006-012.27`, 2006.

[3] Guy Hadash, Einat Kermany, Boaz Carmeli, Ofer Lavi, George Kour, and Alon Jacovi. Estimate and replace: A novel approach to integrating deep neural networks with existing applications. *arXiv preprint arXiv:1804.09028*, 2018.

CHARM MESON PRODUCTION IN PROTON-NUCLEUS COLLISIONS IN THE STAR EXPERIMENT

Michal Svoboda

ABSTRACT: Just a moment after the Big Bang a state of matter called the Quark-Gluon Plasma was present in the Universe. We are able to reproduce this state of matter for a fraction of second in heavy-ion collisions on large particle colliders such as LHC or RHIC. Multiple different tools can be used to study QGP. To correctly describe behavior in heavy-ion collisions, effects caused by a simple presence of a nucleus have to be understood. These effects are called cold nuclear matter effects and can be studied in proton+nucleus collisions. Heavy quarks originating from the early stages of collisions are a good probe for the measurements.

1 Introduction

One of the main goals of the large particle colliders, such as Large Hadron Collider (LHC) in Switzerland and Relativistic Heavy Ion Collider in the USA, is to study a state of matter called Quark-Gluon Plasma (QGP). This state of matter was present in the Universe shortly after the Big Bang and is expected to be present in the centres of neutron stars. QGP can be reproduced for a short time in the collisions of heavy ions (lead+lead, gold+gold) at a sufficient energy. Collisions of protons serve as a baseline for the measurements in the collisions of heavy ions. However some effects are also caused by a bare presence of a nucleus in a collision. These are called Cold Nuclear Matter (CNM) effects and to isolate them, nucleus+proton (or nucleus+deuteron) collisions, are studied. It is usually assumed that there is not present any QGP in these collisions. A useful tool for the study of CNM effects is the Nuclear Modification Factor R_{AA} which is defined as

$$R_{AA} = \frac{1}{\langle N_{\text{bin}} \rangle} \frac{\frac{\mathrm{d}N}{\mathrm{d}p_T}|_{AA}}{\frac{\mathrm{d}N}{\mathrm{d}p_T}|_{pp}}, \tag{6}$$

where $\langle N_{\text{bin}} \rangle$ is the mean number of binary collisions of nucleons calculated from the Glauber model, $\frac{\mathrm{d}N}{\mathrm{d}p_T}|_{AA}$, resp. $\frac{\mathrm{d}N}{\mathrm{d}p_T}|_{pp}$ is a yield depending on the transverse momentum p_T in a nucleus+nucleus collision and proton+proton collision, respectively. To compare p+p collisions to asymmetric collisions, the AA yield has to be replaced by pA or dA yield.

2 Cold Nuclear Matter Effects

Heavy quarks (such as charm or beauty) originate in the early stages of a collision and thus can serve as a good probe of the effects of the nuclear matter. There are multiple effects which can influence the production of heavy quarks which are

- **Modification of the Parton Distribution Function** - PDF (depending on a Bjorken x and transferred four-momentum Q^2) describes the probability of finding a parton with momentum fraction x at a scale Q^2. It is expected that the behavior of free partons differs from those bound in a nucleus. Different parton density is responsible for this effect which can be quantified by a shadowing factor R_i^A which is defined as

$$R_i^A(x, Q^2) = \frac{f_i^A(x, Q^2)}{A f_i^{\text{nucleon}}(x, Q^2)} \tag{7}$$

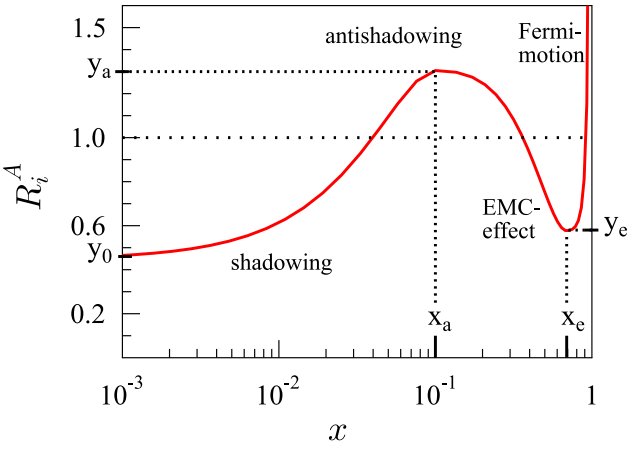

Figure 31: Dependence of the R_i^A on the Bjorken x with different regimes of the PDF modification. Taken from [1]

.

where A is the number of nucleons in the colliding nucleus, f_i^A is the bound nucleon PDF for parton flavour i and f_i^{nucleon} is free nucleon PDF. Values of shadowing factor for different Bjorken x are in the Figure 31.

- **Parton Saturation** - For small values of x the hadron looks denser. At some point of low x arises the saturation and instead of creating new partons, gluons start to recombine (gg→g, gg→q). Saturation can be described in the terms of color glass condensate. One of the important parameters for the description of saturation is the nuclear modification factor depending on the rapidity and CGC based models.
- **Multiple Parton Scattering** - This effect is also called a Cronin effect. It arises in a nucleus before or after the hard scattering or it can happen in the both cases. Partons exchange gluons which leads to the loss of energy (both radiation and collision) and thus the p_{T} spectrum broadens. It is characterized by a transport coefficient of CNM $\hat{q}$.
- **Quarkonia Absorption** - Quarkonium travels through the nucleus after its creation, however it can interact inelastically and thus it is absorbed. Suppression of the production is then observed in the yield. Important parameter is the absorption cross-section. Nuclear absorption effects are negligible at the LHC energy, however at lower energies this might be more significant.

3 D^0 in p+Pb Collisions

This section is based on the article [2] which refers to the measurement of p_{T}-differential production cross sections and nuclear modification factors of different types of D meson in p+Pb collisions measured by ALICE detector in 2016 at $\sqrt{s_{\mathrm{NN}}}$ = 5.02 TeV. Nuclear modification factors of various D mesons are shown in the Fig. 32. The R_{AA} is compatible with unity in the whole range of transverse momentum within two standard deviations. Because of the size of the uncertainties, it is not possible to discuss possible mass dependence originating from the collective expansion.

A comparison of the measured data with various models can be seen in the Fig. 33.In the left panel, four models that include only cold nuclear matter effects are shown. A model from Kang et al. shows different trend and does not describe the data at low p_T. A model based on the Color Glass Condensate describes the data within two standard deviations but the model underestimates the data at low p_T. FONLL calculation which is based on perturbative calculations at next-to-leading order describes the data within uncertainties. A model from Vitev et al. based on a LO pQCD calculations with intristic k_T broadening, nuclear shadowing and quark charms energy loss in CNM also describes the data. In the right panel is a comparison to models which assume creation of QGP in p+Pb collisions. The Duke model includes both collisional and radiative energy losses, whereas the POWLANG takes into account only the collisional processes. Neither of these models describes the data, but both show a similar trend as the data with a peak at low p_T.

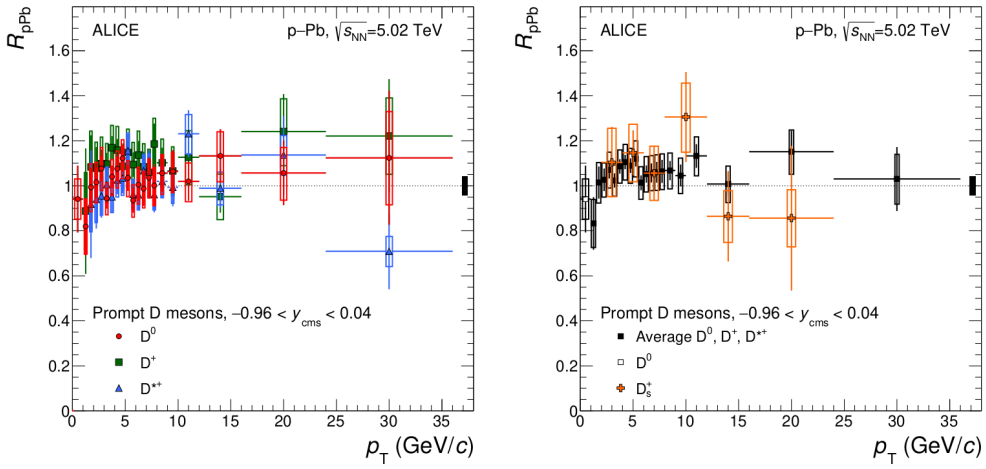

Figure 32: Nuclear modification factor R_{pPb} of prompt D mesons in p+Pb collisions at $\sqrt{s_{\rm NN}}$ = 5.02 TeV measured by ALICE. Left: results for D^0, D^+ and D^{+*}. Right: Average of non strange D mesons in $1 < p_T < 36$ GeV/c, D^0 in $0 < p_T < 1$ GeV/c and strange D meson in $2 < p_T < 24$ GeV/c. Taken from Ref. [2].

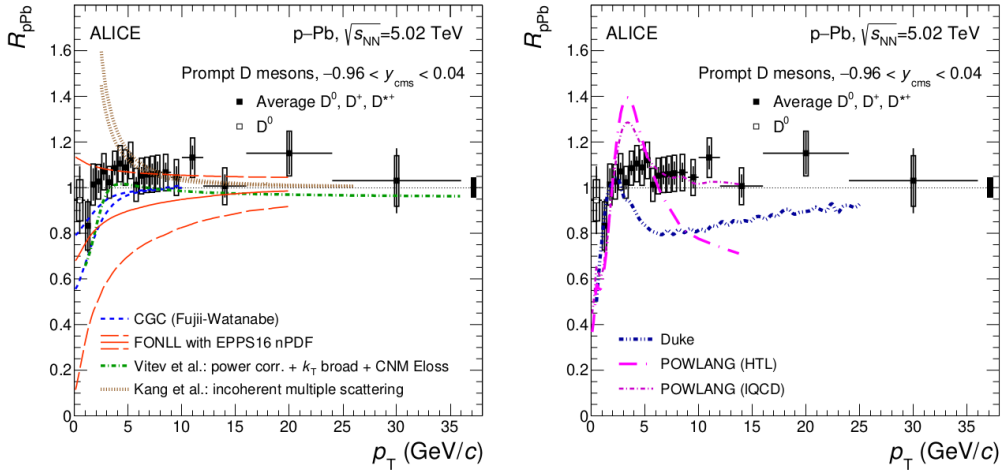

Figure 33: Nuclear modification factor R_{pPb} of prompt D mesons in p+Pb collisions at $\sqrt{s_{\rm NN}}$ = 5.02 TeV measured by ALICE. Left: Comparison with models that include only CNM effects. Right: Comparison with transport models. Taken from Ref. [2].

4 Conclusions

Apart from serving as a probe of hot and dense medium cold Quark-Gluon Plasma, heavy quarks can also be a tool for studying so called cold nuclear matter effects. Particle accelerators LHC and RHIC are able to study these properties. Some of the results have been shown in this short proceedings.

References

[1] Eskola, K. J., Paukkunen, H., & Salgado, C. A. (2009). EPS09 - A new generation of NLO and LO nuclear parton distribution functions. *Journal of High Energy Physics*, *2009*(04), 065-065. https://doi.org/10.1088/1126-6708/2009/04/065

[2] Acharya, S., et al. (2019). Measurement of prompt D^0 , D^+ , D^{+*}, and D_s^+ production in p+Pb collisions at $\sqrt{s_{\rm NN}}$ = 5.02 TeV. *Journal of High Energy Physics*, *2019*(12). https://doi.org/10.1007/JHEP12(2019)092

STUDY OF NON-LINEAR EVOLUTION OF THE HADRON STRUCTURE WITHIN QUANTUM CHROMODYNAMICS

Matěj Vaculčiak

1 Introduction

As the upgrades of experimental facilities such as CERN or BNL promise to reach higher and higher collision energies, probing the hadron structure becomes more precise and the conundrum of its evolution becomes even more tantalizing.

One of the ways to approach this problematics is using the so-called colour dipole model which describes the deep inelastic electron-proton scattering. Within this framework, evolution equations can be obtained such that the previously unobserved yet crucial phenomenon of parton saturation is implemented.

The centrepiece of the presented talk is the Balitsky-Kovchegov evolution equation which contains such an exact mechanism and its results are shown to provide potentially interesting predictions of the newly obtained experimental data. This ultimately brings us a bit closer to understanding what happens inside of hadrons - the smallest composite pieces of matter.

2 Deep inelastic scattering and the colour dipole model

The physical process used to address the hadron structure experimentally is deep inelastic electron proton scattering. In this process the incoming electron emits a virtual photon, which subsequently shatters the proton. The double differential cross section of the process is given by

$$\frac{\mathrm{d}^2\sigma}{\mathrm{d}Q^2\mathrm{d}x} = \frac{4\pi\alpha^2}{Q^4}\left[(1-y)\,\frac{F_2(x,Q^2)}{x} + y^2F_1(x,Q^2)\right], \tag{8}$$

where Q^2 is virtuality, y is inelasticity, x is the Bjorken x, α is the electromagnetic coupling constant and most importantly the functions $F_1(x,Q^2)$ and $F_2(x,Q^2)$ are the so-called structure functions. These observable quantities can be calculated using the colour dipole model in the following way:

$$F_2(x,Q^2) = \frac{Q^2}{4\pi\alpha_{em}}\left(\sigma_L^{\gamma^* p}\left(x,Q^2\right) + \sigma_T^{\gamma^* p}\left(x,Q^2\right)\right),$$
$$F_L(x,Q^2) = \frac{Q^2}{4\pi\alpha_{em}}\sigma_L^{\gamma^* p}\left(x,Q^2\right),$$

where $\sigma_{L,T}^{\gamma^* p}\left(x,Q^2\right)$ are cross sections of the scattering between the virtual photon and the proton. The main idea of the colour dipole model is that the virtual photon splits into a quark-antiquark pair and this colour dipole then interacts with the proton. This two-step process can be recognized in the equations for the photon-proton scattering

$$\sigma_{L,T}^{\gamma^* p}(x,Q^2) = \sum_f \int \mathrm{d}^2\vec{r}\int_0^1 \mathrm{d}z|\psi_{T,L}^{(f)}(\vec{r},Q^2,z)|^2 2\int \mathrm{d}^2\vec{b}N(\vec{r},\vec{b},\tilde{x}_f(x)),$$

where the squared wave function term $|\psi_{T,L}^{(f)}(\vec{r},Q^2,z)|^2$ describes the photon to dipole splitting, while the dipole scattering amplitude $N(\vec{r},\vec{b},\tilde{x}_f(x))$ encodes how the dipole interacts with the proton.

3 Balitsky-Kovchegov equation

To calculate the dipole scattering amplitude from the previous section, the integro-differential Balitsky-Kovchegov (BK) equation can be used. It reads

$$\frac{\partial N(r,b,Y)}{\partial Y} = \int \mathrm{d}\vec{r}_1 K(r,r_1,r_2)\ [N(r_1,b_1,Y) + N(r_2,b_2,Y) - N(r,b,Y) - N(r_1,b_1,Y)N(r_2,b_2,Y)] \quad (9)$$

and describes the evolution of the dipole amplitude with Bjorken x or the rapidity $Y := \ln \frac{x_0}{x}$ equivalently.

The linear terms on the right hand side encode a process where a dipole of size $\vec{r}$ splits into two new dipoles of sizes $\vec{r}_1$ and $\vec{r}_2$. The last non-linear term on the other hand provides a possibility for two dipoles to merge, thus effectively implementing a mechanism of dipole saturation. These dipoles can then be associated with gluons, whose density diverges most violently from all partons.

The BK equation was solved in 1 and 2 dimensional case, meaning that only the dipole size r was taken into account in the 1D case, while in the 2D case also the size of the impact parameter b was used. The results were used to calculate various observable quantities, an example is given in Fig. 34, where the structure function F_2 is shown as calculated with various choices of kernel.

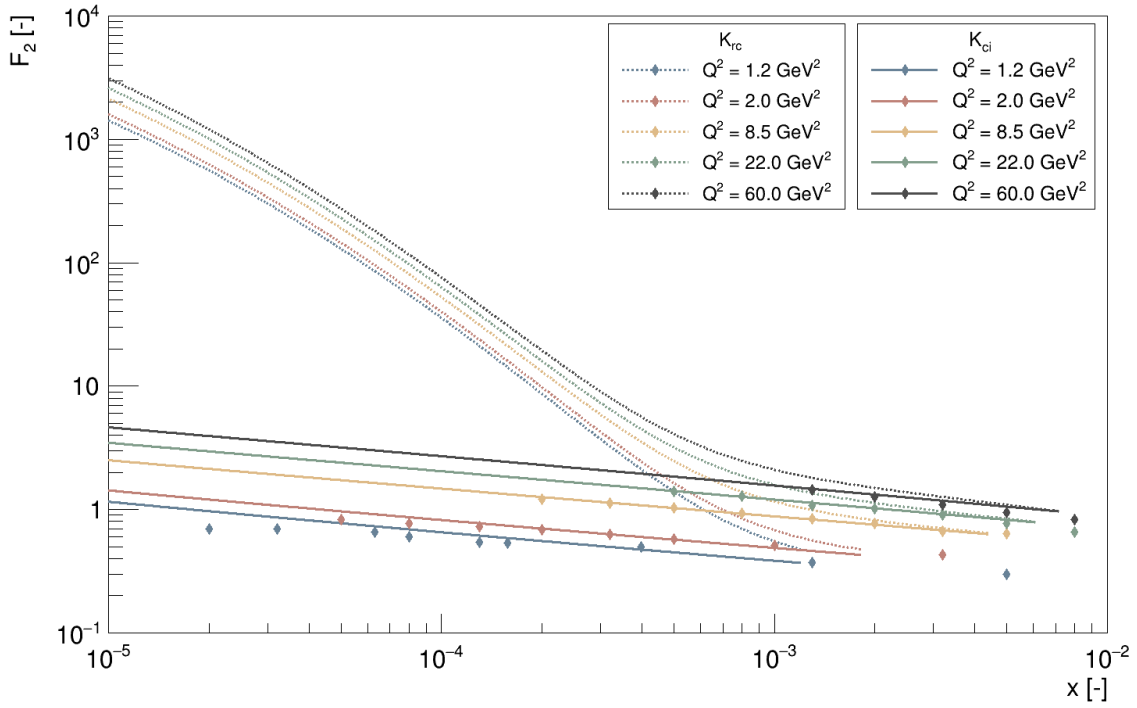

Figure 34: Comparison of F_2 structure functions calculated from 2D BK equation solutions with various kernels (see [1]) with experimental data from HERA [2].

4 Outlook

As already mentioned, only the simplified 1D and 2D versions of the BK equation have been yet calculated, so the natural goal is to be able to obtain a solution in the full dimensional dependence. Furthermore, the BK equation presented in Eq. (9) represents only the leading order approximation and it may be interesting to see the effect of higher order corrections.

References

[1] Matěj Vaculčiak Study of non-linear evolution of the hadron structure within quantum chromodynamics Master's thesis Czech Technical University in Prague

[2] Combined measurement and QCD analysis of the inclusive $e^{\pm}p$ scattering cross sections at HERA 2010 1029-8479 http://dx.doi.org/10.1007/JHEP01(2010)109 10.1007/jhep01(2010)109 1 Journal of High Energy Physics Springer Science and Business Media LLC Aaron, F. D. and Abramowicz, H. and Abt, I. and Adamczyk, L. and Adamus, M. and Al-daya Martin, M. and Alexa, C. and Andreev, V. and Antonelli, S. and et al. 2010 Jan

LASER DRIVEN PLASMA WAVEGUIDES FOR TABLETOP SYNCHROTRONS

Martin Guldan

1 Introduction

Conventional radiofrequency accelerators are growing in size to satisfy the needs of particle physics. This is due to the radiofrequency cavity breakdown that occurs at ∼100 MV/m electric field gradient. If the field is increased beyond this value, critical components of the accelerator may be irreversibly damaged [1]. This is one of the motivations for the development of new acceleration methods. From those, plasma acceleration has already shown some promising results. Its main advantage is the capability to withstand field gradients in the order of 100 GeV. This allows one to accelerate electrons to high energies over short distances [2], [3].

2 Laser wakefield acceleration

One way to obtain such a large gradient is to use an intense femtosecond laser pulse. When shot into an underdense plasma this pulse will create a plasma wave in its wake which is capable of trapping electrons and accelerating them [4]. Such a wave is depicted in figure 35.

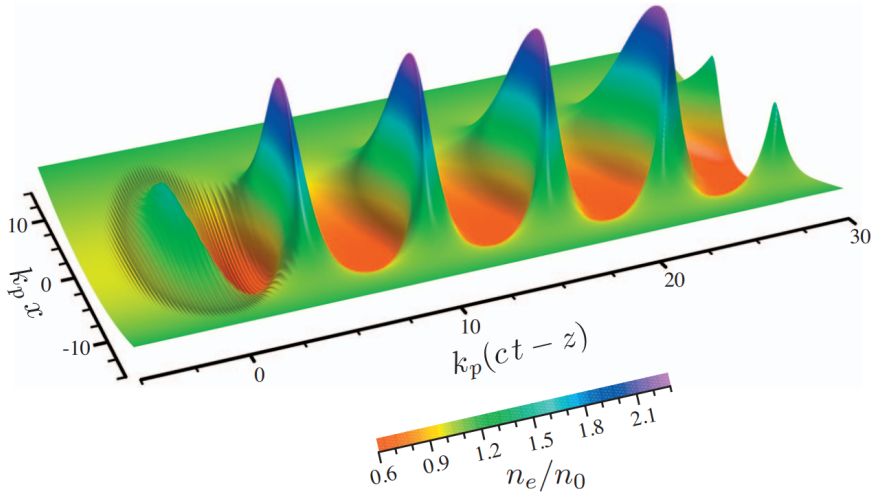

Figure 35: Relative electron density of a plasma wave. Laser pulse is in the left-most bubble going leftward. Adapted from [4].

In order to create this plasma wave, a laser pulse no longer than a few femtoseconds with an intensity upwards of 10^{18} W/cm^2 needs to be used. To achieve this intensity, the laser pulse is focused down to a spot with a diameter on the order of tens of μm. With such a tight focus comes the unwanted effect of shortening of the Reighley length, which is the distance from the focus to a place where intensity is halved due to beam divergence. Focus spot size and Reighley length are related to each other as $\text{Reighley length} \propto (\text{focus diameter})^2$ [5].

To sustain high enough intensity for wakefield acceleration over large distances, beam divergence needs to be compensated. This is done by continuously focusing the beam along its path. A way of guiding the beam is to create a parabolic profile of the density of the plasma through which the laser pulse propagates [6]. The plasma itself then acts as a lens and under the right conditions the spot size does not change. A depiction of a parabolic channel is in figure 36.

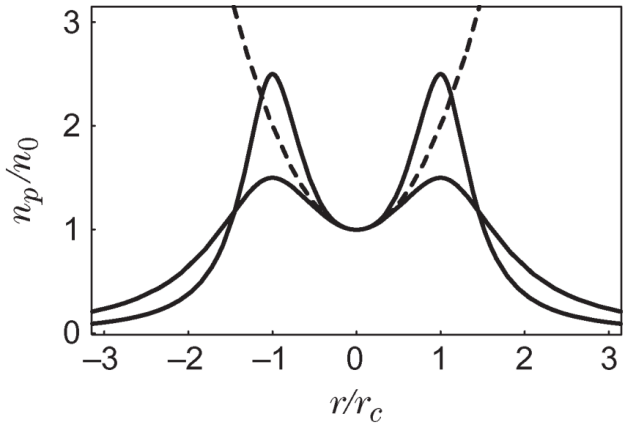

Figure 36: Parabolic electron density profile of a plasma channel on vertical axis plotted against radial distance from channel center. Dashed line - parabola, Solid lines - density profiles with different channel depths. Adapted from [7].

A parabolic profile can be created with an electric discharge through the gas which both ionises and heats the gas. A nanosecond laser pulse can also be shot through the medium to achieve similar results. The hotter part of the plasma expands and the desired density profile is established [8].

3 Curved channel

It turns out that parabolic plasma is even capable of guiding the laser pulse through a curved channel [7]. This gives hope for future multistage acceleration devices such as the one shown in figure 37. So far only simulations have been done. The purpose of my work is to physically demonstrate the feasibility of this technology and send a laser beam through a curved channel.

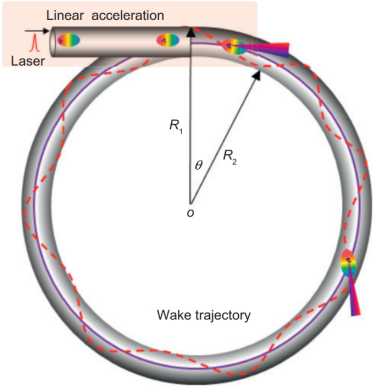

Figure 37: A schematic view of a synchrotron based multistage accelerator. Adapted from [9]

4 Conclusion

Laser wakefield acceleration is a promising technology that could lead to a new era of compact yet powerful particle accelerators. The reduction in size may have a large impact on the availability of fast particles for the purpose of not particle physics, but also medicine, material diagnostics and many others.

References

[1] W. Wuensch. "High-gradient breakdown in normal-conducting RF cavities". Proceedings of EPAC 2002, Paris, France.

[2] Ian Blumenfeld et al. "Energy doubling of 42 GeV electrons in a metre-scale plasma wakefield accelerator". In: *Nature 445.7129 (2007)*, p. 084801.

[3] A.J. Gonsalves et al. "Petawatt laser guiding and electron beam acceleration to 8 GeV in a laser-heated capillary discharge waveguide". In: *Physical review letters 122.8 (2019)*, pages 741–744.

[4] E. Esarey., C.B. Schroeder, W.P. Leemans. "Physics of laser-driven plasma-based electron accelerators". In *Reviews of Modern Physics, Vol. 81, NO. 3, July-September 2009,* pages 1229–1285.

[5] Jinchuan Ju. "Electron acceleration and betatron radiation driven by laser wakefield inside dielectric capillary tubes" (Doctoral thesis). Available from *HAL theses, https://tel.archives-ouvertes.fr/tel-00861267*.

[6] P. Sprangle, E. Esarey, J. Krall, G. Joyce. "Propagation and guiding of intense laser pulses in plasmas". In *Physical Review Letters, Vol. 69, NO. 15*, October 1992.

[7] Albert Reitsma and Dino Jaroszynski. "Propagation of a short intense laser pulse in a curved plasma channel". In *IEEE Transactions on Plasma Science, Vol. 36, NO. 4*, August 2008.

[8] Joost Daniëls. "Measuring and modifying plasma density profiles to confine high power lasers" (Doctoral thesis). Available from *Eindhoven University of Technology, https://research.tue.nl/en/publications/measuring-and-modifying-plasma-density-profiles-to-confine-high-p*.

[9] Min Chen et al. "Tunable synchrotron-like radiation from centimeter scale plasma channels". In *Light: Science & Applications 5.1 (2016)*, e16015-e16015.

DESIGN PATTERNS IN DATA SCIENCE

Henry Day-Hall

1 Introduction

Clean coding practices have long been regarded as essential skills in commercial programming, yet scientific programming harbours little interest. There are some great exceptions, as will be demonstrated by examples given later. However, we must admit to a certain abundance of spaghetti code[1]. and bloated libraries in physics.

The trouble is not that writing good code takes too long, actually, good code saves time, even for relatively small projects[2]. However, setting aside the time to learn about good coding practice on top of the lifetime of topics to be studied in physics itself is a real challenge.

The wealth of freely available material on the subject is mostly orientated towards commercial programming. This isn't irrelevant to science, but our priorities differ, and more targeted text would be helpful. Given space restrictions, the focus here is programming patterns, and their relevance to data science. The reader should gain a basic idea of programming patterns, know a handful of common patterns, and be able to spot those 'in the wild'. This will be of benefit in planning, writing and discussing scientific programs.

1.1 Three preliminaries required for the discussion

Firstly, "Do not Repeat Yourself" (DRY). In programming, repetition, or near repetition, of any amount of code is undesirable. If the repeated concept contains an error, then work to fix the error is multiplied, and it's likely that least one copy is forgotten. If the requirements change and the repeated concept must be altered, this work also is multiplied, and if a copy is forgotten that makes a new error. The whole program takes longer to read, and may become harder to understand[3]. Instead of repetitions, wherever possible, code should be generalised so it can be reused.

The second principle is object-orientated programming. This is a programming philosophy centred on a meeting objectives using objects created from classes. It can be compared to "functional programming" which meets objectives by designing functions[4]. Almost all modern programming is object-orientated.

The third and final concept is that of strong or weak typing. In general terms, a strongly typed language places more importance on an objects type (or class) than a weakly typed one. This can vary along three dimensions.

- *Static v.s. dynamic*; compile time checking only happens in static languages.
- *Manifest v.s. inferred*; the type of objects is only explicitly declared in the code in manifest languages.
- *Nominal v.s. structural*; compatibility of objects is determined by type in a nominal language, but in a structural language it's determined by their properties.

[1] Spaghetti code is a derogatory term describing code that is poorly structured and difficult to understand.

[2] In some areas a bit of judgement is needed, testing code provides very valuable stability, but the average test suite is 5 times the length of the code it tests [**?**, p. 75]. As such, tests are normally worth adding only after code has been established as likely to persist for some time, or significantly buggy, at which point the stability gained by the testing does save time that would be lost hunting problems.

[3] On occasion, the inverse is true, because the technique used to reuse code may become complex. Generally it's still worth reusing rather than repeating, but a judgement call is needed here.

[4] That's not to say that an object orientated program cannot include some functions, they normally do, but the design emphasises the role of objects over functions.

2 Programming patterns and scales in software

Perhaps the most famous book on programming patterns is that of Gamma, Helm, Johnson and Vlissides [**?**]. The authors are referred to as the "Gang of Four" (GoF)[5]. In this book, the GoF define a programming pattern as a "simple and elegant solutions to specific problems in object-oriented software design." [**?**, p. xi]. While our understanding of programming patterns has expanded since the GoF book, this definitions still neatly covers it.

Originally the patterns describes by GoF talked about relationships between classes and functions, referred to as component scale patterns. This includes easily understood ways to avoid code repetition, best allocations of responsibility between classes and good ways to construct complex structures while retaining simple components.

Now we would understand patterns as also existing on larger scales. Application scale patterns cover the overall design of the program. This concerns how information is passed through the program, and concepts like "back-end" and "front-end" live here. The larger scales are not discussed here, because they are rather susceptible to Conway's law; "Any organization that designs a system (defined broadly) will produce a design whose structure is a copy of the organization's communication structure." [**?**]. In physics, the programmer often also has the domain knowledge, so we are tightly bound by Conway's law. It's not inherently a bad thing, but it does give us less agency to chose patterns at the application scale. For further reading on application scale patterns, see [**?**].

3 GoF pattens by intent

The GoF separate patterns into creational, structrual and behavioral. As someone who is not a software architect by training, these categories are somewhat opaque to me; I will use somewhat different categories, that I hope are more intuitive to a physicist.

Objects from a theme. Often we need a set of objects, that share a basic theme. Following the DRY principle, we should not write them all separately, because then the thematic elements would be repeated in each class. Depending on how and when the theme should vary, the pattern used could be one of; State, Template method, Builder or Decorator.

In fastjet [**?**], the Template method pattern is used to facilitate plugins[6]. A fastjet plugin should implement an object representing a new algorithm for jet formation[7]. Different jet formation algorithms may share a distance measure between input particles, a record keeping for partial grouping of particles, and collective properties of grouped particles. The Template method suggests an abstract base class to represent the structure of the algorithm. This abstract base implements the common elements and has and unimplemented methods for the parts that must vary. Each plugin then treats the abstract base class as a 'fill in the blanks' exercise, and overwrites the unimplemented methods. Thus each plugin can be treated as a complete algorithm with a structure that matches the abstract template.

Communicate between variable interfaces. Information and instructions must move through a program, but ideally, one part of a program changing (at run time or in the course of development) shouldn't require if statements or redesigning in other parts. Regardless of whether the variation is inbuilt or expected, a flexible interface is needed, though the exact nature of the flexibility depends both on the elements doing the communication and the kinds of variation that will occur. Patterns that serve this need include Adaptor, Visitor, Mediator, Command and Composite.

Of these, Command is particularly interesting. In this pattern, the communication itself is represented as an object, which could replace a list of arguments. It is passed to a function or class, which retrieves the information it needs. One command could be consumed by many interfaces if it is given enough information to be used by any of the interfaces,

[5]The corresponding patterns are referred to as either Gamma patterns, or GoF patterns

[6]I do not know if the excellent use of patterns in fastjet is a result of the authors knowledge of these patterns, or simply experience in tackling these common challenges. It is observed that many people arrive organically at the best programming patterns.

[7]Jets are a signature found in high energy particle colliders, they are formed by clustering observed particles into exclusive groups.

excess data is simply ignored with no need for dummy arguments. Commands can also be logged to create an ongoing record of the program's activity. Finally, commands can be stored on a stack, and executed asynchronously[8].

Simplifying communication. Like the previous category, this is about communication, however, here the complexity of the communication needs to be controlled. In instances when a direct call from one function to another would require a bloated signature, or many conditionals to chose the appropriate arguments, a less direct approach can simplify communication. These patterns radically reimagine how data can be exchanged, they include Command[9], Bridge, Observer, Chain of responsibility and Facade.

Facade is perhaps most common in scientific programming. Given a complex, flexible system, external users often require only one default process. Rather than requiring the external user to understand the whole system, a facade class is created that is only capable of running this default action, possibly with a limited selection of arguments. This hides the complexity of the system from users that don't require it, they only need to understand the simplified facade.

Facilitating runtime changes. Some requirements change each time the program is run; input types, user selections, or output devices. With weakly typed languages these different modes can be represented by different classes which are used interchangeably. This keeps the classes simple, making each mode the domain of a different object. With the right pattern, a strongly typed language can elegantly achieve the same; patterns include Abstract factory, Factory method, Prototype and Strategy[10].

Strategy is also found in the elegant fastjet plugin system [**?**]. Once a concrete object representing the algorithm has been created by the plugin[11], it is encapsulated by another object, to shield the rest of the program from any differences. The rest of the program treats all encapsulated algorithms the same.

Memory management Memory management might be desired in two senses; firstly, efficiently storing the internal state of an object at a chosen moment is the objective of the Memento pattern. Secondly, the Flyweight pattern is used when many objects would have the same internal state, and we wish to reduce the memory use of the collection.

4 Conclusions

Programming patterns appear in the finest examples of physics code. Well chosen patterns make code more comprehensible, flexible and maintainable. Those with extensive experience will naturally tend towards them, and they are frequently rediscovered by successful programs. Time invested into understanding the theory of programming patterns will be more than repaid by time saved, and pitfalls avoided, when gaining our own experience.

[8] This is the basic principle behind an event driven architecture [**?**, p. 11].

[9] Command is a useful patterns from many perspectives.

[10] These patterns can be applied to weakly typed languages too, but there is normally less need.

[11] As defined by the Template pattern discussed earlier

UPSILON MESON PRODUCTION IN P+P COLLISIONS MEASURED AT STAR

Jakub Češka

1 Introduction

This article presents a brief theoretical overview of the quarkonium production and measurements, which are central to the analysis also introduced. The analysis is aimed at measuring the Υ meson in the p+p collisions at 500 GeV measured by the STAR experiment during Run17. The main focus is the measurement of normalised Υ meson yield in dependence on the normalised charged particle event multiplicity. This allows for the study of the interplay between the soft and hard QCD processes, which are involved in quarkonium production.

2 Motivation

The study of quarkonia is a well-established area of modern high energy physics. Studying their momentum p and transverse momentum p_{T} spectra is useful to further the development of the theoretical models describing their production by comparing the spectra to their predictions. Furthermore, the ratios of their various states serves to understand their production mechanisms and comover interaction. The main focus of the analysis described in this article is the dependence of the normalised quarkonium yield on the normalised charged particle multiplicity. Since the quarkonium yield should be proportional to the number of multi-parton interactions in proton-proton collisions and the multiplicity is related to the energy density in the collision, this dependence helps to understand the multi-parton interaction influence on quarkonium production.

3 Quarkonia

Quarkonia are a bound state of a heavy quark (either c or b) and its corresponding antiquark. Due to the heavy mass of the quarks, they are produced in the very early stages of the collision and thus are used as a probe of the quark gluon plasma (QGP), which is formed later. The study described in this proceeding is focused on Υ mesons, which are bottomonia (bound states of a b quark and $\bar{b}$ antiquark). Quarkonia may exist in multiple quantum states and the Υ meson is the S-wave ($L = 0$) state. There are 3 distinct Υ states, which exist under the open beauty threshold. The masses of those states are shown in Tab. 3 .

state	m [GeV]
Υ(1S)	9.46
Υ(2S)	10.02
Υ(3S)	10.35

Table 3: The masses of the three lightest Υ states. [1]

3.1 Quarkonium production

The quearkonium production consists of two parts: hard and soft. The diquark pair is produced in a hard scattering in a high energy collision, which can be described using a perturbative QCD calculation. The formation of the quarkonium,

the binding of the diquark pair - hadronisation, is a soft process, which cannot be treated perturbatively and models have to be used to describe it. The most common models used are:

- Colour Singlet Model (CSM),
- Colour Octet Model (COM),
- Color Evaporation Model (CEM).

However, there are additional phenomena which play a part in quarkonium production. In proton-proton collisions they are first and foremost multi-parton interactions (MPIs), which describe an event, where in a proton-proton collisions multiple binary parton collisions occur.

3.2 Effects on quarkonia

The produced quarkonia are influenced by several phenomena, when produced in high energy collisions. The most refereed to effect is the dissociation of quarkonia in QGP. This occurs at high temperatures via a mechanism which is analogous to Debeye screening of charges in plasma creation. The heavier quarkonium states, having a lower binding energy, dissociate at a lower medium temperature. This results at a sequential suppression of quarkonium state yields, which has been observed by CMS [2]. Another effect is a co-called feed-down interaction, where a heavier quarkonium state decays in a lighter one. Additional effects include regeneration (which is not significant for Υ mesons at RHIC energies) [3]. Additionally, there are so called Cold Numlear Matter effects (CNM) [4], which include nuclear absorption, comover interactions and nuclear PDF effects.

3.3 Normalised multiplicity dependence

The experimental observable $N_\Upsilon / \langle N_\Upsilon \rangle$ is defined as:

$$N_\Upsilon / \langle N_\Upsilon \rangle = (N_{\text{MB}}/N_{\text{MB}}^{\text{bin}})(N_\Upsilon^{\text{bin}}/N_\Upsilon), \tag{10}$$

where:

- $N_{\text{ch}} / \langle N_{\text{ch}} \rangle \ldots$ self-normalised particle multiplicity;
- $N_\Upsilon \ldots$ total number of events containing Upsilon meson;
- $N_\Upsilon^{\text{bin}} \ldots$ number of Upsilon events in corresponding multiplicity bin;
- $N_{\text{MB}} \ldots$ total number of minimum bias (MB) events;
- $N_{\text{MB}}^{\text{bin}} \ldots$ number of MB events in corresponding $N_{\text{ch}} / \langle N_{\text{ch}} \rangle$ bin.

4 Data analysis

The study described in this article analyses the p+p collisions at 500 GeV recorded by the STAR experiment during Run17. The analysis focuses on BHT2*BBCMB triggered data, which offers $\mathcal{L} \sim 340$ pb^{-1} of integrated luminosity. The analysis consists of several distinct parts, which are:

- event selection;
- track selection;
- event multiplicity ($TofMult$) measurement;
- electron/positron identification;
- Υ candidate reconstruction (in the dielectron channel).

Subsequent parts of the analysis, which among other include signal extraction and its analysis have not been implemented at the moment. The roadblock in the analysis is the fact, that the reconstructed data, which is being analysed, does not contain the information from the Barrel Electromagnetic Calorimeter (BEMC). This leaves only the Time Projection Chamber (TPC) for the identification of electrons; however, at high energies, all of the particles become relativistic and leave a similar signature dE/dx in the TPC. The separation of electrons and hadrons will possible via the BEMC data. The dataset is currently being reconstructed and the author has been involved in the quality assurance work, which had the task of validating the BEMC information presence in the newly reconstructed data.

The algorithm has not produced an Υ meson signal in the dielectron invariant mass spectrum, due to the electron sample not being pure enough and being contaminated by hadrons, mostly pions. However, it has been tested and succeeded in finding a J/ψ signal, which is more pronounced due to the larger c quark cross-section compared to the b quark. The spectra can be seen on Fig. 38.

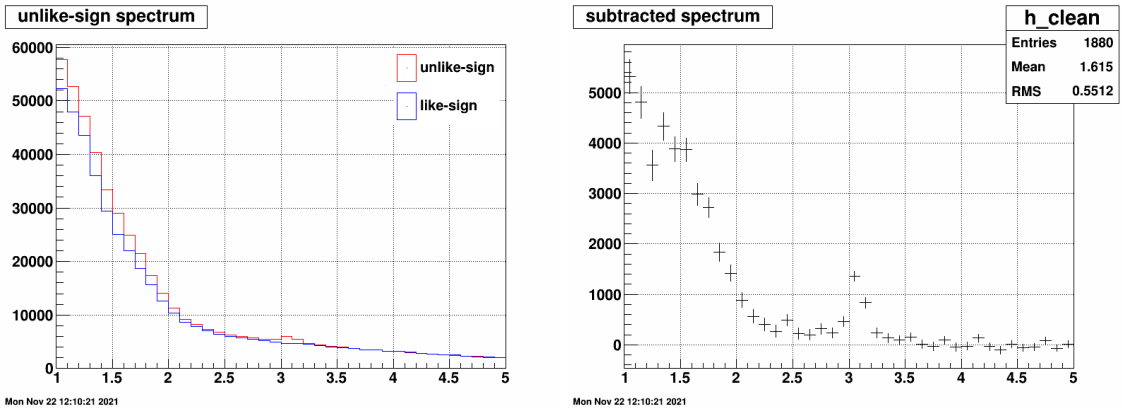

Figure 38: Invariant mass spectrum of: left: unlike-sign (red) and like-sign (blue) reconstructed J/ψ candidate; right: unlike-sign reconstructed J/ψ candidates with like-sign candidates subtracted.

5 Conclusion

The analysis introduced in this article is currently a work in progress. At the moment the algorithm has been validated by producing a J/ψ signal, which shows, that the analysis is being performed correctly. With the ongoing data reconstruction, which should include the BEMC information crucial for the electron/hadron separation, it can be expected that the analysis will soon be able to continue and produce a clean Υ meson signal.

References

[1] R.L. Workman *et al.* [Particle Data Group], **Review of Particle Physics**, To be published in Prog. Theor. Exp. Phys. 2022, **083C01** (2022).

[2] S. Chatrchyan *et al.* [CMS Collaboration], **Observation of Sequential Υ Suppression in PbPb Collisions**, Phys. Rev. Lett. **109** (2012), 222301.

[3] X. Du, M. He, and R. Rapp **Color screening and regeneration of bottomonia in high-energy heavy-ion collisions**, Phys. Rev. C **96** (2017), 054901.

[4] A. Andronic *et al.*, **Heavy-flavour and quarkonium production in the LHC era: from proton–proton to heavy-ion collisions**, Eur. Phys. J. C **76** (2016), 107.

STUDY OF THE MASS COMPOSITION AND HADRONIC INTERACTIONS OF THE ULTRA-HIGH ENERGY COSMIC RAYS USING DATA OF THE PIERRE AUGER OBSERVATORY

Tereza Potúčková

1 Cosmic rays

1.1 History

In 1910 to test the theory that atmospheric ionisation comes from the radioactive materials in the Earth's crust, Theodor Wulf measured ionisation at the top of the Eiffel Tower. There he discovered that the ionisation didn't decrease with the altitude as much as it was supposed to. To investigate this, Victor Hess made a series of balloon flights. During these flights it was measured that at certain altitudes the ionisation started to increase. This led to the discovery of cosmic rays.

1.2 Properties

1.2.1 Mass composition

Cosmic rays are charged particles coming from outer space. Primary particles, which are the ones entering the atmosphere can be protons, alpha particles, heavier nuclei up to uranium or electrons. Which primary will be dominant evolves with energy. When they enter the atmosphere they interact with it, leading to production of secondary cosmic rays in cascades called air showers. These can be detected and used to determine the primary particle that caused the shower and its trajectory.

1.2.2 Energy spectrum

Cosmic rays come into the atmosphere in a wide range of energies, as can be seen on Figure 39. This figure also shows the dependence of number of particles arriving on the energy of the primary particle. Two important points can be seen on the graph called the knee and the ankle. Here the dependence changes. This is related to the origins and means of acceleration of cosmic rays.

2 The Pierre Auger Observatory

The Pierre Auger Observatory is the largest cosmic ray experiment, designed to detect and study them. It is located in Argentina, spreading on over 3000 km^2. The reason for such a large area is the fact that it studies cosmic rays of energies above 10^{17} eV, frequency of arrival of such particle being estimated at about 1 per km^2 per century. It is a hybrid observatory, meaning it combines two types of detection methods.

2.1 Surface detector

The surface detectors are tanks filled with 12000 liters of pure deionised water organized in an array. The tanks contain a photomultipliers to collect the Cherenkov radiation emitted when particles travel through the water at speeds higher

than that of light in water. The amount of light collected is then used to determine the energy of the primary particle. These detectors can also be used to reconstruct the trajectory of the primary particle. A large number of particles is produced during one shower, so they can be detected in more than one tank with slightly different times of detection. For this purpose each detector has a GPS device providing necessary information. A schematic view of a surface detector can be seen on Figure 40.

2.2 Fluorescence detector

The second method of detection uses fluorescence light. Fluorescence telescopes used to detect this light are placed at four sites in groups of six, each with a field of view of $30° \times 30°$. The as a result of interaction with the charged particles produced in the shower nitrogen molecules are excited and subsequently emit light of wavelengths in the UV part of the spectrum that enters the detector where it is focused into its camera. These detectors are used to measure the depth of shower maximum, which is a mass sensitive value and can also be used to reconstruct the trajectory of the primary particle in case one shower is detected by multiple telescopes. A schematic view of a fluorescence telescope can be seen on Figure 41.

3 Figures

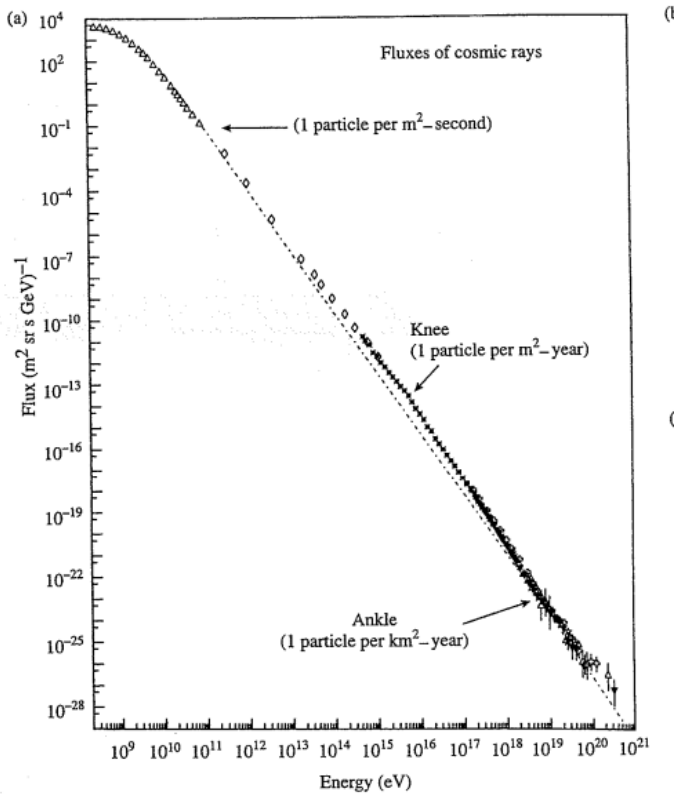

Figure 39: Energy spectrum of primary cosmic rays. [1]

References

[1] Donald Perkins: Particle Astrophysics: Second Edition *Oxford University Press, 2009.*

[2] The Pierre Auger Collaboration: The Pierre Auger Cosmic Ray Observatory. *https://arxiv.org/pdf/1502.01323.pdf*

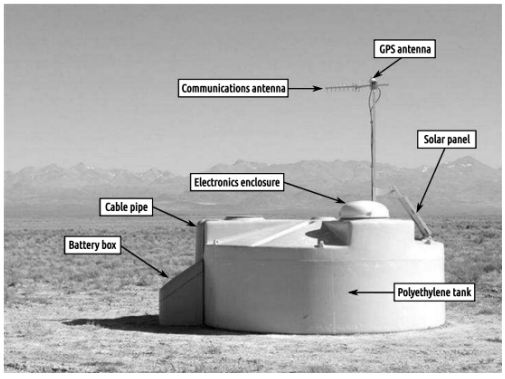

Figure 40: A schematic view of a surface detector. [2]

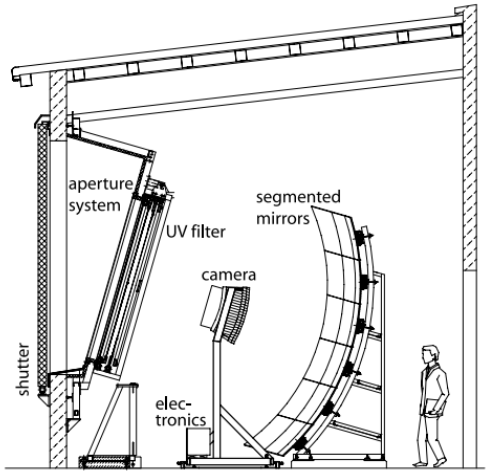

Figure 41: A schematic view of a fluorescence detector. [2]

WEJČF 2022

ELECTRON PRODUCTION FROM THE OPEN-HEAVY FLAVOR DECAY IN RELATIVISTIC HEAVY-ION COLLISION AT STAR

Ayanabha Das, FjFi-CVUT

1 Introduction

Lattice QCD predicted quark-gluon plasma formation in ultrarelativistic heavy ion collision. From the QCD phase diagram, a new form of matter with de-confined quarks and gluons exists at high temperatures and/or high baryon density regions. The experiments such as STAR (RHIC-BNL) and ALICE (LHC-CERN) investigate the evidence of strongly coupled hot and dense matter at different energies. One of the central purposes of these experiments is to understand the QGP through quantitative comparisons between theoretical calculations and experimental measurements. Heavy flavor quarks are a unique probe for this task. Due to their large masses, they are dominantly produced in the initial hard scatterings, where the production rate can be well calculated by perturbative-QCD (pQCD). The measurements of non-photonic electrons (NPE), mainly produced by semileptonic decays of D and B mesons, provide information on heavy quarks production and the properties of nuclear matter created in heavy ion collisions.

The STAR collaboration has dedicated measurements on charm mesons and baryons via hadronic decay channels at Au+Au 200 GeV utilizing Heavy Flavor Tracker (HFT). Directly constructing heavy flavor hadrons becomes quite challenging when going to low energies. The charm production cross section decreases faster with the decrease of collision energy, $\sqrt{S_{NN}}$, than that of the light flavor hadrons. It is challenging to suppress combinatorial background purely relying on the TPC tracking if directly constructing heavy flavor hadrons through typical hadronic decay channels. Hence, the semileptonic decay channel is a better solution to access the heavy flavor properties in the hot medium at RHIC low energy.

Here, we report on the steps towards the measurement of the production yield of heavy flavor electrons (HFE) in Au+Au collisions (0 - 60% centrality) at $\sqrt{S_{NN}} = 54.4$ GeV at the STAR Experiment. The current primary objective of this study consists of including recently available information from the Barrel Electromagnetic Calorimeter (BEMC) subdetector to improve the electron identification in the referred dataset. Two variables are of significant meaning in characterising the QGP properties and its evolution: the elliptic flow coefficient (v_2) and the nuclear modification factors R_{AA} and R_{CP}. Both of these parameters quantify the QGP effects on the transverse momentum spectra of the produced particles. Here, we focus on R_{AA} and R_{CP}, as it is to be obtained from this study shortly.

2 The STAR Experiment

The Relativistic Heavy-Ion Collider (RHIC) is a high-energy particle collider located in Upton, New York. RHIC has the capability of colliding different ion species at different beam energies. The Solenoidal Tracker At RHIC (STAR) is a multipurpose detector with full azimuth coverage dedicated to studying ultra-relativistic heavy-ion and polarized proton-proton collisions. It excels in charged-particle tracking in events with high track multiplicities and particle identification while also featuring a full azimuth electromagnetic calorimeter and a muon detector. Currently, in 2022, STAR is the only detector system running at RHIC. This section 2 describes the subsystems used in our study.

2.1 Vertex-Position Detector (VPD)

The Vertex Position Detector (VPD) consists of two assemblies of nineteen detectors positioned 5.7 m away from the interaction region at the east and west sides of the STAR Experiment. Each side contributes with a maximum covering the pseudorapidity range of $4.24 < \eta < 5.1$. The primary purpose of the VPD is to measure photons from a π^0 decays in the forward direction. Thus, it accurately measures the time of collision and the position of primary vertex with the resolution of $\sim$1 cm and $\sim$2.5 cm for Au+Au and p+p collisions, respectively.

2.2 Time Projection Chamber (TPC)

The Time Projection Chamber (TPC) is the central detector for particle identification (PID) at STAR, covering full azimuth ($\phi < 2\pi$) and a pseudorapidity range of $|\eta < 1|$. It is employed to measure charged particle momentum and ionization energy loss ($-dE/dx$) and to reconstruct the primary vertex. The TPC can provide excellent tracking of particles down to low p_T with the large multiplicities at top RHIC energies.

For TPC particle identification, we base ourselves on a parameter derived from the particle energy loss. This parameter, $n\sigma_x$, relates the measured and expected energy loss in the TPC gas for a given particle species (x) according to equation (1), where $\sigma_{dE/dx}$ is the dE/dx resolution of the TPC. The cuts are applied to identify the electrons and reduce hadron contamination (mainly pions).

$$n\sigma_x = \frac{1}{\sigma_{dE/dx}} ln \frac{\langle dE/dx \rangle_{measured,x}}{\langle dE/dx \rangle_x} \tag{1}$$

2.3 Time Of Flight (TOF)

The main purpose of the Time-Of-Flight (TOF) detector is to extend the PID capabilities of STAR into higher momenta via the measurements of the time of flight (t) of charged particles from its point of origin (or vertex) to the TOF detector, thus measuring its velocity (v). It covers the whole azimuthal angle ($\phi < 2\pi$) and a pseudorapidity range of $|\eta < 1|$. TOF distinguishes between charged particles by estimating the stop time of the incoming particle with a subsequent subtraction of its start time (provided by the VPD). The fraction of the speed of the light in vacuum β is calculated as:

$$\beta = \frac{L}{ct} \tag{2}$$

where, L is the path-length from the primary vertex (PV). For electron identification using TOF, we apply cuts on the particle velocity. Since electrons are expected to have velocity close to the speed of light, their β parameter value (c/v) lies close to unity. By applying the cut $|1/\beta - 1| < 0.025$, we can distinguish electrons from hadrons until the point at which all the particles have a velocity relative to c.

2.4 Barrel Electromagnetic Calorimeter (BEMC)

The STAR BEMC, as a conventional electromagnetic calorimeter, is built to absorb electrons and photons at high energies (E > 1.2 GeV) in the bulk of the lead-scintillator modules. The BEMC covers the complete azimuthal angle and pseudorapidity range of $|\eta| < 1$, matching TPC acceptance. One can distinguish between the produced particles from the percentage of the deposited energy of the electromagnetic shower. Electrons, for instance, deposit almost all their energy on the calorimeter and are therefore easily detected.

An important step when dealing with BEMC information is that cuts are a sanity check to investigate whether some performance problems were present during the runs. For particle identification using BEMC, cuts are applied on the energy-to-momentum ratio E/p (alternatively on p/E). Electrons are expected to have an E/p ratio $\approx$1 since they essentially deposit all their energy inside BEMC. For this reason, we apply a cut at an E/p interval which includes 1. The $e^{\pm}$ identification cuts are summarized in the table in the section.

3 Overview of the analysis

All electrons identified in one specific event are named inclusive electrons, and they are classified in two general categories: photonic electrons (PE) and non-photonic electrons (NPE). The usual technique employed by the STAR Collaboration is to reconstruct NPE constitutes obtaining the corrected yield of photonic electrons and subtracting it from the inclusive electron sample. The PE yield correction is performed based on the simulation of the STAR subdetectors. These simulations constitute future steps in our analysis. Besides the corrected yield of PE, one also needs to consider the purity of the inclusive electron sample (purity) due to p_T-dependent hadron contamination to obtain the NPE. We are currently working on the purity estimation.

The primary sources for the background electrons are photon conversion and pseudo-scalar meson (mainly from π^0 and η) Dalitz decay, so the heavy-flavor electrons (e_{HF}) are also called "Non-Photonic electrons" (e_{NPE}), and the background is called as "Photonic electrons" (e_{PE}). To extract heavy-flavor electrons, one needs to identify the inclusive electrons and subtract the background electrons. In summary, the NPE yield is obtained using the following equation:

$$N_{NPE} = \frac{N_{incl}.\epsilon_{purity} - N_{PE;corrected}}{\epsilon_{total}} \tag{3}$$

In Equation (3), N_{NPE}, N_{incl} and $N_{PE;corrected}$ represent the non-photonic electron yield, the inclusive electron yield and the corrected photonic electron yield, respectively. Here, $N_{PE;corrected}$ is given by $N_{PE;corrected} = N_{PE}/\epsilon_{PE}$, where N_{PE} is the uncorrected photonic electron yield and ϵ_{PE} the efficiency of PE reconstruction, which will be obtained from simulations. Also in equation (3), ϵ_{tot} is the parameter, representing the overall electron efficiency. Based on the outputs of the previous calculation, one can obtain the nuclear modification factors R_{AA} and/or R_{CP} to investigate the energy loss of our hard probes in the medium. The energy loss of these hard probes will be used to characterize the QGP in our study.

3.1 Dataset and event selection

This analysis is based on the minimum bias triggered data collected in RHIC run year 2017. Considering overall statistics of charged particle multiplicities (N_{ch}) between data and Glauber model, we choose to use only one centrality bin, 0-60%. The details of dataset used in the analysis are summarized below:

- Collision type: Au+Au
- Center-Of-Mass (COM) energy: $\sqrt{S_{NN}} = 54.4$ GeV
- Production: P18ic
- Library: SL20c
- Triggers: 580001, 580021
- Run number (min - max): 18153035 - 18172014 (Bad runs are excluded)

A series of event level cuts on the primary vertex position are applied in order to reject bad events. The origin of the frame is defined at the center of the STAR detector and the Z-direction is along the beam direction. The event cuts are as follows:

- $|V_r| = |\sqrt{V_x^2 + V_y^2}| < 2$ cm. Require the collisions inside the beam pipe.
- $|V_z| < 35$ cm. Require that collisions happen inside the TPC, with a uniform acceptance and a low background related to photon conversions in the detector material.
- $|V_{z,VPD} - V_z| < 3$ cm. This cut is for suppression for the pile-up events.
- $|V_x, V_y, V_z| > 10^{-5}$ cm. Require the events have valid vertex information.

Table 1: Track quality cuts

Observables	**Cut values**
p_T	> 0.2 GeV/c. Make sure tracks can pass through the TPC
$\|\eta\|$	< 0.8. Guarantees uniform track acceptance
$\|gDCA\|$	< 1.5 cm. DCA to the priamry vertex, which is to reduce tracks coming from secondary vertex
nHitsFit	> 20. Number of TPC hit points used in the track fitting, which shall be greater than 20 for a good momentum resolution
nHitsDeDx	> 15. Number of TPC hits used to measure the particle ionization energy loss, which must be of at least 15 to improve the dE/dx resolution
nHitsFit2Poss $\rightarrow$ nHitsFit/nHitsMax	> 0.52. Ratio of used and maximum possible number of TPC hit points, which is to avoid one track splitting into two tracks
Primary track	Require tracks coming from primary vertex, which is to suppress secondary vertex tracks and ensure better momentum resolution

3.2 Electron selection and purity study

3.2.1 Track selection

The lifetime of heavy flavor hadrons is very short compared to the TPC track pointing resolution, so heavy-flavor electrons can be regarded as coming from the primary vertex. We set cut on the global track's Distance to the Closet Approach (DCA) to the primary vertex and require tracks to be primary tracks. Track quality cuts not only ensure better momentum resolution but also help to reduce photon conversion electrons. It is one of the primary background sources in this analysis because the start position of photon conversion electrons is usually far away from the primary vertex. Table 1 lists the track cuts for the inclusive electrons.

3.2.2 Inclusive electron identification

After applying the cuts on event and track levels, respectively, the identification of inclusive electrons is then accomplished with the information from TOF, BEMC and TPC. Track and electron identification cuts are applied differently in the case of inclusive (tagged) and partner electrons: partner electron cuts are less strict to improve reconstruction efficiency. As described in the section 2.2, 2.3, 2.4; detailed tagged electron PID cuts for different detectors are represented below:

1. $p_T \leq$ 1.25 GeV: TPC
   - if p > 0.8 $\rightarrow$ 0 < $n\sigma_e$ < 2
   - if p $\leq$ 0.8 $\rightarrow$ (3.5 $\times$ p - 2.8) < $n\sigma_e$ < 2
2. p_T > 1.25 GeV: only TOF and BEMC
   - $|\frac{1}{\beta} - 1|$ < 0.025
   - 0.6 $\leq$ E/p < 1.5
   - if p > 0.8 $\rightarrow$ 0 < $n\sigma_e$ < 2
   - if p $\leq$ 0.8 $\rightarrow$ (3.5 $\times$ p - 2.8) < $n\sigma_e$ < 2

We need to select the partner electron candidates for photonic electron identification, which are used in a tag-and-probe method to study the efficiency of the detectors. We rather have better efficiency and "worse" purity for the PE reconstruction. The partner electron is selected with loose PID cut: $|n\sigma_e|$ < 3.0. If the invariant mass of reconstructed di-electron pair is within $|M_{e^+e^-}|$ < 0.1 GeV/c^2, then the partner electron would be selected as electron samples.

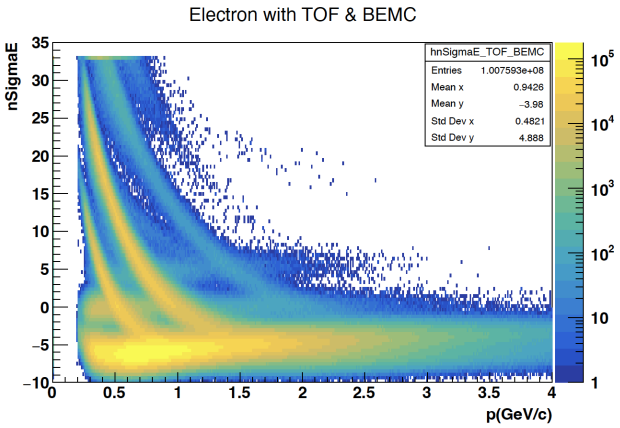

Figure 1: $n\sigma$ vs p (GeV/c) histogram for different particle species after TOF and BEMC cut

3.2.3 Purity estimation - inclusive electrons

One important thing in this analysis is to estimate the purity of inclusive electrons. As it is shown in Fig. 1, there are some momentum regions where electron dE/dx band crosses over with other hadrons. In these momentum regions, electron purity will drop very quickly. To ensure the systematic uncertainty is under control, these regions will be excluded and only the p_T range with high electron purity will be used in later on analysis.

We estimate the electron purity by fitting $n\sigma_e$ distribution to determine electrons relative yield within PID cut range. We project $n\sigma_e$ in fine momentum bins (Fig. 1), so that $n\sigma_e$ distributions of hadrons are close to Gaussian distribution. The default method for the purity fitting is using Multi-Gaussian fit. Firstly we fit $n\sigma_e$ distribution of different particle samples with the normalized Gaussian function and extract σ and mean value. Then fitting the projected Fig. 1 utilizing Multi-Gaussian function with fixed width and mean value. The total fitting function is shown in Equation (4):

$$\begin{aligned} f^{total} = C_e.Gaus(\mu_e, \sigma_e) + C_\pi.Gaus(\mu_\pi, \sigma_\pi) + C_K.Gaus(\mu_K, \sigma_K) \\ + C_{merged\pi}.Gaus(\mu_{merged\pi}, \sigma_{merged\pi}) + C_p.Gaus(\mu_p, \sigma_p) \end{aligned} \tag{4}$$

Physically, the particles yield (proportional to constant parameter in the fitting C_i, i is the particle species) are expected to be a continuous distribution if drawing as a function of momentum. Next, the electron purity is calculated as the integral yield ratio between electron and total fitting function within PID cut (Constant parameters are gotten from Multi-Gaussian fitting).

$$purity = \frac{\int_{(n\sigma cut)} f^e}{\int_{(n\sigma cut)} f^{total}} \tag{5}$$

where, $f^e = C_e.Gaus(\mu_e, \sigma_e)$. Above procedures will give default electron purity for later on calculation.

4 Results & Discussions

To measure the purity of the inclusive electron sample, we base ourselves in the output of the TPC $n\sigma_e$ vs. p histogram after TOF and BEMC cuts have been applied (Fig. 1). By doing a 1D projection histogram of $n\sigma_e$ in different p-bins, we obtain multiple histograms corresponding to the electron distributions along with the hadron contamination sources. The resulting projections are described as a sum of gaussians corresponding to different particles. In this analysis we

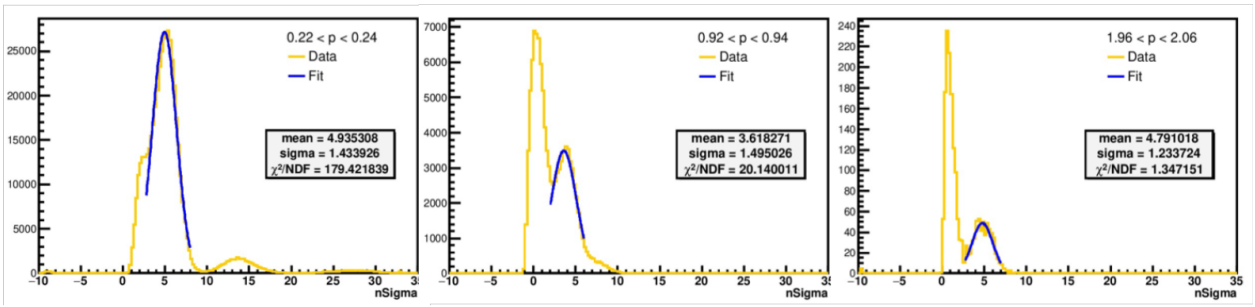

Figure 2: $n\sigma$ projections and fittings for merged π before electron identification cuts at low, intermediate and high p.

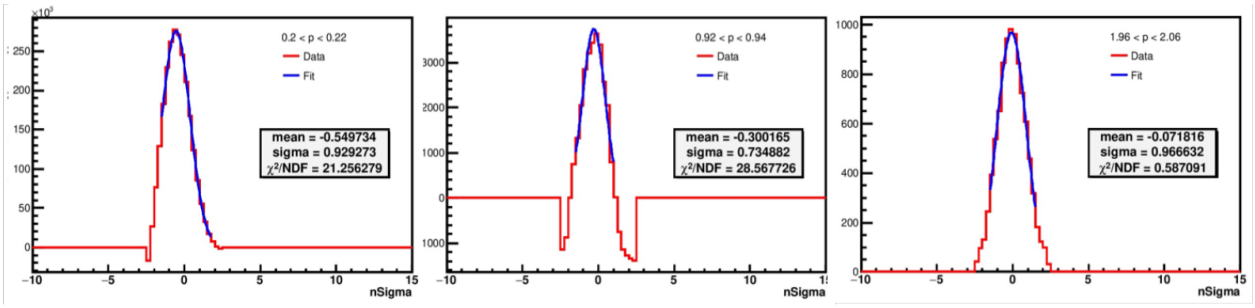

Figure 3: $n\sigma$ projections and fittings for PE before electron identification cuts at low, intermediate and high p.

consider the contamination from pions, merged pions, kaons and protons. Other possible contamination sources are not included here, since they lie far from electrons in $n\sigma$ values.

With the purpose of finding the parameters to the total fits in different p-bins, we apply strict cuts in $n\sigma_K$, $n\sigma_p$, $n\sigma_{merged\pi}$, $n\sigma_{PE}$ distributions before the electron identification cuts are introduced. By extracting the mean and the sigma of the pure sample distributions of protons, kaons, merged pions and photonic electrons, we can provide constraints to the total Multi- Gaussian fit. The description of the sum becomes then more accurate, mainly in the region where overlapping of $n\sigma$ distributions happen. Detailed cuts for particle samples are listed below:

- p: $|M^2 - 0.879| < 0.02\ GeV^2/c^4$, $|n\sigma_p| < 4$
- K: $|M^2 - 0.243| < 0.005\ GeV^2/c^4$, $|n\sigma_K| < 4$
- π: $|M^2 - 0.019| < 0.003\ GeV^2/c^4$, $|n\sigma_\pi| < 4$
- Merged pion: $|M^2 - 0.019| < 0.003\ GeV^2/c^4$, $|n\sigma_{Merged\pi}| > 5$

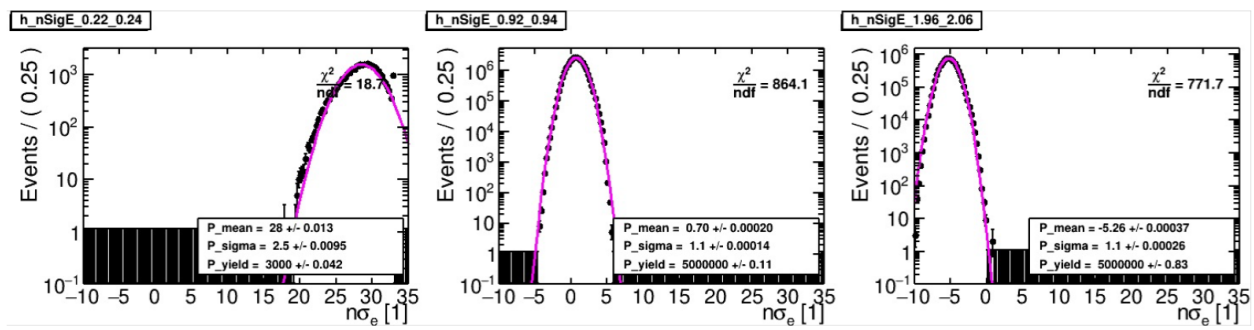

Figure 4: $n\sigma$ projections and fittings for protons before electron identification cuts at low, intermediate and high p.

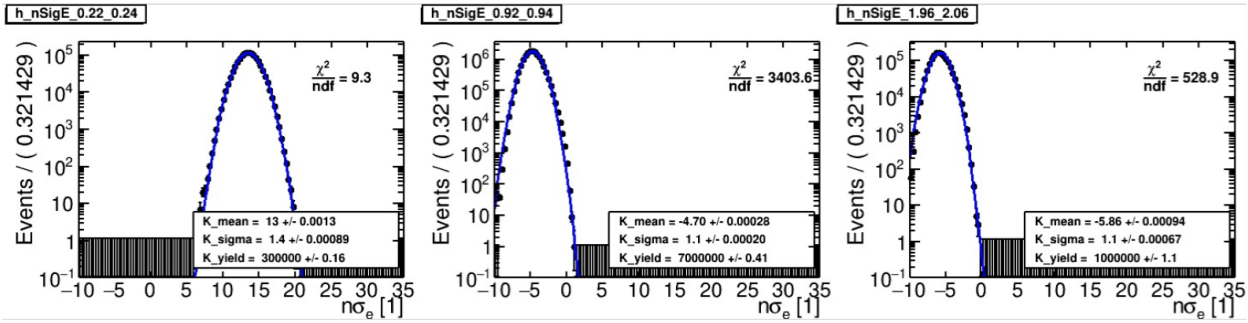

Figure 5: $n\sigma$ projections and fittings for kaons before electron identification cuts at low, intermediate and high p.

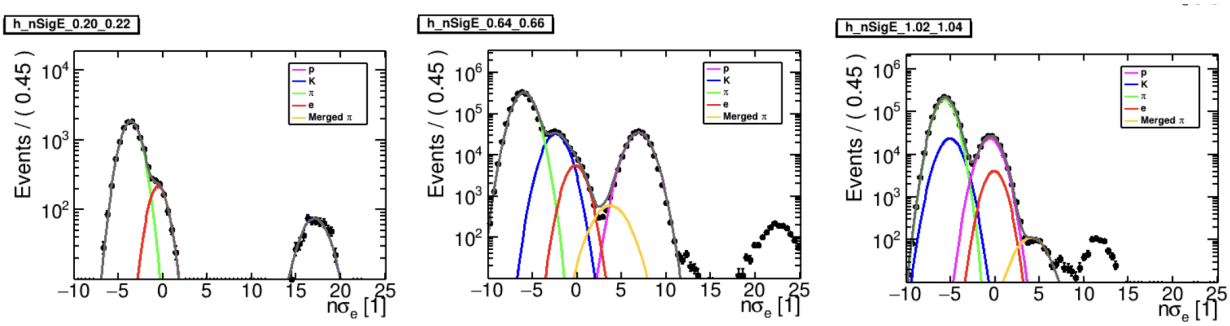

Figure 6: $n\sigma_e$ projection and Multi-Gaussian fittings at low, intermediate and high p.

Single particle distributions with the extracted parameters are displayed in Figures 2 - 5 for low, Intermediate and high p. With the exception of the obtained yield, which becomes different after electron identification cuts are applied, the other parameters restrict the intervals for the fitting of the sum. Figure 6 displays the Multi-Gaussian fitting of the total $n\sigma_e$ distribution at low, intermediate and high p. Also, from the figure 7, we can find the distribution of yield, mean and sigma for all particle species within the total the momentum range 0 - 4 GeV/c.

Finally, we have plotted the real purity distribution of inclusive electrons using the equation (5). The figure 8 describes the overall purity from the momentum range 0 - 4 GeV/c. Pions are the major contamination for inclusive electrons. Outside of the cross-over region around 0.48 and 0.97 GeV/c, we can observe that the estimated electron purity is almost within the limit of 0.95 - 1 at higher p range, which can be useful for further analysis.

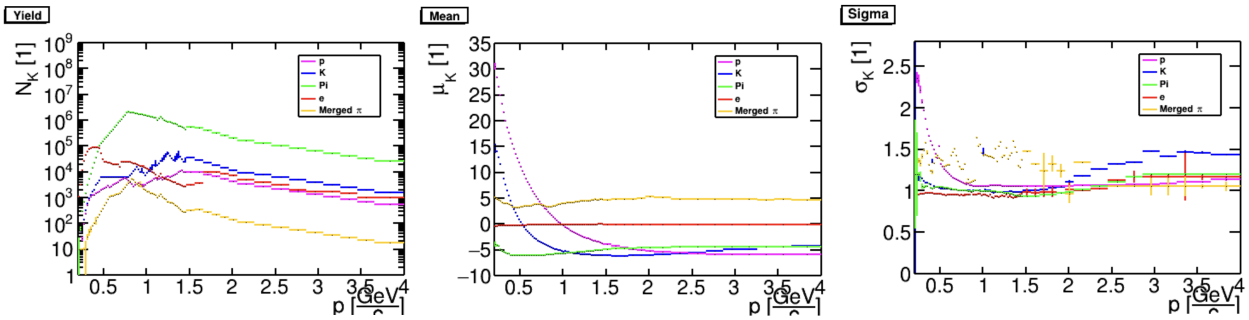

Figure 7: Yield, mean and sigma according to momentum obtained in the multi-gaussian fit, using the constraints provided by the single particle distributions.

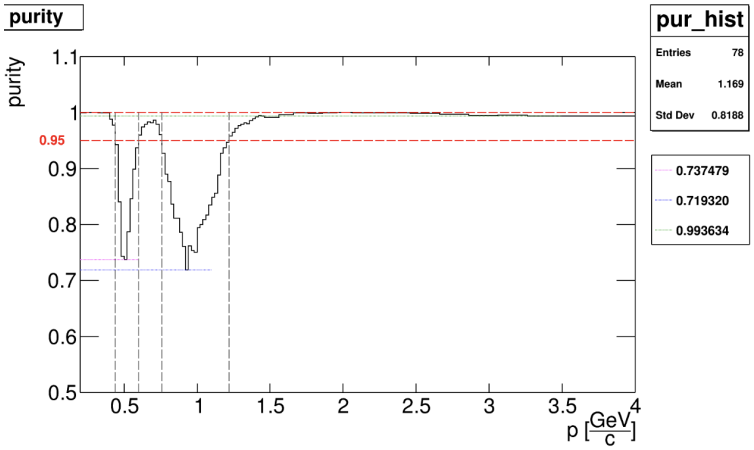

Figure 8: Inclusive electron purity as a function of momentum

5 Conclusions

In summary, we have successfully implemented the recently available BEMC information for this dataset to our analysis. Now we need to transform momentum to p_T. We fill 2D histogram of p vs p_T after electron PID cut and then profile mean. The final electron purity should be plotted with respect to transverse momentum. After finishing the purity studies, we will be able to correct the yield of inclusive electrons. The next step consists mostly in performing the simulations of the detectors to correct the yield of photonic and non-photonic electrons. After these steps are accomplished, the calculation of the NPE yield along with their modification factors R_{AA} and/or R_{CP} becomes straightforward.

References

[1] Francesco Prino and Ralf Rapp. Open heavy flavor in QCD matter and in nuclear collisions In: *Journal of Physics G: Nuclear and Particle Physics 43.9 (2016). issn: 13616471*, DOI: 10.1088/0954-3899/43/9/093002.

[2] Xin Dong, Yen-Jie Lee, and Ralf Rapp. Open Heavy-Flavor Production in Heavy-Ion Collisions In: *Annual Review of Nuclear and Particle Science 69 (Oct. 2019), pp. 417-445*, DOI: 10.1146/ANNUREV-NUCL-101918-023806

[3] A. Andronic et al. Heavy-flavour and quarkonium production in the LHC era: from proton-proton to heavy-ion collisions *European Physical Journal C 76.3 (2016). issn: 14346052*, DOI: 10.1140/epjc/s10052-015-3819-5

CHARM PRODUCTION

Kristýna Haismanová

1 Introduction

Theory called quantum chromodynamics is used to describe strong interaction but it is far from being complete. One of the major goals of particle physics is to put together a phase diagram of nuclear matter. Phase diagram is a graphical representation of behaviour of matter under different conditions. Many experiments all around the world such as SIS-100 or NICA, plan to examine regions near first order phase transition at lower temperatures and higher net baryon densities, while other such as BES or SPS are designed to operate at higher energies closer to critical point. After a collision in such experiments final products are captured and used to reconstruct what processes probably took place in earlier stages. Heavy quarks are some of those observables used as probes of previous events. Lightest of heavy flavour probes is charm quark which mass is around 1.3 GeV. Charm production is considered to be an important signal of the onset of the deconfinement of nuclear matter created in heavy-ion collisions.

2 Open charm as a probe to QGP

At high collisions energies heavy quarks are used to probe the properties of the hot deconfined phase and its interaction (energy loss mechanism) with the traversing partons.
In traditional scenario charm is only produced during the collision at hard processes, this initial state is well defined, and it is possible to apply QCD perturbative calculations. It carries the information about the very early stage of nuclear collision. In contrary to for example strange enhancement it does not come to existence later during expansion and it traverses the medium easier than lighter quarks as it is not affected that much. Modification factor R_{AA} tells us how powerful are the effects of the medium in comparison proton-proton collisions, where there are no medium effects present.

$$R_{AA} = \frac{1}{N_{coll}^{AA}} \frac{\frac{\mathrm{d}^2 N^{AA}}{\mathrm{d}p_T \mathrm{d}\eta}}{\frac{\mathrm{d}^2 N^{PP}}{\mathrm{d}p_T \mathrm{d}\eta}} \tag{1}$$

In reality, data from ALICE and STAR (1) show that charm R_{AA} suppression is very similar to that of light quarks. These results indicate that there is some interaction of charm quark with the hot deconfined matter that playes a nonnegligible role and charm energy loss mechanism is an interesting study point.

3 Charm production at lower energies

Heavy ion collisions at low collision energies are needed to explore other parts of the phase diagram. Charm quark can be used to study properties of the very high net baryon density matter close to the transition. In this regime important questions such as what is the microscopic mechanism of the charm production and how is it affected by the deconfinement could be answered. Several experiments aim to collect data about charm production close to the threshold energy, such as NA61/SHINE at SPS in CERN, J-PARC in Japan, or CBM at FAIR, which is being built in Darmstadt.

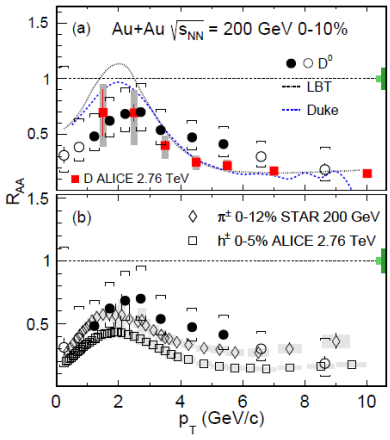

Figure 1: Strong suppression of D^0 a) in model calculations and b) in data from ALICE and STAR. [1]

3.1 Charm production at CBM

Collision energies and rate handling abilities are important properties of experiments. NA61/SHINE which does open charm measurement from lead-lead collisions, or Beam energy scanner II at STAR both reach higher energies than CBM is supposed to. BES also does not have any vertex detector close enough to collision. Older experimentally obtained data from STAR or HADES were measured at energies similar to that of CBM, but the statistics was several orders lower than is expected for CBM. This is the main advantage of CBM because it will allow scientists to study rare probes with higher precision than before. At FAIR collision energy for heavy ions is expected to be bellow 5 GeV therefore most of the charm production will be a subthreshold production.

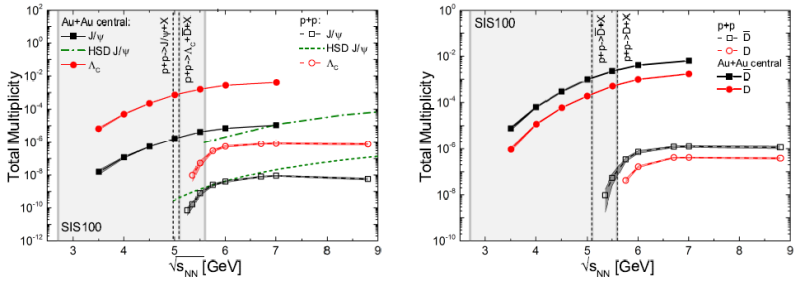

Figure 2: Production yields of J/Ψ, Λ_c, D and $\overline{\mathrm{D}}$ in p-p and central Au-Au as a function of collision energy. Vertical dashed lines indicate threshold center-of-mass energies and grey area is expected beam energy range at SIS100. [2]

3.1.1 MVD at CBM

The most important detector when speaking of charm production at CBM will be Micro Vertex detector which will be placed only centimetres from the target. Using 2 detection plates it will reconstruct trajectories and determine primary or secondary vertexes. Thanks to being so close to the event, it will be able to capture ever very shortly living particles such as D_0 mesons with very high precision.

References

[1] Zebo Tang, Wangmei Zha, Yifei Zhang. An experimental review of open heavy flavor and quarkonium production at RHIC, 2021.

[2] J. Steinheimer, A. Botvina, M. Bleicher. Sub-threshold charm production in nuclear collisions, 2017.

STUDIES OF STRANGENESS PRODUCTION VS. CHARGED PARTICLE MULTIPLICITY WITH PYTHIA8 AND PION INTERFEROMETRY WITH CORAL

Subhadip Pal

1 Introduction

The fundamental constituents of matter, Quarks and Gluons under normal conditions appear only to be confined to hadrons. Lattice QCD calculations have predicted that at temperatures above 160 MeV quarks and gluons would no longer be bound but instead form a phase of free quarks and gluons, the Quark-Gluon Plasma (QGP). The aim of relativistic heavy-ion collisions is to produce such a QGP in order to learn more about the strong nuclear force. In these proceedings, strangeness production which is a signature of the formation of QGP in relativistic heavy-ion collisions has been investigated with the PYTHIA8 monte carlo event generator. It also includes some aspects of two-particle femtoscopy, where the objective is to extract the space-time structure of a particle emitting source from the particle momentum spectra.

2 Strangeness Enhancement in p-p collisions

Having mass greater than that of the up and down quarks strange quarks are not present as valence quarks like the up and down in the initial state of p-p collisions. But they are sufficiently light to be produced during the course of a heavy-ion collision. In the early stages of high-energy collisions, strangeness is produced in hard(perturbative) $2 \longrightarrow 2$ partonic scattering processes by flavour creation ($gg \rightarrow s\overline{s}$, $q\overline{q} \rightarrow s\overline{s}$) and flavour excitation ($gs \rightarrow gs$, $qs \rightarrow qs$). Strangeness is also created during the subsequent partonic evolution via gluon splittings ($g \rightarrow s\overline{s}$). These processes tend to dominate the production of high transverse momentum (p_T) strange hadrons. At low p_T, nonperturbative processes dominate the production of strange hadrons [1].

In high energy p-p collisions, the particle production can be simplified into two broad steps namely initial hard scattering leading the production of partons and the subsequent hadronization of the initial parton configuration. The generation of partons and the partonic level activity involving multiple parton-parton interactions, the initial and final state radiations, and the activity of beam remnants can be approximately described by perturbative QCD while the fragmentation of the final parton configuration to observable hadrons is completely nonperturbative in nature. The understanding of the later part depends on statistical parametrization of experimental data, realistic modeling, parameter tuning etc [2].

3 Pion Interferometry

In HBT pion interferometry identical two-particle correlations are exploited to gain access to the space-time geometry and dynamics of the final freeze-out stage of heavy-ion collisions. Using identical two-pion correlation techniques at mid-rapidity the space-time structure of a collision fireball has been studied in this proceeding using a Core-Halo picture of pion emission. The source imaging technique incorporated in the CorAL (Correlation Algorithm Library) is implemented for analyzing the source functions from a given correlation data. CorAL is an in-progress code-base

to analyze two-particle correlations at small relative momentum. At small relative momentum, long-range Coulomb repulsion effects caused a suppression of the correlation function for $\pi^+\pi^+$ pair.

4 Results

Using the PYTHIA8 event generator, the enhanced production of strange hadrons in proton-proton collisions is investigated at 7 TeV center-of-mass energy as measured by the ALICE experiment at CERN. As shown in the left panel of Figure 1, the combined effect of color reconnection and the formation of ropes due to overlapping of QCD strings in a high multiplicity environment (Rope Hadronization) was able to describe the observed trend [2]. In the right panel, the PYTHIA8 estimates of the ratio for p-p collisions at $\sqrt{s} = 13$ TeV have been compared to 7 TeV.

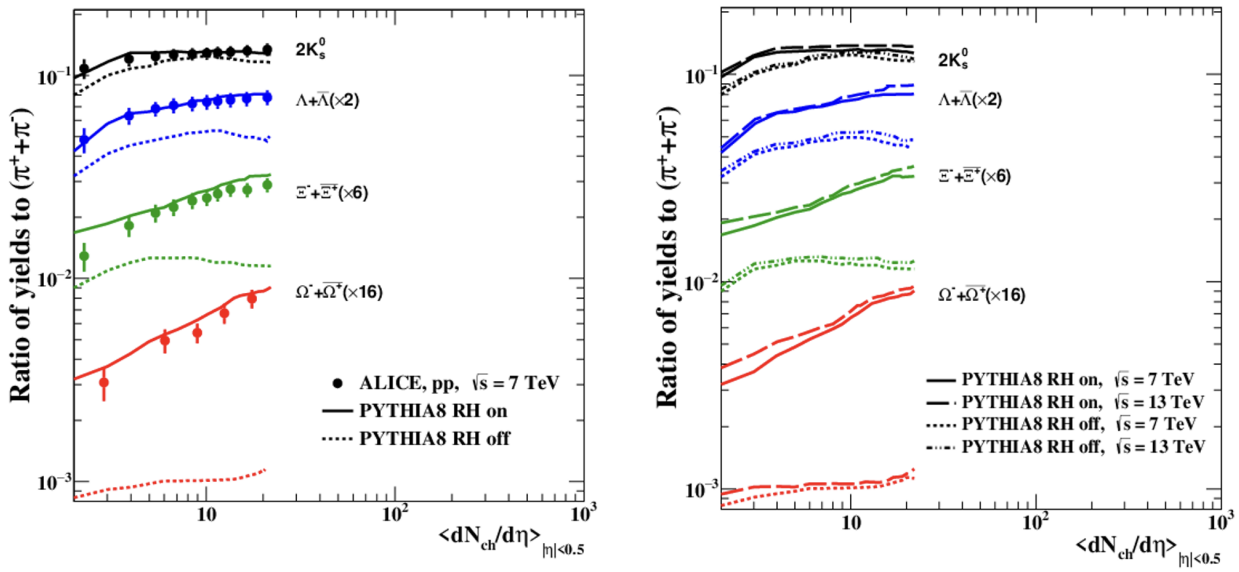

Figure 1: Ratio of yield of strange hadrons to pions as a function of multiplicity. The solid markers are data as measured by ALICE experiment. The solid and dotted lines are predictions of PYTHIA8 (with color reconnection) rope hadronization ON and OFF, respectively. The data points and the PYTHIA8 estimates are suitably scaled for visibility. Figure taken from [2]

.

Bulk properties of the system created in relativistic heavy-ion collisions can be studied via the transverse momentum (p_T) distribution through statistical approach. The transverse momentum distribution of those strange and multi-strange hadrons measured in the p-p collisions was analyzed using q-Weibull formalism for for a broad range of multiplicity classes. Mathematically, the q-Weibull distribution is obtained by replacing the exponential factor in Weibull distribution by its equivalent q-exponential [3].

$$P_q\left(x;q,\lambda,k\right) = \frac{k}{\lambda}\left(\frac{x}{\lambda}\right)^{k-1} e_q^{-\left(\frac{x}{\lambda}\right)^k} \tag{1}$$

where,

$$e_q^{-\left(\frac{x}{\lambda}\right)^k} = \left(1-(1-q)\left(\frac{x}{\lambda}\right)^k\right)^{\left(\frac{1}{1-q}\right)} \tag{2}$$

Figure 2 shows the invariant yield of K^0_S, Λ^0, Ξ and Ω as a function of p_T for p–p collisions at $\sqrt{7}$ TeV for ten different multiplicity classes and the evolution of values of the extracted fit parameters with respect to the mean charged

particle density $\langle dN_{ch}/d\eta \rangle$ corresponding to the multiplicity classes. The q parameter is observed to be greater than one for the measured strange and multi-strange hadrons for all multiplicity classes. These values are consistent with the non-equilibrium scenario present in p–p collisions [3]. An increase in collective radial flow implies an increase in mean p_T and the presence of collective radial flow creates a mass ordering of mean p_T. The λ parameter exhibits both behaviors and thus λ can be related to collective velocity of particles and therefore to mean p_T.

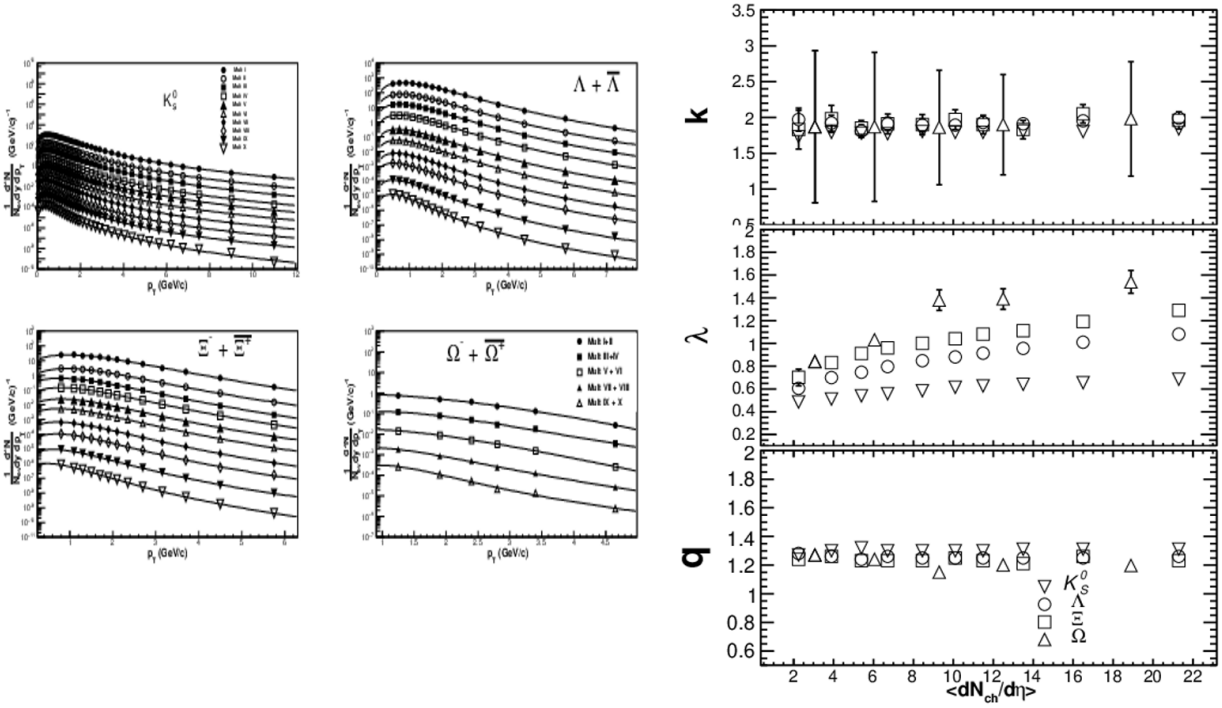

Figure 2: Left panel: p_T distribution of strange and multi-strange hadrons in p–p collisions at $\sqrt{7}$ TeV for $|\eta| < 0.8$ as measured by ALICE experiment at LHC. Right panel: Variation of k, λ and q as a function of $\langle dN_{ch}/d\eta \rangle$. Figure taken from [3]

5 Summary

The combined effect of color reconnection and the rope hadronization was able to describe the enhanced production of strange hadrons in proton-proton collisions at ALICE. The q-Weibull function successfully describes the transverse momentum distribution of the strange particles and the strange particles were emitted from a source which is not fully equilibrated. A mass hierarchy was also observed in the values of λ. These features are consistent with the presence of collectivity in the medium formed.

References

[1] Jaroslav Adam et al. Enhanced production of multi-strange hadrons in high-multiplicity proton-proton collisions. in *Nature Phys.*, pages 535–539, 2017.

[2] Ranjit Nayak and Subhadip Pal and Sadhana Dash Effect of rope hadronization on strangeness enhancement in $p-p$ collisions at LHC energies. in *Phys. Rev. D*, volume 100, issue 7, 2019.

[3] Pritam Chakraborty, Tulika Tripathy, Subhadip Pal and Sadhana Dash Multiplicity dependence of strange and multi-strange hadrons in p–p, p–Pb and Pb–Pb collisions at LHC energies using Tsallis–Weibull formalism. in *The European Physical Journal A*, volume 56, 2020.

IMAGINARY MAGNETIC FIELD IN RELATIVISTIC QUANTUM MECHANICS

Alexandra Ridziková

1 Introduction

The magnetic field is an interesting concept in quantum mechanics and leads to physical effects that have no classical analogy. In recent years relevance of magnetic fields with a non-zero imaginary component in description of quantum mechanics was shown. The magnetic field occurs also in the description of the stability of rotating black holes.

An important equation in relativistic quantum mechanics is Dirac's equation, which replaces the Schrödinger equation which is not Lorentz invariant. The non-selfadjoint Dirac operator D_a on circle with a complex magnetic field is investigated.

2 Magnetic field in quantum mechanics

Physical systems can be described by partial differential equations. A typical example is quantum mechanics, where observables manifest as linear operators on a Hilbert space representing the state space of quantum states. The solution of the Schrödinger equation gives the time evolution of the system:

$$i\hbar\frac{\partial\psi}{\partial t} = H\psi \tag{1}$$

with H being a linear self-adjoint operator representing the total energy of the system.

Magnetic field in quantum mechanics enters the theory indirectly, through its vector potential in the Schrödinger equation. Hamiltonian of charged particle in electromagnetic field has form

$$H = \frac{1}{2m}(\vec{P} - q\vec{A})^2 + q\varphi, \tag{2}$$

where $\vec{A}$ and φ are potentials for which it applies:

$$\vec{B} = \text{rot}\vec{A}, \qquad \vec{E} = -\text{grad}\varphi - \frac{\partial\vec{A}}{\partial t}. \tag{3}$$

3 Imaginary magnetic field

3.1 Quasi-hermitian quantum mechanics

The Spectrum of the linear operator assigned to observable must be identical to the set of values that can be measured for that quantity, which is reason why self adjointness of operators in quantum mechanics is required. In recent years many attempts have been made by physicists to represent observables in quantum mechanics by operators which satisfy

certain physical-like symmetries instead of the self-adjointness. This unconventional representation of observables is consistent with axioms of quantum mechanics if, and only if, the non-self-adjoint observable is quasi-self-adjoint, i.e

$$H^* = \Theta H \Theta^{-1}, \tag{4}$$

where Θ is positive, bounded and boundedly invertible operator called metric.

By modifying the inner product $\langle\cdot|\cdot\rangle$ in the underlying Hilbert space to $\langle\cdot|\cdot\rangle_\Theta := \langle\cdot|\Theta\ \cdot\rangle$, H is self-adjoint again:

$$\langle\phi|H\psi\rangle_\Theta = \langle\phi|\Theta\ \Theta^{-1}H^*\Theta\ \psi\rangle = \langle H\phi|\Theta\ \psi\rangle = \langle H\phi|\psi\rangle_\Theta.$$

3.2 Stability of black hole

Analogies between physical systems, often play a important role in developments of theories. We discuss mathematical analogy between the descriptions of black hole horizons and quantum charged particles. Apparent horizons –namely marginally outer trapped surfaces (MOTS)– has a stability notion which admits a spectral characterization in terms of the eigenvalue of the operator

$$L_{\mathcal{S}}\psi = \Big[-\Delta + 2\Omega^a D_a - (|\Omega|^2 - D_a\Omega^a - \frac{1}{2}R_{\mathcal{S}} + G_{ab}k^a l^b)\Big]\psi$$

defined on the apparent horizon $\mathcal{S}$.

By substitution:

$$\Omega_a = \frac{ie}{\hbar c}A_a \qquad R_{\mathcal{S}} = \frac{4me}{\hbar^2}\varphi, \qquad G_{ab}k^a l^b = -\frac{2m}{\hbar^2}V$$

passes the stability operator $L_{\mathcal{S}}$ to Hamiltonian of non-relativistic charged particle. Applies $\frac{\hbar^2}{2m}L_{\mathcal{S}} = H$, where

$$H = \frac{1}{2m}\Big(-i\hbar D - \frac{e}{c}A\Big)^2 + e\varphi + V.$$

Because of the operator Ω_a being real, the potential A must be purely imaginary. Magnetic Hamiltonian with imaginary vector potential on a closed Riemannian manifold controls the stability of apparent horizons in black hole spacetimes.

This analogy has the potential to link the well-studied quantum particle problem and the rich but largely unaproached MOTS subject.

4 Magnetic Dirac operator on circle

We introduce relativistic Dirac operator D_a on circle with complex-valued magnetic potential $a : (-\pi, \pi) \to \mathbb{C}$ and mass m:

$$(D_a\psi)(x) := \begin{pmatrix} m & -i\partial_x - a \\ -i\partial_x - a & -m \end{pmatrix}\begin{pmatrix}\psi_1 \\ \psi_2\end{pmatrix}, \tag{5}$$

with domain

$$\text{Dom } D_a := \left\{\psi = \begin{pmatrix}\psi_1 \\ \psi_2\end{pmatrix} \in W^{1,2}((-\pi,\pi);\mathbb{C}^2) : \psi(-\pi) = \psi(\pi)\right\}. \tag{6}$$

Operator D_a is self-adjoint, if and only if, Im $a = 0$.

By solving characteristic equation $D_a\psi = \lambda\psi$ we obtain the spectrum: $\sigma(D_a) = \left\{ \pm\sqrt{m^2 + (n - \langle a\rangle)^2}\right\}_{n\in\mathbb{Z}}$ of Dirac operator. The following statement holds

Theorem 4.1

- *Operator D_a is quasi-self-adjoint if, and only if*

$$\mathrm{Im\,a} = 0,$$

with metric operator

$$(\Theta\psi)(x) := \begin{pmatrix} \exp\left(2\mathrm{Im\,A(x)}\right) & 0 \\ 0 & \exp\left(2\mathrm{Im\,A(x)}\right) \end{pmatrix} \begin{pmatrix} \psi_1 \\ \psi_2 \end{pmatrix}.$$

- *The eigenfunctions of D_a form a Riesz basis.*

It follows that spectrum of D_a is purely real under condition Im $\langle a \rangle = 0$, which represents more general condition than self-adjointness (ie. Im $a = 0$). However drastic change in basis properties occurs.

References

[1] J. L. Jaramillo, *Black Hole Horizons and Quantum Charged Particles.* Classical and Quantum Gravity, Vol. 32, No. 13 (2015).

[2] L. Andersson, M. Mars, W.Simon, *Local existence of dynamical and trapping horizons*, Phys. Rev. Lett. 95 (2005).

[3] D. Krejčiřík, *Complex magnetic fields: An improved Hardy-Laptev-Weidl inequality and quasi-self-adjointness*, SIAM J. Math. Anal. 51, 790-807 (2019).

[4] D. Krejčiřík, P. Siegl, M. Tater, J. Viola, *Pseudospectra in non-Hermitian quantum mechanics*, Journal of Mathematical Physics 56, 103513 (2015).

TRANSVERSE EXPANSION IN NUCLEAR COLLISIONS AT RHIC BES

Jakub Štěrba

1 Introduction

The quark-gluon plasma can be created in heavy ion collision, if sufficient energy density is reached. It is created in a form of a so called fireball, which shows collective behaviour. One of the signs of such collectivity is the anisotropic flow, the experimental sign of which is the anisotropic particle production in azimuthal angle. Therefore, the particle spectrum can be expanded into the Fourier series

$$\frac{\mathrm{d}N}{\mathrm{d}\phi} \sim 1 + 2\sum_n v_n \cos[n(\phi - \psi_{RP})], \tag{1}$$

where the v_n are Fourier coefficients, called flow coefficients. For the particular case of $n = 2$, it is the case of elliptic flow. This anisotropic flow is caused by the initial shape of the fireball and the pressures present. Also fluctuations of the nucleons inside of the nuclei play an important role in anisotropic flow formation.

For modelling of the evolution of the fireball a hydrodynamic approach turned out to be useful. It treats the QGP as a viscous fluid which is evolved by the hydrodynamic equation until the point of freeze-out. Of course, the hydrodynamic code is not able to simulate the whole collision process, therefore, it needs some initial conditions, such as Glauber model, and final state simulations, such as transport code. In our case using the vHLLE hydrodynamic code (see [3]), for initial state the Glissando Glauber model (see [1], [2]) is used and SMASH transport code (see [4]) is used as final state.

In the Fig.1 the results for simulations of Au+Au at 27 GeV and centralities 10-20%, 20-30% and 30-40% are shown. It can be seen that the results for the centrality 20-30% quite match the experimental data obtained by STAR collaboration (see [5], [6]), however, for other centralities the results match the experimental data rather poorly. That is why we have decided to create new initial state generator, which would have a new feature, which would allow initial transverse momentum deposition.

2 IMAGO: A new Glauber model

The new initial state generator is based on the principle of standard Glauber Monte Carlo model. It works in a few simple steps, which shall be shortly described.

The first step is generating of the nuclei. The nucleons are generated accordingly to thy Woods-Saxon distribution

$$\rho = \frac{\rho_0}{1 + \exp\frac{r-R}{a}}, \tag{2}$$

where a certain spacing between the centers of the nucleons are maintained, in order for them not to overlap.

Now, the nuclei are generated, however, they need to be collided. The nucleons collide in they are close enough and the close-enough distance is given by

$$d = \sqrt{\frac{\sigma_{NN}}{\pi}}, \tag{3}$$

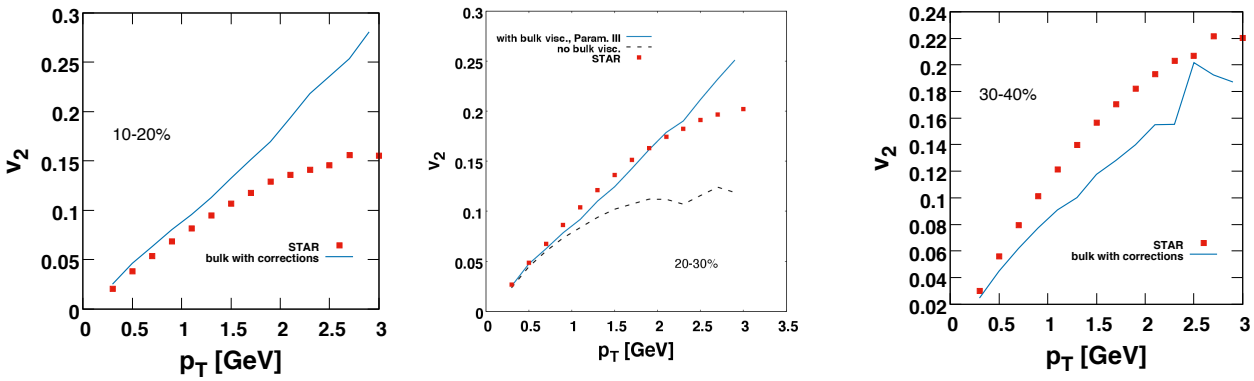

Figure 1: Sample figure caption.

where σ_{NN} is the energy-dependent nucleon-nucleon inelastic cross section.

The third step is to define centrality of the collision. The centrality in our case is given according to the cumulative distribution of the *Relative deposited strength* or *RDS*. It is given as a combination of the number of participants N_{part} and number of binary collisions N_{coll} of given collision and is determined by the parameter α as

$$RDS = \frac{1}{2}(1-\alpha)N_{part} + \alpha N_{coll}. \tag{4}$$

Now, once the centrality of the collision can be determined, the last step can be implemented - the initial transverse momentum deposition. Let us explain the procedure of the deposition. As two nucleons collide, each of them gains an initial p_T-kick in the direction opposite to their relative distance. Each nucleons gain such p_T-kick at each collision, of course in different directions, however, the magnitude of each p_T-kick is the same and is given as a parameter of the model. All contributions for each nucleon is the summed into the final one. This initial transverse momentum is then smeared in the transverse and longitudinal profile together with the energy density and baryon number. Such smeared profile can then be filled into the hydrodynamic code and the whole simulation can be run.

3 IMAGO+vHLLE+SMASH

The whole vHLLE package was run with the new initial state generator for Au+Au collisions at 27 GeV and for centralities 10-20%, 20-30% and 30-40%.

In Fig.2 an elliptic flow transverse momentum dependence is shown for different values of initial p_T-kicks together with STAR data and original simulations using Glissando as initial conditions. Overall, the simulations using the new model describe the experimental data better than those using Glissando, however, the effect of the initial transverse momentum deposition is more pronounced for less central collisions because of the profiles of the initial conditions. For more central collisions, the initial transverse momentum acts as an additional shear viscosity in the hydrodynamic modelling and thus reduces the elliptic flow values.

In Fig.3, a transverse momentum positive pion spectra are shown. These are also important, sinco it can be seen that changing the value of the p_T-kick does not change the shape of the spectrum. This means, that the momentum is only redistributed in the initial conditions and one does not add any radial flow.

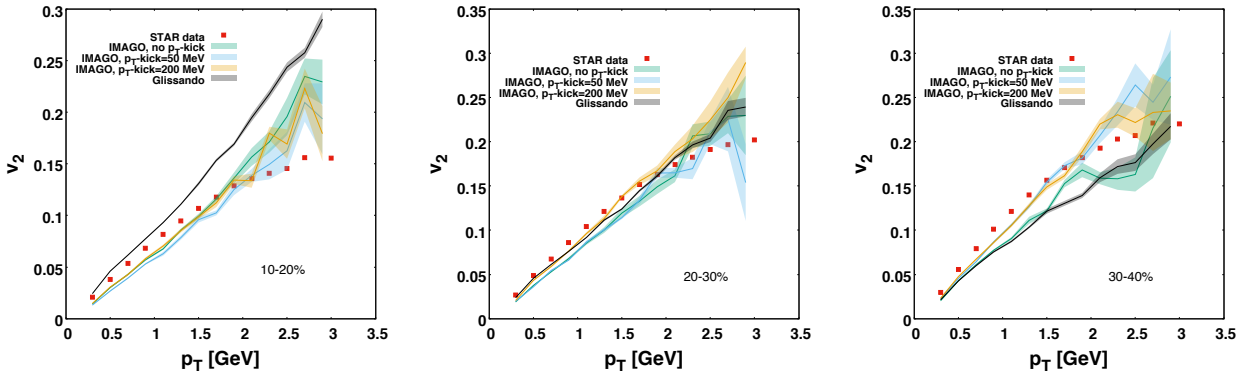

Figure 2: Sample figure caption.

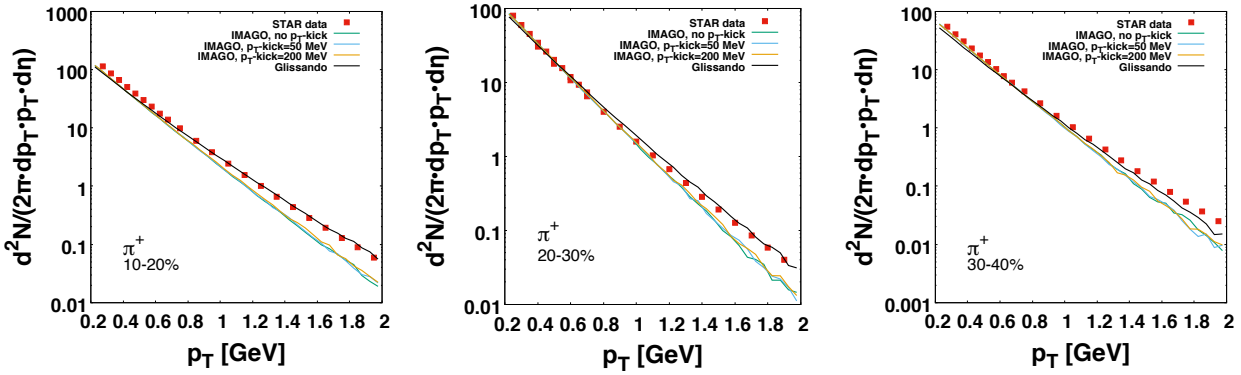

Figure 3: Sample figure caption.

References

[1] W. Broniowski, M. Rybczynski and P. Bozek, GLISSANDO: Glauber initial-state simulation and more.., Comput. Phys. Commun. **180** (2009), 69-83.

[2] M. Rybczynski, G. Stefanek, W. Broniowski and P. Bozek, GLISSANDO 2 : GLauber Initial-State Simulation AND mOre. . . , ver. 2, Comput. Phys. Commun. **185** (2014), 1759-1772.

[3] I. Karpenko, P. Huovinen and M. Bleicher, A 3+1 dimensional viscous hydrodynamic code for relativistic heavy ion collisions, Comput. Phys. Commun. **185** (2014), 3016-3027.

[4] J. Weil, V. Steinberg, J. Staudenmaier, L. G. Pang, D. Oliinychenko, J. Mohs, M. Kretz, T. Kehrenberg, A. Goldschmidt and B. Bäuchle, *et al.* Particle production and equilibrium properties within a new hadron transport approach for heavy-ion collisions, Phys. Rev. C **94** (2016) no.5, 054905.

[5] L. Adamczyk *et al.* [STAR], Bulk Properties of the Medium Produced in Relativistic Heavy-Ion Collisions from the Beam Energy Scan Program, Phys. Rev. C **96** (2017) no.4, 044904.

[6] L. Adamczyk *et al.* [STAR], Inclusive charged hadron elliptic flow in Au + Au collisions at $\sqrt{s_{NN}}$ = 7.7 - 39 GeV, Phys. Rev. C **86** (2012), 054908.

EVOLUTION OF GALAXIES IN CLUSTERS

Anežka Kabátová

1 Introduction

The hot and dense environment of galaxy clusters represents a site of dramatic changes in member galaxies' morphology as they shift from blue gas-rich to red gas-poor objects due to multiple processes.

One of the essential external processes is the ram pressure stripping that galaxies experience while moving with high velocities through the hot intra-cluster medium (ICM), whose temperatures reach 10^7 K. During this process, the gas reservoir of galaxies is gradually depleted from outside in as suggested by multiple observations of partially or fully gas-stripped galaxies. Without any gas in the disk left, the star formation of the galaxy is quenched. However, a very different story evolves in the tail behind the parent galaxy. After leaving the disk, the displaced gas presumably mixes with the ICM forming a multi-phase environment whose temperature and density depends locally on domination of heating and cooling processes respectively. Yet, details of the evolution of the tail gas remain unknown and are subject of the intense research.

We present molecular gas observations of five ram-pressure stripping Coma cluster galaxies that were previously studied in Hα and are at different stages of their evolution within the cluster. Using these observations, we would like to come one step closer to answering following questions, among others: What drives the presence of molecular gas in tails of cluster galaxies? Is the molecular gas (if present) formed in-situ or is it directly stripped from the parent galaxy? What is the star formation efficiency in the tails?

2 Observation

Observation was carried out with the IRAM 30m antenna operated by Institute de Radio Astronomie Millimétriqie located at Pico Velenta, Spain, between December 2014 and December 2016. Two prominent CO lines: ^{12}CO(1-0) (ν_{rest} = 115.271 GHz) and ^{12}CO(2-1) (ν_{rest} = 230.538 GHz) were observed simultaneously. The main beam projected area corresponds to $\Omega_B \approx 120$ kpc^2 and 31 kpc^2, respectively. Data were reduced engaging CLASS tool of GILDAS software package developed for primary use in IRAM data reduction. Detected CO lines were fitted by Gaussian to measure the antenna temperature, width and position.

The list of observed galaxies and their properties can be found in Table 1. The example of observed object (GMP 4471) can be found in Figure 1.

3 Results

In three out of five galaxies in the sample, molecular gas was detected clearly outside the galaxy in their ram pressure-stripped tails. In one galaxy, the molecular gas was detected in the region partially covering the outer part of the disk and innermost part of the tail; however, none was detected in the tail itself. In the last galaxy, the tail observation was not conducted due to limited time.

Here I state some of observational highlights of the sample. In the galaxy GMP 4471, the molecular gas was detected alongside the whole tail in three different regions. It is clear that the extension of the large molecular tail is $\approx$ 50 kpc, with the last observed region located 43 kpc from the galaxy center. The structure of the tail of GMP 2559

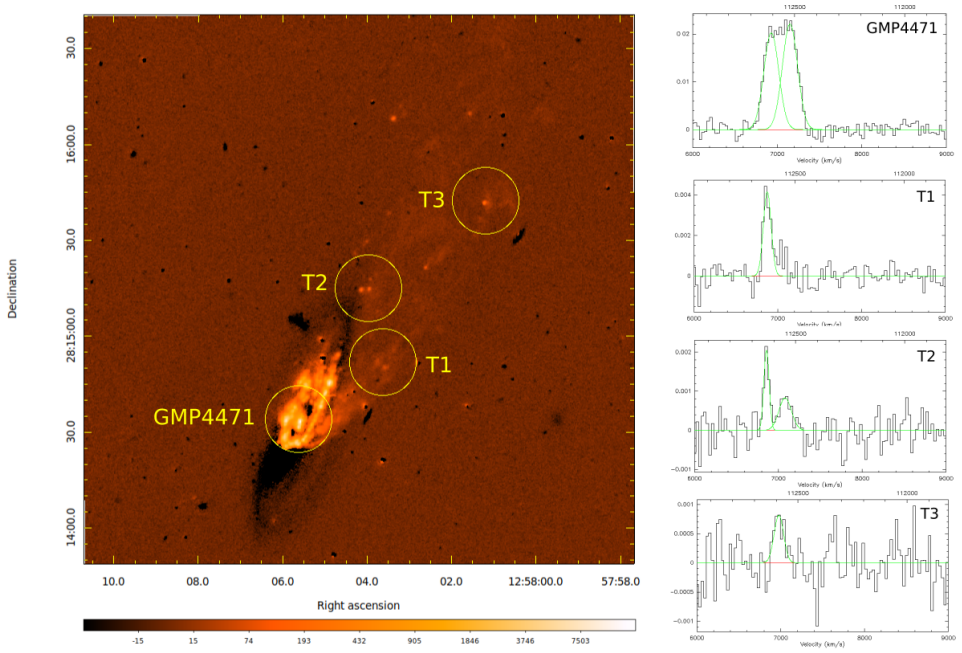

Figure 1: Left: Optical Hα image of the galaxy GMP 4471 (Subaru telescope) overlaid with ^{12}CO(1-0) beams (HPBW $\approx$ 10.32 kpc) of the IRAM 30m antenna located at the observed pointings at the main body of the galaxy and the tail. Right: The ^{12}CO(1-0) spectra smoothed to 30.48 km s^{-1} channels.

is much more complicated. The south-eastern region shows a multi-peak detection with a low-velocity component ($\approx$ 1000 km s^{-1} w. r. t. the galaxy) already known from previous observations, as well as three different peaks much closer to the parent galaxy velocity. In the tail of the galaxy GMP 3779, a clear detection at almost exactly same velocity as the parent galaxy can be seen in both CO(1-0) and CO(2-1). This is rather surprising, considering the high velocity of the parent galaxy w.r.t. to the Coma cluster. As mentioned before, for the galaxy GMP 3896, CO was only detected in a boundary region between the disk and the tail. The multi-peak structure of the detection in the parent galaxy suggests its rotation, which is supported also by the detection in the boundary region that coincides with one side of the wide peak of the parent. For the last galaxy of the sample, GMP 3071, only the detection of the parent galaxy is available, so no conclusions about its tail structure can be made. However, even the detection in the galaxy disk is considerably weak, implying probably a strong stripping that this galaxy has been exposed to.

The interpretation of these observations is still in progress. What I know for sure at this moment is that for most of the galaxies, the amount of molecular gas extrapolated from the amount of CO gas is higher than expected from the stellar mass of these objects. That could suggest that, besides stripping, the ram pressure temporarily enhances the conversion of the atomic gas into the molecular gas. That could also lead to episodes of increased star formation. Comparing these results to previous works, it is striking that this property does not hold universally. Therefore, a natural next step is to investigate whether it reflects some underling properties of individual clusters.

Besides that, a possible link was found between the strength of the ram pressure imposed on the given object and the amount of molecular gas in its tail. The method has some obvious limitations - single-dish observation does not provide enough coverage to make strong conclusions about the extend of molecular gas, however, the correlation is very strong and definitely worth further investigation.

4 Conclusion

As the presented work is still in progress, it is obvious that it will bring new exciting results to the community. The ram-pressure stripping as a driver of galaxy evolution is a hot topic ignited by the upswing of modern radioastronomy.

Table 1: Properties of observed Coma cluster galaxies. Coordinates, type, redshift, velocity w.r.t. Coma cluster, stellar mass.

Name	RA, Dec [Deg]	Type	z	V_{Coma} [km s^{-1}]	$M_\star$ [$10^8 M_\odot$]
GMP 4471	194.523520, 28.242740	Scd	0.02351	124	209
GMP 2559	195.158042, 28.057361	Scd	0.02615	720	46
GMP 3896	194.733375, 27.833361	S	0.02525	629	178
GMP 3779	194.772000, 27.644583	Sb	0.01853	-1499	15
GMP 3071	194.983804, 27.746328	S0/a	0.02963	2066	8

I hope that my work will at very least contribute to the brief list of observed molecular tails of stripped galaxies. Moreover, the revealed unexpected properties of these objects will hopefully contribute to the puzzle of galaxy evolution in cluster environment.

ELECTRON PRODUCTION FROM THE OPEN-HEAVY FLAVOR DECAY IN RELATIVISTIC HEAVY-ION COLLISION AT STAR

Ayanabha Da